Model Independent Search for Neutrinos from Gamma Ray Bursts with the IceCube Detector

by

Dennis Diederix

Submitted in Partial Fulfillment of the Requirements for the Degree

of Master of Science in Physics

Under the supervision of

Prof. dr. N. van Eijndhoven at the Vrije Universiteit Brussel,

Prof. dr. A. Achterberg at the University of Utrecht

Brussels, December 2010

Preface

The most violent and energetic phenomena in the Universe known to date since the Big Bang, are Gamma-Ray Bursts (GRBs). In the short lifetime of a GRB (from tenths of a second up to several minutes) it emits photons with an amount of energy that is comparable to the energy that is produced in a year by all the stars in our Milky-Way. These sources of gamma-ray photons are detected all over the sky at a rate of a few hundred per year.

The production of photons by GRBs can be described relatively well by electromagnetic models, which describe the acceleration of electrons in a fireball model (exploding star model). A relativistic outburst of bulk matter accelerates electrons to high energies, which emit synchrotron radiation because of the strong magnetic fields that are present in the fireball explosion. Other mechanisms could also produce photons, like Bremsstrahlung, describing electrons that emit photons due to mutual interactions with other electrons, or inverse Compton scattering, where already existing photons gain energy upon interaction with the energetic electrons. Moreover, hadrons (like protons and nuclei) could also be accelerated along with the electrons in the fireball model of a GRB. These hadrons could explain the existence of the highest energetic ($\sim$EeV) charged particles detected at the Earth (so-called cosmic rays). However, these models still need to be verified experimentally. The detection of high-energy neutrinos coming from GRBs will verify the hadronic acceleration model of GRBs and will be decisive if GRBs can be the sources of very high-energy cosmic rays, which would account for a break through in the Astro-Particle Physics field.

The IceCube neutrino detector is built at the South-Pole with the purpose to detect high-energy neutrinos in a range of about TeV-PeV. A search for neutrinos from 102 northern sky GRBs with the IC40 detector configuration is described in this report. Signals in the detector that occur during a period of two hours around the detection time of each GRB are stacked so that a possible neutrino signal will add up constructively in our time-profile. We assume that a possible difference in production time between the photons and neutrinos is uniform for all the GRBs in our sample due to a generic production mechanism. Thus the analysis is sensitive for precursor, prompt and afterglow neutrino signals as we use a large time-window.

A full description is provided on how neutrinos are detected, describing how the electronic read-out of the detector (so-called waveform) is analyzed and how this could be optimized. Methods on how a track is reconstructed for particles

in the detector is given, as well as a discussion on the method used to reduce background events. A Bayesian statistical method is described to determine the significance of an observation and an investigation on an improvement method (combining the angular and timing information of the reconstructed track) is provided. Furthermore, the experimental data of the IC40 detector is investigated. The stability and specific features of the data are investigated, before several filtering procedures are performed to result with our final data-sample. The so-called "un-blinding" procedure that needs to be followed before one is allowed to look at the final data-set lay beyond the scope of this research, which prevented a disclosure of a possible discovery or calculation of an upper-limit on the flux. Nevertheless, the analysis presented here shows that the sensitivity needed to claim a detection can be reached.

First, I am very grateful to my supervisor Nick van Eijndhoven , who gave me the opportunity to do my masters research in a new and very exiting environment, without getting a feeling of being 'an alien' in Brussels. Although we enjoyed the warmth of our southern friends, it felt like we started a new adventure together as the new Dutch in Brussels. You gave me the opportunity and guidance to enjoy the many facets of research, providing me with thorough knowledge on all aspects of my research project and introduced me, via memorable activities, to the most exiting international research collaboration.

I owe my thanks to Bram Achterberg, who helped improve my report enormously with his thorough view and comments.

It has been a great pleasure to work with the IceCube collaboration, especially the people from the IIHE in Brussels, who were always kind enough to help a student with a number, who made me feel at home, who helped me with all my bugs and other research issues and tried to keep me in physical shape (both at lunch and in the sports center). So I thank my room mate Robbe and Erik, Mathieu, Mark, Alberto, Alfio, Sabrina, Kael, Debanjan, Kalpana, Jan, Michael and Abdel, Catherine, Daniel and of course Marleen for a great time and for all your help.

Ik heb hele mooie herinneringen aan mijn gezellige en prachtige huis in Brussel, waar altijd een bordje klaar stond en af en toe een super mooie film werd gedraaid. Lies en Tom dank voor jullie enorme gastvrijheid.

Net over de grens wil ik al mijn vrienden en familie bedanken. Mijn ouders voor hun steun tijdens al die jaren studeren, Jurjen voor zijn goede raad en natuurlijk Heleen.

Contents

Chapter 1

Neutrino Physics

1.1 Introduction

The Universe with all its mysteries is the most observed object known to mankind. In every ancient culture, from the ancient Middle-East, Chinese, Arabic to Indian societies, studies of our Universe can be found.

Potential insight in the mechanisms of the Universe is mainly obtained by detection and observation of messenger particles, originating from astrophysical sources. Originally, only the visible light could be used to perform astrophysical studies. But even with the naked eye and use of some basic telescopes a broad understanding of our place in the Universe was developed. Only since one century ago, the sensitivity of the detectors improved dramatically, making it possible for astronomers to use infrared, ultra-violet, radio wavelength and even X-Ray and gamma-ray light as cosmic messengers. With the development of satellites, astronomical research really developed rapidly.

New messengers from our cosmos were discovered when Victor F. Hess tried to understand the radiative ionization at the Earth. He discovered a remarkable phenomena on the radiation as it increased while his experimental balloon rose in the atmosphere.

> *The result of the existing observations seem to be explainable assuming that a radiation of high penetrating power enters our atmosphere from above and causes even in its lowest layers a fraction of ionization in closed vessels.* **V.F.Hess (1912)** [1]

The radiation increase which Victor Hess discovered, arises from charged particles hitting the Earths atmosphere, and ionizing particles along their path through the atmosphere. The ionized particles form a so-called air-shower which results in an increase in radiation in the higher regions of the atmosphere, see Figure 1.1. The original particles that hit the atmosphere are named *cosmic rays*, and consist mainly of protons (80%) and helium nuclei (14%) [2]. With the discovery of cosmic rays, a new research field, Particle Physics, was

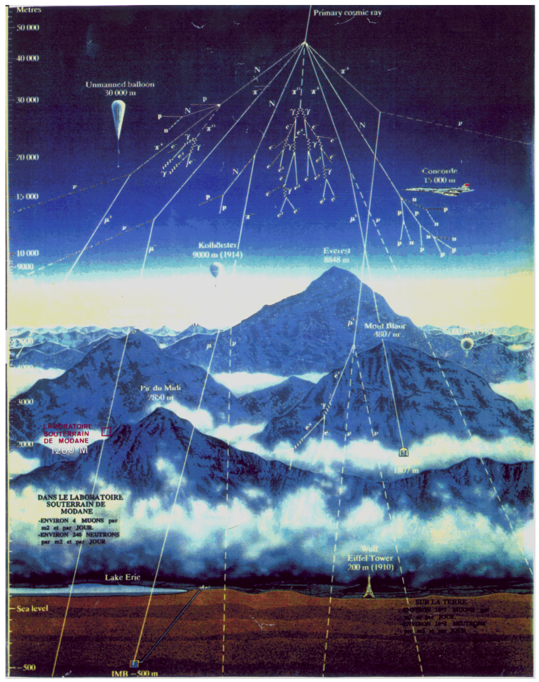

Figure 1.1: Schematic view of (high-energy) charged particles originated in our cosmos, and hitting the atmosphere, so-called Cosmic Rays. The particles produce an air-shower of ionized particles, which result in an increase of radiation in the higher region of the atmosphere.

born. Furthermore, after the existence of the *neutrino* was proven by Fred Reines and Clyde Cowan in the nineteen-fifties, yet another very promising cosmic messenger was found.

1.2 Cosmic Rays

Over the last decades, intensive studies have been made of cosmic rays at ever increasing energies. Cosmic rays can have very high energy, up to ten thousand times more than the particles that will be produced by the largest accelerator built by mankind: the Large Hadron Collider. The energy of cosmic rays ranges from 10^3 up to 10^{20} eV, whereas the number of particles per square meter per second arriving at Earth (the flux) spans over approximately 31 orders in magnitude.

Above the GeV region the spectrum of the cosmic rays is characterized by a power law

$$\frac{dN}{dE} \propto E^{-s} \tag{1.1}$$

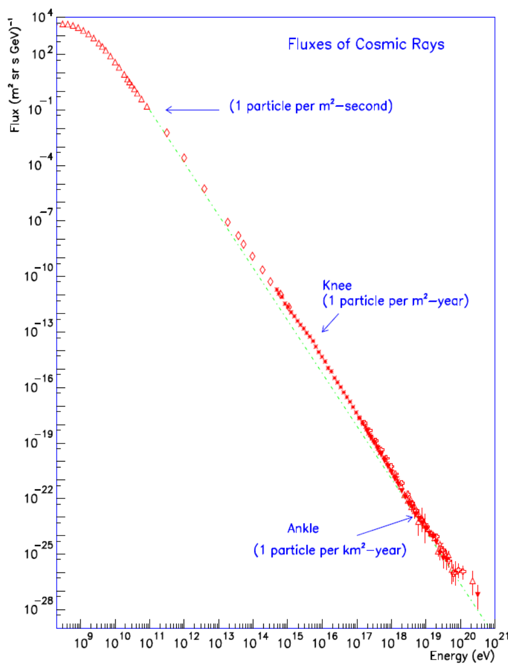

Figure 1.2: Compilation of measurements of the differential energy spectrum of Cosmic Rays. The energy is drawn on the x-axis, and the flux of particles is given on the y-axis. The dotted line shows an E^{-3} power-law spectrum line for comparison [3].

with spectral index $s \approx 2.7$. Apart from the so-called "knee" (at 10^{15} eV) where the flux steepens to $s \approx 3$ and the "ankle" (at 10^{19} eV) where the spectral index becomes $s \approx 2.7$ again, the spectral index is remarkably constant for a large range in energy. This is illustrated in Figure 1.2 and in Figure 1.3 the flux is multiplied with $E^{2.7}$ to emphasize the shifts of the spectral index.

Due to the low flux above 10^{14} eV, only ground-based detectors with large apertures and long exposure times are able to detect a significant amount of events. These experiments exploit the atmosphere as a giant calorimeter, the most famous one being the Auger experiment [4], named after the famous physicist Pierre Auger (1899-1993). Already in 1938 he concluded from the size of the extensive air-showers (EASs) that the spectrum should extend up to or even beyond 10^{15} eV [4]. Subsequent experiments have proven this, by observing primary particles which have energies higher than 10^{20} eV [5] [6].

Particles with an energy smaller than $\sim$GeV are understood to be produced by Solar activity (Solar flares and shock waves in the Solar corona) [7], whereas higher energy particles originate from other sources in our Galaxy.

The lowering in flux at the "knee" (around 10^{15} eV) can be explained by the maximum acceleration power of Supernova's (SN; exploding stars) in our

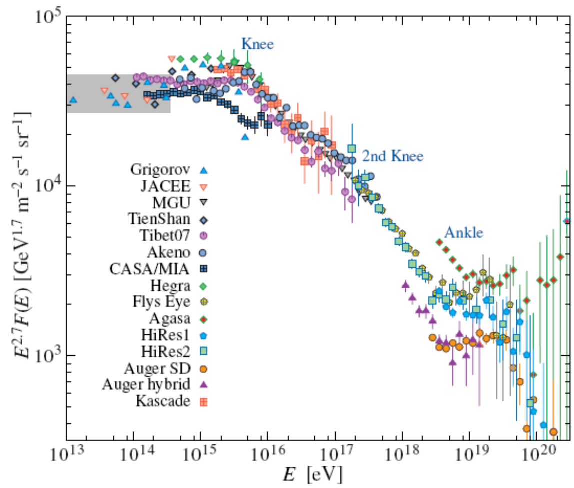

Figure 1.3: Multi-experiment measurements of the cosmic ray flux. The flux on the y-axis is multiplied by $E^{2.7}$, so that the "knee" and "ankle" are more visible. The energy is given on the x-axis in a log scale. [2]

galaxy. The maximum energy to which protons are accelerated is limited by the magnetic field and gyro-radius (radius in which they can be accelerated and are still bound by the magnetic fields) of the SN and the charge of the particles (equal to the particle number Z), following

$$E_{max} \propto B \cdot r \cdot Z. \tag{1.2}$$

Heavier nuclei can therefore be accelerated to higher energies because of their higher charge, which explains a lowering in flux above these energies.

At the "ankle" where the flux flattens again to an $E^{-2.7}$ spectrum [3], the particles are believed to originate from extra-galactic sources, as their gyro-radius will increase with energy, until $r_{gyro} > R_{galaxy}$ at which they cannot be accelerated further by our Galaxy. Candidates for these extra-galactic high energetic sources are so-called Gamma-Ray Bursts [8] (see chapter 2).

Studies of the Auger [9] and HiRes [10] experiments observe an abrupt suppression of cosmic rays at energies higher than 10^{20} eV. This effect can either be explained by the maximum available energy in cosmic acceleration regions, but is probably the result of the so-called **Greisen – Zatsepin – Kuzmin effect** (GZK cutoff) [11], which already in 1966 predicted the interactions of high energetic protons with photons of the 2.7 K Cosmic Microwave Background radiation (CMB). In this process, the $p + \gamma$ produce pions, protons or neutrons via the Δ-resonance following,

$$p + \gamma_{CMB} \rightarrow \Delta^+ \rightarrow \pi^0 + p \tag{1.3}$$

$$p + \gamma_{CMB} \rightarrow \Delta^+ \rightarrow \pi^+ + n \tag{1.4}$$

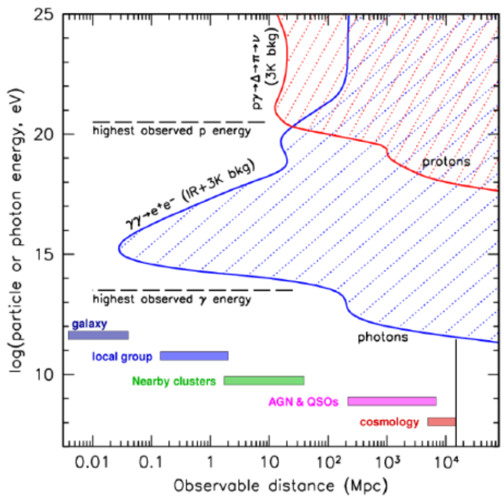

Figure 1.4: Observable distance as a function of energy for protons and photons [12]. Lines indicate the maximum distance at which the photons and protons can be detected, as a function of the energy, which is given in log scale on the vertical axis.

The CMB photon density is very low, which limits this effect for only those protons that travel more than an effective scattering length of several Mpc. This effect is illustrated in Figure 1.4, where the observable distance is shown as a function of the energy. Above approximately 10^{20} eV no protons can be observed that have traveled more than 10 Mpc because of their interaction with the CMB radiation. In these interactions charged and neutral pions are produced that decay into neutrinos and muons or high-energy photons respectively. Because the neutrinos will not be affected by CMB radiation, no GZK cutoff is expected and thus the detection of neutrinos with energies above 10^{20} eV will confirm the GZK effect.

In spite of major steps towards understanding the flux and composition of highest energetic cosmic rays, theories on the acceleration mechanisms that could explain such high-energy charged particles remain unverified. Several potential acceleration mechanisms will be discussed below, and the analysis presented will give a possible method of differentiating between the credibility of some of these theories.

Cosmic Ray Acceleration

Over the years numerous ideas have been brought up to explain the power law nature of the cosmic ray spectrum observed at the Earth. **top – down** scenarios exist that relate ultra-high energy cosmic rays to decay products of super massive particles with long life times, originating from the Big Bang. However, results of the Auger experiment, which investigates the ultra-high energy air-showers, show that these models are difficult to consolidate with their results [13]. More acceptable models describe the acceleration in a $\mathbf{bottum - up}$ manner, considering massive exploding astrophysical sources to be the most probable source of high-energy cosmic rays.

Enrico Fermi's theory, derived in 1949 [14], was the first serious step towards a comprehensive explanation of how cosmic rays are accelerated in a simple exploding star model, using a general line of reasoning. The idea is that particles gain energy by interaction with particles of an accelerated shock region. This increase in energy will be energy-dependent as their interaction time (τ_{acc}) decreases for higher energy, as the particles will move faster and interact more. The number of incoming particles is steady, and the escape probability is a Poisson process which is (almost) energy-independent, given by the escape time τ_{esc}. The particle distribution will be a power law given by

$$dN/dE \propto E^{-(1+\tau_{acc}/\tau esc)}, \tag{1.5}$$

as the particles gain energy at a rate of $dE/dt = E/\tau_{acc}$ and the escape rate per particle is τ_{esc}^{-1}.

This can be illustrated by a simple analogy. We consider a game where gamblers join continually, in which they are able to increase their winnings by a small fraction f with a probability of (1-p), or loose everything with a probability of p ($<<$ 1), after leaving the game. Provided that $f < p$, the number of gamblers that win some amount w before inevitably losing everything, is proportional to $w^{-p/f}$, the required power law [15].

In this first idea of Fermi, the particles gained energy by elastically colliding with particles in a gas cloud, which moves with speed u_{cloud}. Assuming the particle is relativistic, having a speed of $\backsim c$ (the speed of light), the relative energy difference after leaving the gas cloud will be $\backsim \pm(u_{\text{cloud}}/c)$. But because the chance of a head-on collision is bigger than a head-to-back collision by a fraction of $\backsim (u_{\text{cloud}}/c)$, the energy increase will be favorable over a decrease in energy [16]. The energy gain is therefore $\backsim (u_{\text{cloud}}/c)^2$, hence called the "second order" Fermi acceleration, see Figure 1.5

Quickly after the proposed scenario of Fermi in 1949, it became clear that his idea was not enough to explain the efficient acceleration mechanism needed for the high-energy cosmic rays. However the theory became a foundation for a first order Fermi acceleration mechanism, derived mathematically by Lieberman and Lichtenberg [18]. The method was further developed by Bell [19], Bladford and Ostriker [20], Krymskii [21] and Axford et al. [22] to describe the astrophysical process of shock acceleration. Both the first and second order Fermi acceleration processes are schematically drawn in Figure 1.5. In the first order Fermi acceleration scenario, a shock front is considered moving with a relativistic speed to the right. These shock fronts are formed by explosive phenomena such as a supernova explosion of a GRB, which will be explained in detail in section 2.

The system can be divided in two regions, separated by the shock front. The

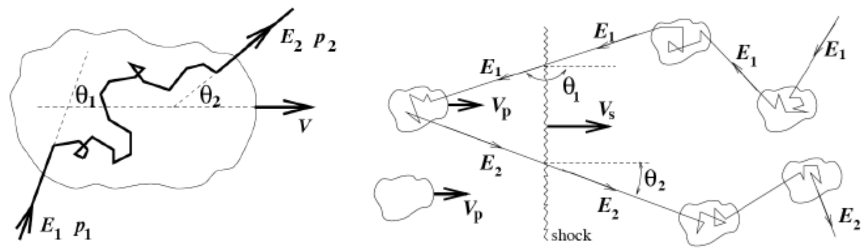

(a) Second Order

(b) First Order

Figure 1.5: Schematic views on the principle of first and second order Fermi acceleration [17] mechanism. More detail can be found in the text.

downstream region (illustrated on the left of the shock wave) will move towards the upstream region as the shock front will drag the gas clouds along. A particle that travels back and forth across the shock front, will encounter a push from the gas clouds on the left, and gain energy according to

$$\frac{\Delta E}{E_0} \backsim \beta_{front}. \tag{1.6}$$

Here E_0 is the initial energy of the particle and β_{front} the speed of the shock wave divided by the speed of light, c. Due to strong magnetic fields along the shock front, charged particles are believed to be forced across the shock front n times, after leaving the acceleration region with a final energy E_f given by

$$E_f = E_0 \left(1 + \frac{\Delta E}{E}\right)^n E_f = E_0 \left(1 + \frac{\Delta E}{E_0}^n\right) \tag{1.7}$$

To reach an energy E thus requires $n = \frac{ln(E/E_0)}{ln(1+\Delta E/E_0)}$cycles. Taking p as the escape probability for a certain time window and N_0 the number of particles trapped in the acceleration region from the beginning, the number of remaining particles thus follows

$$N = N_0 p^n. \tag{1.8}$$

The proportion of particles which is accelerated to an energy higher than E is given by

$$\begin{aligned} N(> E) &= \sum_{i=n}^{\infty} (1-p)^i \\ &= \frac{(1-p)^n}{p} \\ &= \frac{(E/E_0)^{-s}}{p} \end{aligned} \tag{1.9}$$

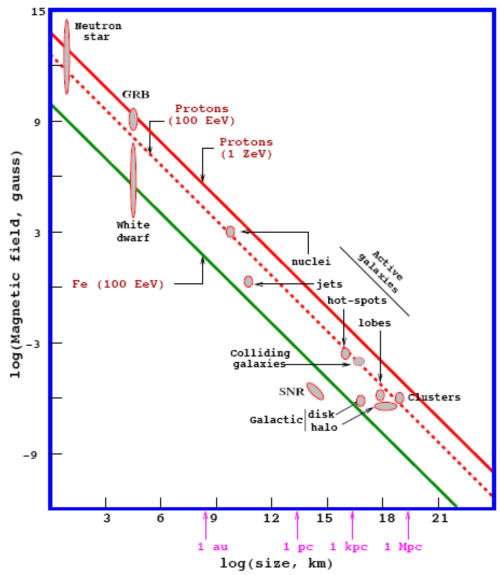

Figure 1.6: Hillas plot for astrophysical point sources [23]. The log scaled size is drawn on the horizontal axis and the log scaled magnetic field on the vertical axis.

with $s = -ln(p)/ln(1 + \frac{\Delta E}{E})$. The differential energy spectrum can now be written as:

$$\frac{dN(E)}{dE} = const. \times E^{-s-1} \tag{1.10}$$

The observed value for cosmic rays (after correcting for the energy-dependent escape from the host Galaxy) is $s \simeq 1.1$, yielding a spectral index of 2.1. The scenario explained above gives a reasonable outcome, as the measured flux at Earth has a spectrum of 2.7. The difference can be explained by assuming that the escape probability p increases with the acquired energy and the fact that the accelerated particles will also undergo various other effects when propagating through the cosmos.

Astrophysical Point Sources

The question remains in what kind of violent environment such a first order Fermi acceleration mechanism could take place. Several potential astrophysical phenomena are schematically drawn in the so-called Hillas plot of Figure 1.6 [23]. The Hillas plot shows that the maximum energy for accelerated particles is limited by the magnetic field B and the radius of a specific source, following equation 1.2.

A Gamma-Ray Burst is believed to be the most promising production site for ultra-high energy charged particles. Gaining more understanding and experimentally verifying these mechanisms is the underlying goal of the analysis which will be presented.

1.3 Neutrino Physics

The difficulty in identifying the direct source of the cosmic rays, is that charged particles do not travel in a straight line towards our detectors. In our universe, weak magnetic fields in the intergalactic medium deflect charged particles, changing their direction of motion. The cosmic rays will therefore never point back to their sources, but are randomly distributed across the sky, see Figure 1.7. Only at the highest energies ($\sim 10 - 100$ EeV) does this deflection become so small that a source direction could be inferred.

Exploding stars can be detected by the light they emit. The light will point back almost directly to the source, as their direction is only deflected by the gravitational fields. However, light is often blocked or decreased in flux by interstellar dust. Furthermore, photons will be absorbed by pair production with the CMB photons and Compton scattering with electrons of interstellar dust. The arrival probability depends on the mean free path of the photons, which is energy depended. In Figure 1.4 the observable distance for protons and photons as a function of the particle's energy is shown.

It is noted that the photons and protons have their disadvantages as cosmic messenger, due to the fact that energetic radiation (X-rays and gamma rays) of distance objects are easily absorbed, and charged hadrons (like protons) will not point back to their original source. Furthermore, as energetic electrons and positrons are easy to detect through the synchrotron and Inverse Compton radiation they emit, it is almost impossible to infer the acceleration of energetic hadrons along with electrons and positrons by a GRB from observed radiation. To determine if GRBs are the source of ultra-high energy cosmic ray particles, we need a method other than investigating the energetic radiation or cosmic rays alone.

Fortunately there is a particle which also can be used as a cosmic messenger, namely the neutrino. The neutrino has a very low mass, has no electrical charge and has a very small cross-section, which enables it to travel through the cosmos without being blocked by any obstacle. Like the photons, it will only be deflected by the gravitational fields. This will not form a problem in neutrino experiments, because the photons and neutrinos from the same source will be deflected in the same way by the gravitational fields, and thus point back to the same point in the sky.

The fact that the neutrino interacts hardly with anything, is also its great drawback when it is to serve as a cosmic messenger. Because of the low cross-section of a neutrino, one needs an enormous detector with a large interaction volume to enlarge the chance of an interaction of the neutrino in the detector. Without interacting near or in the detector, the neutrino will remain invisible.

A neutrino can have and oscillates between three different flavors, namely ν_e, ν_μ and ν_τ. It can interact with a nucleus via the weak interaction, exchanging either a neutral Z^0 boson or a charged $W^{\pm}$ boson yielding a neutral current interaction or charged current interaction, respectively. In case of the neutral current interaction, a neutrino with its original flavor plus a hadronic cascade are produced. In regard of a charge current interaction, a lepton (e, μ or τ) with the flavor of the original neutrino is produced as well as a hadronic cascade. The detector is sensitive for light which is produced by the hadronic cascade via Bremsstrahlung as well as Cerenkov light produced by the leptons (muons and taus). When a muon or tau travel through a medium with a speed larger than the speed of light in that medium, Cerenkov light is emitted. As such, neutrino detectors generally use large volumes of transparent matter enabling it to detect light which is emitted by secondary particles which are produced in neutrino interactions with matter.The IceCube neutrino telescope, used for my analysis, uses a $\sim km^3$ volume of ice of the Antarctic as transparent medium. Numerous optical photo-multipliers are placed deep in the ice, which detect photons emitted by the secondary particles. Further details on the detection methods of neutrinos and on the detector are given in chapter 3.

For point source analyses, like the GRB analysis presented here, directional information of the original neutrino is crucial. From all secondary particles formed by a neutrino interaction, only muons are able to travel a substantial distance through the detector (the lifetime of a tau is too short). Therefore, as a (high-energy) muon emits Cerenkov light along its path through the detector, a reconstruction of its track can be made. The direction of the muon will be almost the same as the original neutrino at high energy, thus only ν_μ will be used in the analysis presented here.

Not only muons from ν_μ interactions will travel through our detector, as numerous muons are produced in cosmic ray air-showers. These muons typically travel downwards through the detector in the same direction of the air-showers. Unlike muons, neutrinos are able to traverse through the Earth, possibly inducing a muon that travels upwards in the detector. This principle is used to reduce nearly all background events in our detector, by only using the so-called "upgoing" tracks. Thus, for the GRB analysis presented here, only GRBs that lie in the Northern Sky are taken into account. However, also neutrinos are produced in cosmic ray air-showers. These neutrinos that are formed by air-showers in the Northern Hemisphere sky are able to induce an "upgoing" muon in the detector, and are difficult to eliminate from GRB signal neutrino events.

1.4 Overview of the Research and Analysis

This report will describe an analysis which is performed on data from the IceCube neutrino telescope. The detector is built in the ice of the Antarctic, comprising of a $\sim km^3$ scale volume detector which makes it the largest neutrino detector on Earth. This neutrino telescope is primarily devised to detect neutrinos in an energy range of about 10-100 TeV [25]. It will search for astrophysical point sources of energetic neutrinos, such as Gamma Ray Bursts or Active Galactic Nuclei (AGN). In addition, studies on neutrino oscillations can

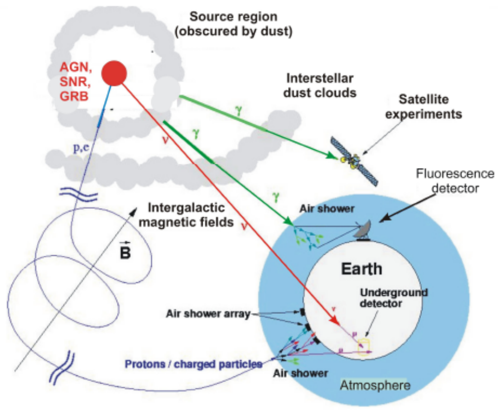

Figure 1.7: Various ways of observing distant objects [24]

be performed, galactic supernovas are studied and indirect dark matter searches are undertaken. Since the majority of the neutrinos crossing the detector are atmospheric neutrinos from cosmic ray interactions at the top of the atmosphere, IceCube is also used for cosmic ray studies in conjunction with IceTop, a water-based Cerenkov detector located on the surface.

Numerous Universities and institutes are combined within the IceCube collaboration. The research described in this paper was performed in the Brussels group of the collaboration. Apart from GRB studies, dark matter research, point source analyses and lower energy neutrino studies are the main focus of this research group.

This report describes an analysis of a potential neutrino signal from GRBs that were detected between April 2008 and May 2009. A two-hour window is taken around each GRB event to search for any neutrino signal. Events within two-hour windows of every GRB that passed several data-stability criteria are stacked, so that a possible neutrino signal will add up constructively in our time profile. The assumption is made that the time difference between the photons and neutrinos is uniform for all the GRBs in our sample due to a generic production mechanism.

The mechanisms and different theories of Gamma-Ray Bursts are described in chapter 2. In chapter 3 a full overview is given of the IceCube detector. How the data is analyzed, and what kind of algorithms are used to derive a track reconstruction will be summarized in chapter 4. Moreover, a comparison and optimization is provided for the so-called $feature-extractor$, the algorithm that analyses the recorded waveforms of Cerenkov photon pulses and determines the timing and the photoelectric charge induced by a one or more Cerenkov photons. Furthermore, at the end of chapter 4, several selection criteria are described to eliminate background events. These criteria are used in the analysis to arrive at the final data-sample. In chapter 5 the statistical method of the analysis is presented, and a possible improvement on the analysis is proposed. Chapter 6 reviews the criteria for a consistent data-sample and discusses the final data-set and GRB catalog. An "un-blinding" procedure which has to be followed before one is allowed to look at the final data-set lay beyond the scope of this research, which prevented a disclosure of a possible discovery or calculation of an upper-limit on the flux. Nevertheless, in chapter 7 the the sensitivity of the analysis of the final data-sample is discussed, as well as an outline for further improvement.

Chapter 2

Gamma Ray Bursts

Gamma-Ray Bursts (GRBs) are among the most violent and spectacular astrophysical phenomena known to mankind, apart from the Big Bang. Their cosmological distance to the Earth, in combination with the high luminosity in gamma rays, X rays and, in some cases, visible light point to the most violent regions in our Universe. To understand how massive objects could produce such high energies, and investigate a possible link between the GRBs and the ultra-high-energy cosmic rays, scientists have examined these objects for decades, with numerous instruments. This chapter gives an overview of where we stand with our knowledge on these objects, and what neutrino physics can contribute to this field of research.

2.1 Introduction to GRB observations

In 1967 satellites of the project Vela accidentally observed GRBs for the first time, while they scanned the Earth for possible test detonations of nuclear weapons that were banned by the *Partial Test Ban Treaty*, allowing only underground nuclear tests. The satellites were equipped with scintillators sensitive to photons in the energy range from (0.2-1.5) MeV, and observed unexpected large bursts of photons. Because of their angular precision of a few degrees, the possibility of having the Earth or Sun as sources were ruled out [26].

Theorists came up with numerous ideas to explain the phenomena, but not until 20 years later the first GRB experiment started on the Compton Gamma Ray Observatory satellite with the Burst and Transient Source Experiment (BATSE) [27]. The experiment concluded with two main discoveries.

First, the BATSE experiment on the Compton GRO showed that GRBs can be divided into two groups, so-called $\mathbf{long-bursts}$ with a duration of $\geq$ 2s and $\mathbf{short-bursts}$ with a duration of $\leq$ 2s, see Figure2.1(a). The duration is measured by the parameter T_{90} , which determines the time it takes to accumulate 90% of the total flux, from 5% up to 95% of the detected photons. The $long-$ and $short-bursts$ are believed to be differentiated by their progenitors, although they will result in similar phenomena that form a GRB, this is further explained in section 2.2.

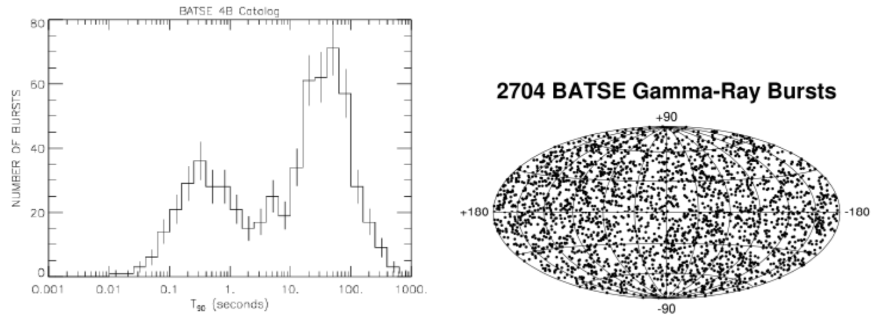

(a) (b)

Figure 2.1: (a) illustrates the bi-model distribution of the duration of GRBs. (b) shows the directional distribution of 2704 GRBs which were measured by the BATSE experiment.

Secondly, as shown in Figure 2.1(b), all of the 2704 detected GRBs were distributed isotropically over the sky, indicating that the sources lie either outside our galaxy or very close to the Earth. Would they have been located throughout our galaxy, then the distribution would have been clustered around the galactic plane, where most of the hundred billion stars of our Galaxy reside. The possibility that the GRBs lie very close to the Earth was excluded when the redshift could be determined for some GRBs by the Dutch-Italian satellite BeppoSAX, which was launched in 1997 [28] to investigate Galactic X-Ray sources (accreting binaries) and AGNs. The satellite was able to observe the X-ray afterglow of some GRBs, further improving the determination of the position of a GRB (the so-called *error box*), which enabled the identification of a *host galaxy* for some GRBs. The diffuse emission of the host galaxy could then be determined, and the redshift calculations of the host galaxies concluded that the GRB lie at cosmological distances from Earth.

The SWIFT satellite was launched in 2004 for further investigation on GRBs and has detected the majority of the GRBs used in this analysis. Around a hundred GRBs are detected each year by the SWIFT satellite. The detector was built to study GRBs in a range of different wavelengths. It can also observe the afterglow for a small fraction (25%) of the GRBs, which enables the determination of the red-shift for a few GRBs that are used in the analysis.

With the Burst Alert Telescope on the SWIFT satellite, photons in the energy range of 15-150 keV are detected with a precision of 4 arcminutes. An alert signal is send to the X-ray Telescope (XRT), the UV/Optical Telescope (UVOT) and the Gamma-Ray Burst Optical/Near-Infrared Detector (GROND). These detectors quickly aim at the GRB position and detect light in the range of 0.2-10 keV and 170-650 nm respectively. The latter detectors can determine the position of the GRB even further to a 0.3-5 arcsec. This is more than sufficient for a neutrino analysis, as the accuracy of our track reconstruction will not become better than about 0.5 degree.

A further improvement on GRB observations was started with the launch of the Fermi Gamma Space Telescope in July 2008. This satellite combines a wide window Gamma-Ray Burst Monitor (GBM) that detects up to 200 GRBs per year, with a Large Area Telescope (LAT) that provides a better position determination.

2.2 Standard GRB model

Although numerous observations have been performed on GRBs, the theories on their origin and underlying mechanisms have up to today not yet been proven, and can be very different in their approach. This is peculiar in modern astronomy, as pulsars, quasars and X-ray sources were theoretically understood within a few years, or even months after their discovery. This is probably due to the fact that GRBs are such extreme transient phenomena with a large variety of characteristics and because they are highly unpredictable.

A few characteristics however are considered to be generic. GRBs come from other galaxies. They are the most energetic sources known in our Universe, emitting photons with a total energy of $\sim 10^{51} - 10^{53}$ ergs in a few seconds. Because of their extra-galactic origin, only one GRB per million years per galaxy is detected at Earth, when we assume the rate of GRBs does not change with cosmological time. It could however be possible that the rate of GRBs could change with the cosmic evolution.

Fortunately, there exists a widely agreed theoretical concept that is used to explain the high luminosity and the low detection rate of the GRBs. In this model, two oppositely directed jets form from a short-lived accretion disk of matter circling around a black hole. The matter in the accretion disk fuels the "inner engine" until a relativistic outburst of the matter in the form of $e^{\pm}, \gamma$, and possibly baryon plasma, is ejected along the rotation axis forming the jets. This model is called the "fireball" model, which describes a beamed version of the original spherical fireball model [29] (see Figure 2.2). The beamed model reduced the expected total energy involved in the outburst by a factor $\Omega/4\pi$, where Ω is the opening angle of the collimated jet, compared with earlier estimates that assumed a spherical explosion. As such the luminosity becomes more comparable with other astrophysical phenomena like Active Galactic Nuclei (AGN).

The bulk matter in the jet moves with relativistic speeds, where the radiation will be concentrated conically towards the direction of motion of the matter in the observer frame, because of the aberration effect (beaming). The GRBs are therefore only visible when the line of sight to the detector falls within the opening angle of the jet, which enlarges the true GRB rate by a factor of $4\pi/\Omega$ compared to the spherical explosion models.

The relativistic speed of the jet is proven by the non-thermal spectrum that

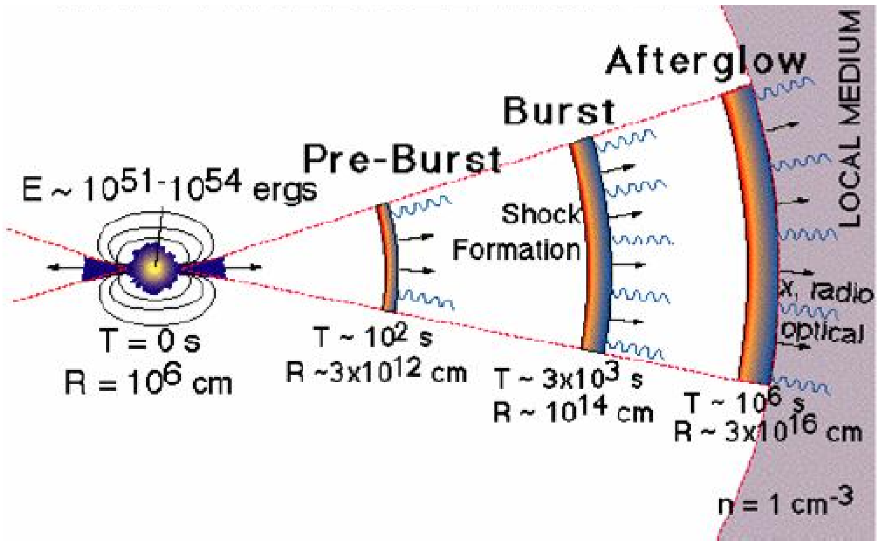

Figure 2.2: GRB fireball evolution with shock formations in the jets. More details are to be found in the text.

is observed for the photons of a GRB. In a 'naive' model with a non-relativistic jet, the photon density should be large to explain the rapid variation in photon brightness observed at Earth. This 'naive' scenario predicts an *opaque* fireball where the photons will produce electrons and positrons via pair production, resulting in a thermal equilibrium of photons and e^-e^+ pairs. Only the outer layer of the photon-pair fireball will radiate a *Black Body spectrum* (*Planck spectrum*). Such a spectrum has a typical exponential cut-off, which is **not** observed at Earth, as rather a $power - law\ spectrum$ is observed with photon energies much larger than the pair production threshold. In a relativistic jet model, the observed time between the arrival of subsequent photons is contracted so that the predicted photon density at the source is much lower. Therefore the fireball will be transparent, resulting in an observed power law spectrum [30] [31].

As bulk matter in the jet is emitted it will pave its way through outer regions of the star, evolving from an optically thick and relativistic hot plasma to a colder and optically thin plasma from which photons are able to escape. Possibly shock/bow waves are formed proceeding the jets, allowing shock acceleration processes to be present (see section 1.2). The speed of the bulk matter will decrease due to interaction with matter in the outer regions, decreasing aberration effects, and thus widening the opening angle of the jet. This could explain the large variances in luminosity and fluences which have been observed for different GRBs [32]. A detector could detect the radiation from a GRB jet in a later stage, where the opening angle becomes wide enough so that the GRB can be detected, or the luminosity falls faster due to the widening of the opening angle of the jet.

Two scenarios have been devised that explain the formation of a short-lived accretion disk around a black hole, namely the *hypernova scenario* and the *merger scenario*. The two scenarios explain the bi-model distribution of the duration of GRBs. The *hypernova scenario* [33] is used to explain the long-bursts GRBs, where a black hole is formed inside the nucleus of a massive star ($M > 20{-}30M_{\odot}$) that collapses at the end of its thermonuclear life. The core of the star collapses to a neutron star and the outer regions explode incompletely. The exploding matter is not able to reach into space, and falls back onto the collapsed core. The core will accumulate this vast amount of mass, collapsing further into a black hole after it has exceeded its maximum mass for a neutron star ($M_{ns} \leq 2 - 2.5M_{\odot}$ depending on different models). The rotation of the progenitor star is essential, as it will ultimately result in the fast rotation of the in-falling material, creating a short-lived accretion disk around the newly formed black hole. Due to friction in the accretion disk, the matter will fall into the black hole, and two oppositely directed jets of relativistic matter are formed that propagate away from the black hole in the direction of its rotation axis. The details on the formation of jets near a black hole and a short-lived accretion disk remain unclear, although jets seem to be formed regularly in these circumstances.

The short-bursts of GRBs are believed to originate from a *merger scenario* [34], where two neutron stars or a neutron star and a black hole collide. A collision is inevitable when two dense objects rotate rapidly around their common center of mass and lose energy due to the emission of *gravitational waves* [35]. When the stars collide, a black hole is formed, possibly combined with a short-lived accretion disk that ultimately produces two jets that result in a GRB.

The two models that describe the formation of a GRB are principally different. A distinctive phenomenon can be observed in the hypernova scenario, where a supernova is produced because the jets will blow apart the stellar envelope surrounding the black hole: the typical emission for a supernova where light in other wavelengths than gamma-rays can be observed some 30 days after an explosion is visible, only for some long-bursts (hypernova scenario) GRBs [36].

Acceleration of matter in jets

Although the fireball model is widely accepted, the features of the outflow of matter in the jets is still quite controversial. The observed photons are believed to be produced by Synchrotron radiation of the emitted electrons. Some models do not require the acceleration of particles other than $e^{\pm}$, which are captured by strong electromagnetic fields, so-called Poynting flux [18], possibly accompanied by (low energy) neutrinos. Other models however describe an acceleration process of several charged particles (electrons as well as protons or nuclei), which move with relativistic speeds [8]. The particles are accelerated either by internal mechanisms in the "inner engine" only [37] [38], or by shock accelerations like first order Fermi acceleration [19] [20] [21] [22], explained in section 1.2. As

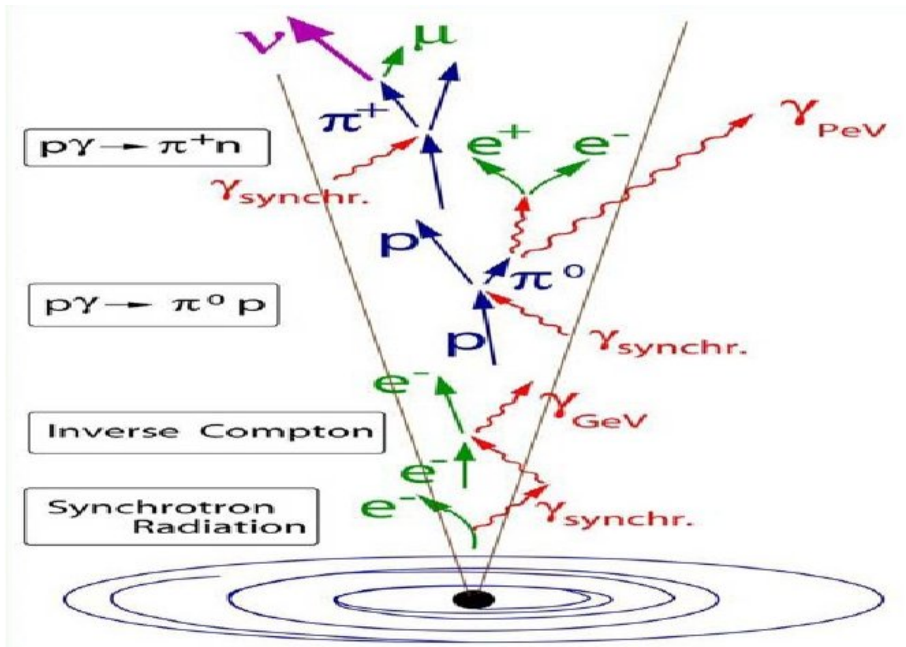

Figure 2.3: The production scheme for high-energy particles and photons is drawn in relativistic jets. Further details can be found in the text.

will be shown below, a clear differentiation of the models can be obtained by neutrino experiments, as a high-energy neutrino signal will only emerge when hadrons are accelerated in this process.

Furthermore, afterglow studies established a GRB-Supernova connection in a few bursts by seeing the emergence of spectral features also seen in a detected Supernova at the position of the GRB [36].

2.2.1 Neutrino Production

The observed energetic X-ray photons are expected to be produced by electrons that are accelerated in the fireball jets, either via Synchrotron radiation or Inverse Compton scattering. Along with these accelerated electrons, some models predict that also hadrons (mainly protons) are accelerated. The accelerated protons and neutrons can produce pions via a Δ-resonance;

$$\begin{aligned} p + \gamma \rightarrow \Delta^+ &\rightarrow n + \pi^+ \\ &\rightarrow \pi^0 + p \end{aligned} \tag{2.1}$$

$$\begin{aligned} n + \gamma \rightarrow \Delta^0 &\rightarrow \pi^0 + n \\ &\rightarrow \pi^- + p \end{aligned} \tag{2.2}$$

The neutral pions will more or less instantly decay in high-energy photons contributing to photon radiation, whereas the charged pions yield muons, electrons and high-energy neutrinos, providing a distinctive signal for the hadronic model:

$$\begin{aligned}
&\pi^0 \rightarrow \gamma\gamma \\
&\pi^+ \rightarrow \mu^+ + \nu_\mu \rightarrow e^+ + \nu_e + \bar{\nu}_\mu + \nu_\mu \\
&\pi^- \rightarrow \mu^- + \bar{\nu}_\mu \rightarrow e^- + \bar{\nu}_e + \nu_\mu + \bar{\nu}_\mu
\end{aligned} \tag{2.3}$$

These reactions are summarized in Figure 2.3. According to these interactions, the ratio of the neutrino flavors at the production site will be $(\nu_e, \nu_\mu, \nu_\tau) = (1 : 2 : 0)$. This ratio changes to (1:1:1) due to neutrino oscillations along their path to the detector [39]. The analysis presented in this report only makes use of the ν_μ signal, which yields a muon traveling in almost the same direction as the neutrino for high energies, in case the neutrino interacts with a nucleus. Unlike other secondary particles formed by the neutrino interaction, the muon will travel a substantial distance in the detector. The Cerenkov light that is emitted by muons while traversing the detector, is detected and enables a track reconstruction, see chapter 3 for further details.

2.2.2 Energy Considerations

In non-thermal relativistic jets from a GRB, the above mechanisms can produce protons which are Fermi accelerated to energies above 10^{20} eV [8]. As shown above, this can result in an accompanied burst of neutrinos which are produced by $\pi^\pm$ production from photon-proton interactions. The energy of the prompt neutrinos (produced along with the gamma-rays) is therefore correlated with the photon (e_γ) and proton (e_p) energy, above the Δ resonance threshold, following [40] [41]

$$e_\gamma e_p = 0.2 \text{ GeV}^2 \Gamma^2 \tag{2.4}$$

where the Lorentz factors of the expanding fireball are $\Gamma > 10^2$. Using observed values for the photon energy (~ 1 MeV), protons with energies of $\sim 2 \times 10^6$ GeV will enable the production of neutrinos from pion decay via the Δ resonance. The $\pi^\pm$ is expected to get $\sim$ 20% of the proton energy, which leaves each neutrino with around 5% of the initial proton energy, yielding an energy around 10^{14} eV.

As the neutrino energy is correlated with the photon and proton energy, it largely follows the observed photon energy spectrum of GRBs [41]. The photon energy spectrum can often be fitted by a so-called Band spectrum [42]. The fit can be described by a power-law with an exponential cutoff $E^\alpha \times exp(-E/E_0)$ for lower energies and a steeper power-law given by E^β with $\alpha > \beta$ for higher energies. This shape is in agreement with predictions from the synchrotron model, taking into account processes like self-absorption and the energy losses of the radiating electrons and/or positrons.

The neutrino spectrum is given by the famous Waxman-Bahcall spectrum. Below the first energy break at 5×10^{14} eV, the pion production is not very

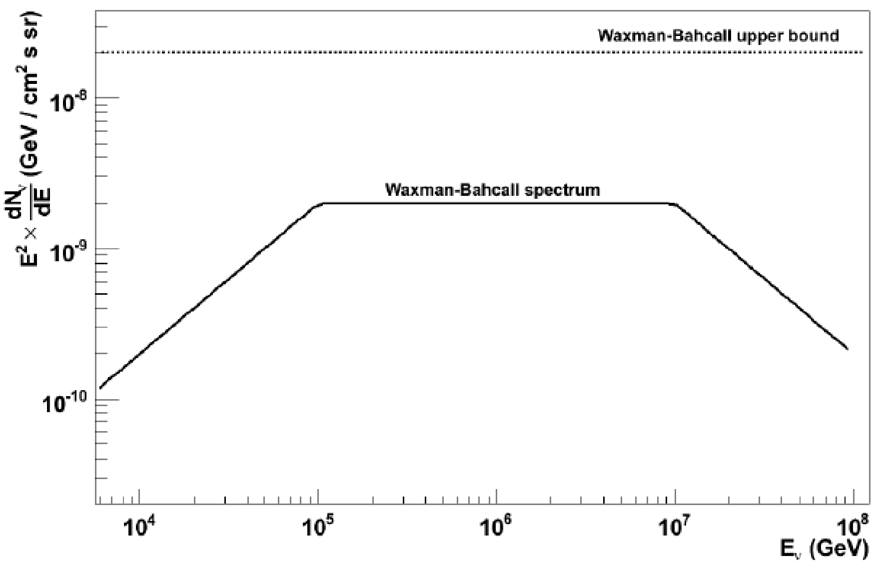

Figure 2.4: The Waxman-Bahcall energy spectrum for neutrinos and their independent upper-bound are illustrated here. The horizontal axis gives the log of the energy, and on the vertical axis the flux is given.

effective due to the Δ resonance threshold. The spectrum steepens above 5×10^{15} eV because charged pions (like electrons) suffer synchrotron losses in a magnetic field, as well as muons (intermediate particle from equation 2.3) due to Cerenkov radiation, concluding with the following Waxman-Bahcall spectrum;

$$\frac{dF_\nu}{dE} = f_\nu \times \begin{cases} (E_\nu/\epsilon_\nu^b)^{-\alpha_\nu} & , for\ E_\nu < \epsilon_\nu^b \\ (E_\nu/\epsilon_\nu^b)^{-\beta_\nu} & , for\ \epsilon_\nu^b < E_\nu \leq \epsilon_\nu^s \\ (E_\nu/\epsilon_\nu^b)^{-\beta_\nu}(E_\nu/\epsilon_\nu^e)^{-(\alpha+2)} & , for\ E_\nu \geq \epsilon_\nu^s \end{cases} \tag{2.5}$$

where $A_\nu = 2\times10^{-19}GeV s^{-1} sr^{-1} cm^{-2}, \alpha_\nu = 1, \beta_\nu = 0, \epsilon_\nu^b = 10^5$ GeV and $\epsilon_\nu^s = 10^7$ GeV. The spectrum is drawn in Figure 2.4, as well as an independent upper bound given by [43]

$$\frac{dN_\nu}{dE_\nu}E_\nu^2 < 2\times10^{-8}GeV/cm^2s\ sr. \tag{2.6}$$

The Waxman-Bahcall spectrum has specific values for each GRB, but falls within the uncertainties of different GRB models. The Waxmann-Bahcall limit uses the observed spectrum of ultra-high energy cosmic rays (assumed to be protons) to derive an upper limit on the neutrino flux, assuming a common origin. As such, it is independent of the details of the various GRB models.

The spectrum of neutrinos is important for the data-simulation process. The simulation data-sets provide further understanding on the detector and on the experimental data. In stead of a Waxman-Bahcall neutrino spectrum, a generic E^{-2} neutrino spectrum was used in this report to simulate the signal produced in the IceCube detector, through the muons generated in interactions of the neutrino with atoms in the bedrock below the detector. The simulation process is explained in more detail in section 4.5. Further details can be found in section 4.5. The simulation of E^{-2} neutrino signal data is readily available in the collaboration because of other more general studies on the neutrino signal. The production of a personal simulation data-sample lay beyond the scope of the presented research, but would not have made a big difference as the spectra are very comparable and thus the detector response is almost identical, as has been shown by M.Duvoort [24].

2.2.3 Precursor, Prompt and Afterglow Neutrino Signal

Neutrinos are expected to be produced in various stages of the GRB, predominantly via photon-hadron interactions described by equations 2.1, 2.2 and 2.3. Therefore neutrinos can be classified into three different groups, namely precursor neutrinos, prompt and afterglow neutrinos, arriving before, simultaneously and after the observed gamma-rays.

Low energy (sub GeV) precursor neutrinos are produced by the core collapse that initiates the GRB. Because the neutrinos have such a low cross-section, they can escape at this early stage unlike photons or any other particles. Furthermore, precursor neutrinos can be detected with an energy around 10 TeV that are produced by proton-neutron (and proton-proton) interaction in a spherical supernova wind[1] [44]. This model is supported by BATSE and SWIFT that detect X-ray photons before the gamma-rays for some GRBs. Moreover, the relativistic bulk matter, which forms the jets in the fireball model, will travel through the outer layers surrounding the core collapsing supernova or neutron star merger. At first the hot plasma travels through the optical thick region from where only neutrinos can escape, yielding a precursor neutrino signal that is produced by the photon-proton mechanism explained above, with energies around 10^{14} eV.

The relativistic jet will become optically thinner as it expands, at which point photons can escape. Prompt neutrinos that are produced along with the photons via photon-proton interactions are expected to arrive roughly in the same time as the gamma-ray photons (time dilation effects and the difference in speeds can be neglected, see section 5.1) with an energy of about 10^{14} eV.

Because a clear afterglow of X-ray, optical and radio photons have been observed, several mechanisms are still in play at that time. The afterglow is believed to come from synchrotron radiation of electrons that are accelerated in shocks moving inwards. These shocks will also accelerate protons to high energies. The combination of low energy photons ($\sim 10^2$ eV) with high-energy protons result in ultra-high-energy neutrinos (~ 10 PeV) [40].

[1] The pressure in the explosion will accelerate electrons, protons and neutrons. The neutrons are not decelerated by magnetic fields and collide with protons before they decay, producing $\pi^{\pm}$ that decay as described in equation 2.3

Because little is still certain about the features playing a role in the evolution of the GRB, an analysis method is chosen to be as model-independent as possible. The analysis presented here is capable of discovering a prompt, precursor and/or an afterglow neutrino signal, on one condition, that the signal neutrinos have a coherent time at which they are produced with respect to the gamma-ray production. As such, the possible neutrino signal is expected to cluster in our two-hour time window for every GRB.

Chapter 3

IceCube detector

Because of the low cross section (weak interaction) of the neutrino, and the fact that the neutrino has no charge, it can act as an important messenger. The neutrino will travel in a straight line across the Universe, pointing back directly from where it was produced. Here we neglect the possible deflection from gravitational fields, which is equally deflecting the observed photons from the source, from which its position is deduced. However, the low cross-section also makes a neutrino very hard to detect, as it will easily traverse a detector without interacting. This chapter focuses on the mechanisms used to detect a neutrino, and how the IceCube detector is built in the ice of the Antarctic, providing an experimental framework to discover (high-energy) cosmic neutrinos.

3.1 Neutrino interactions with matter

A neutrino will only reveal itself by two possible reactions with ordinary matter via the weak interaction. The weak interaction in particle physics is described by the exchange of the weak gauge bosons. The neutral Z^0 boson used in the neutral current interaction, and the exchange of a charged $W^{\pm}$ boson will produce a charged current interaction. In neutral current interactions the neutrino with flavor l will scatter with a nucleus N and produce a hadronic cascade X, given by

$$\nu_l + N \rightarrow \nu_l + X \tag{3.1}$$

Detectors are sensitive for photons produced in the hadronic cascades, and so detect the neutrino indirectly. A more promising way of detecting the neutrino is using the charged current interactions where the neutrino produces a charged lepton of the same flavor l, as well as exciting a hadronic cascade X;

$$\nu_l + N \rightarrow l + X \tag{3.2}$$

Here not only the hadronic cascade can be detected, but also the charged lepton, being either a *muon*, *tau* or *electron*. Each flavor will leave a specific signature in the detector, summarized in Figure 3.1. Loosing energy along their paths, the leptons will emit light that can be detected by the optical photo-multipliers in the ice, the so-called Digital Optical Modules (DOMs) (see section 3.3). Whereas the tau and electron will not travel a large distance in the detector, the muon typically travels several kilometers before decaying [45]. By detecting the emitted Cerenkov light of the muon along its path, see section 3.1.3, the direction of the muon can be reconstructed, providing a method to determine the arrival direction of the neutrino. The *tau* and *electron* will not provide a good directional reconstruction, but on the other hand they can provide a better energy reconstruction as all the energy is lost inside the volume of the detector. In a search for point sources such as GRBs, only muon events are used as the determined arrival direction is crucial for the analysis.

In the charged current interactions, most of the energy of the neutrino will be converted to the outgoing lepton. Because of the additional hadronic cascade present in the interaction, the direction of the lepton will not be exactly the same as that of the neutrino, but has a deviation of $0.7°(\frac{E_\nu}{TeV})^{-0.7}$. For a neutrino with an energy of 100 TeV this deviation in direction is approximately 0.03°, which allows us to determine the direction of the ν_μ by reconstructing the muon track.

3.1.1 Background events

Cosmic rays that produce a cascade of particles in the atmosphere will also produce muons (and other leptons) which traverse the detector. In neutrino signal analyses like the GRB analysis described in this report, these muon events are considered background. Cosmic ray muons will only travel downwards through the detector, as they are produced in the atmosphere above, and cannot traverse the whole Earth. These events are calles "down-going"events. Neutrinos on the other hand are very well capable of traversing through the Earth before interacting, and can therefore produce an "upgoing" muon. All the reconstructed tracks that point downwards in the detector are therefore considered as background events, which implies that the analysis is limited to GRBs on the northern-hemisphere sky.

Furthermore, cosmic rays will also produce neutrinos, which are able to travel through the Earth and interact in our detector. These background events are harder to eliminate, as they are also able to produce "up-going" muons in our detector. These events can be partially eliminated because they have a relative lower energy than the expected neutrinos from GRBs, which results in a different signal in our detector (see section4.4). Even more background reduction is obtained by using the position of the GRBs, and filtering out every event that does not point back within a certain *opening angle* around the GRB position. Because these background neutrino events are isotropically distributed across the northern hemisphere sky, such a position cut will eliminate most of these background events.

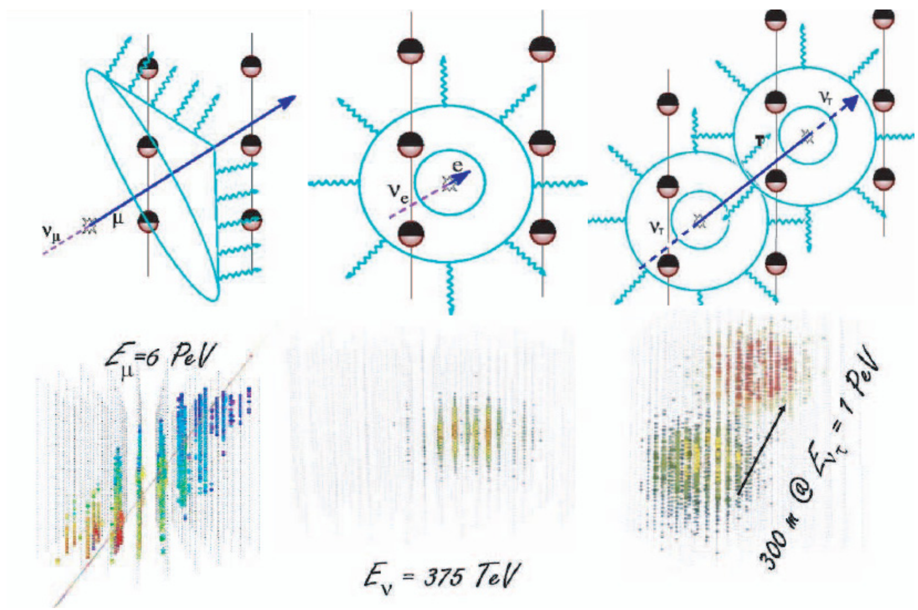

Figure 3.1: Schematic view of the experimental signatures of charged current interactions of all different neutrino flavors in the IceCube detectr [46]. From left to right: ν_μ,ν_e,ν_τ. The dots show the different optical DOMs employed in the ice, which detected a light signal from the interaction. The color scheme is from red over green to blue and indicates the time of the hits in each DOM, where the red dots indicate the early hits. The electron neutrinos will produce electrons which themselves induce an electromagnetic cascade, producing a spherical wavefront of light, boosted in the direction of the incident neutrino. The muon neutrinos induce a muon with a cascade, outside or inside the detector. The muon will traverse through the detector, emitting Cerenkov light along its path (see text). The tau neutrinos first induce a cascade and produce a tau, which decays fast due to its short lifetime. An other cascade is formed by which again a tau-neutrino is produced. The neutral-current interactions are not shown here. They will leave a similar signature as the electron neutrino due to the hadronic cascade which is produced.

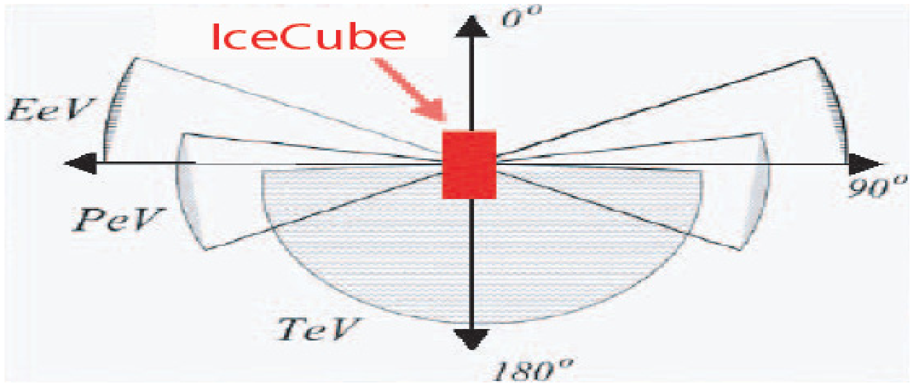

Figure 3.2: Schematic view of the energy sensitivity range of the IceCube detector. Because the Earth filters out the cosmic ray muons, only neutrinos are expected to penetrate through the Earth. Thus the detector is only sensitive for neutrinos in the energy range of TeV coming from below, so-called $\mathbf{up-going}$ neutrinos. Because of the increasing cross-section of a neutrino with higher energies, the neutrinos are not able to traverse the Earth, but will stand out of the cosmic ray background events due to their energy. More information is found in the text.

3.1.2 Energy Sensitivity

The cross-section of the neutrino (and the anti-neutrino) increases more or less linearly with the energy [47]. The probability for the neutrino to interact near our detector therefore increases with energy, which partly compensates the decreasing flux for high-energy particles, see section 1.2. The IceCube detector is built to detect neutrinos in the TeV-PeV energy range coming from the northern hemisphere sky, see Figure 3.2. The DeepCore component will lower the energy threshold to about 10 GeV, see section 3.2. Due to the increasing cross section the Earth becomes opaque for the very high-energy neutrinos, but the high-energy leptons produced by interactions of these ultra-energetic neutrinos will stand out from the background cosmic rays because of their high energy, which make them visible for the detector provided that the neutrino interaction takes place close to the detector[1].

3.1.3 Cerenkov light

When a charged particle, like a muon, passes through a dielectic medium with a speed greater than the speed of light in that medium (c/n), light will be emitted by the particle. For the discovery of this effect, Pavel Alekseyevich Cerenkov received the nobel price in 1958 and the effect was named after him.

[1]If the interaction lies far away from the detector, the incident muon will have lost its exceptional amount of energy

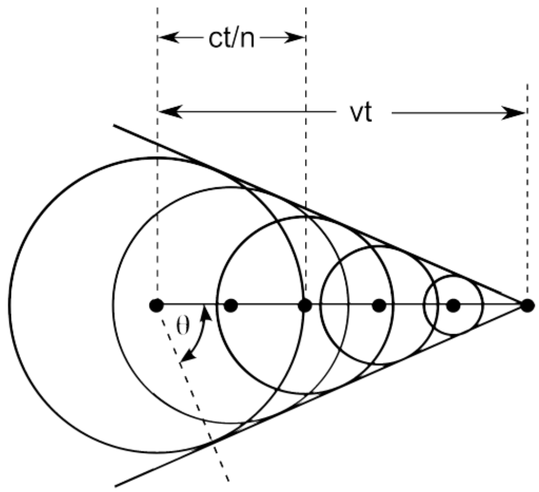

Figure 3.3: Huygens construction of a Cerenkov cone induced by a charged particle traveling with a speed v that is larger than the speed of light in that medium c/n.

The principle of the Cerenkov light can be explained by elementary electrodynamics. The charged particle that traverse through a medium will displace electrons in the medium, bringing them off equilibrium. When the electrons fall back to their original state, light is emitted. Due to the fact that the particle travels faster than the light in this medium, the light interference is constructive, much like a plane traveling faster than the speed of sound. The light will travel through the medium as a cone with a specific angle to the direction of the particle, given by

$$cos(\theta) = \frac{1}{\beta n} \tag{3.3}$$

where β is the speed of the particle v divided by the speed of light$c$, and $\beta n > 1$. See Figure 3.3 for a schematic summary. From the arrival time of the Cerenkov light at different optical modules, which form the detector sensors, a track can be reconstructed to determine the direction of the muon, and hence the direction of the incident neutrino.

3.2 The IceCube detector

Most neutrino telescopes have a transparent medium as a basis to allow the Cerenkov light to be detected by an array of photo-multiplier tubes (PMT). Water basins can be used like in the Kamiokande experiment, but due to the falling flux for higher energetic particles (see section 1.2), and a low interaction rate of a neutrino, a large volume is needed to detect a significant amount of (high-energy) neutrinos. Larger water-based detectors were built in a sweet water lake by the Russian-German Baikal experiment [48] and in the Mediterranean, the ANTARES experiment [49]. A similar but by far the largest neutrino detector is built in the ice of the Antarctic, the IceCube detector.

The IceCube Neutrino Observatory is the world's largest neutrino telescope and will be completed in 2011. It uses the ice of the Antarctic as a transparent medium and, when completed, will have a volume of around 1 km^3. Figure 3.4 gives a schematic view of the detector. The completed detector will consist of 4800 so-called Digital Optical Modules (DOMs, see 3.3) that are buried in the ice at a depth of 1450 m to 2450 m. The main part of the DOM is a large PMT. They are attached to strings with a vertical spacing of 17 m. Each string holds 60 DOMs, and the strings are placed in a hexagonal lattice structure with a spacing of $\sim$ 125 m so that the detector volume is optimized. The strings are deployed by drilling a straight hole in the ice with hot water. The strings are lowered before the water freezes the DOMs in position.

The installation of IceCube started in 2005 with the first string. In 2006 the detector grew to 9 strings (IC9), to 22 strings (IC22) in 2007 and after the deployment season in 2008 consisted of 40 strings (IC40). Each year a separate data-set was produced, and analyzed. The analysis presented here uses data of the IC40 detector. A schematic outline of the IC40 detector array can be found in Figure 3.5. In 2009 the detector consisted of 59 string (IC59), growing further to 79 strings in 2010. The detector will be completed in 2011, consisting of 86 strings (including the DeepCore components mentioned below). In this final setup IceCube is sensitive for neutrinos with energies ranging from about 100 GeV to a few EeV [50].

The IceCube detector is further improved by the extension of the so-called DeepCore (DC) strings, which will lower the energy threshold to 10 GeV. The six DeepCore strings are deployed in the lower center part of the detector, where the ice is very clear. Because their smaller vertical separation of 10 m for the upper 10 DOMs, and 7 m vertical separation for the lower 50 DOMs, low energetic muons can be detected. A further advantage is that with the DeepCore strings it will be possible to look for neutrinos coming from the southern hemisphere, by using a so-called $\mathbf{veto-algorithm}$ based on the surrounding standard IceCube strings. This veto-algorithm eliminates background down-going muons that pass through our detector, by investigating the signal in the upper region of the detector. A neutrino traveling down in the detector can interact in the lower part, leaving only a signal in the DC region. However, a muon that travels downwards in the detector also shows up in the upper part of the detector. Down-going neutrinos can thus be distinguished from the background cosmic ray muons, and potential point sources on the southern hemisphere can therefore be investigated.

Besides the in ice detector part of IceCube, a surface air shower detector IceTop has been built at the surface. It consist of 160 tanks, situating 2 tanks per inlet of a string. The tanks are filled with ice and have two DOMs per tank. This part of the detector is built to investigate cosmic ray showers, and can be used in addition to the in ice detector.

3.3 Digital Optical Modules

The fundamental elements of the IceCube detector are the Digital Optical Modules (DOMs). These DOMs are built to detect single photons with a ns accuracy and they are all synchronized with each other. Figure 3.6 is a schematic view of the DOM, with the 25 cm Hamamatsu Photo-multiplier Tube built in a 35.6 cm in diameter glass sphere. The DOM achieves high accuracy and a wide dynamic range by internally digitizing and time-stamping the photon signals before transmitting the digital data to the surface [46]. The devices can be calibrated and tested separately in situ, which is important because the DOMs are inaccessible after deployment, and will need to withstand high pressure and low temperatures for over 15 years. Rigorous testing is performed on the DOMs before they are deployed.

The DOMs have three different read out channels, in which a waveform is saved.The Analog Transient Waveform Digitizer (ATWD) is the main readout channel and samples the analog waveform of the PMT to a digital one, with a set speed of 3.3 ns, allowing acquisition of 422 ns long waveforms. For a longer acquisition time, the DOM has a Fast Analog to Digital Converter (FADC) channel, which saves a waveform that has a bin size of 25 ns, spanning a total time window of 6400 ns. Moreover, the three highest 25 ns bins of the FADC waveform are recorded yielding a so-called Soft Local Coincidence (SLC) waveform. For most isolated DOMs in an event, no ATWD and FADC waveform is recorded, although a SLC waveforms will be stored for every DOM that detects a photon.

DOM calibration and pulse feature extraction

The waveforms that are digitized and transmitted to the surface have to be analyzed. First, the waveforms are calibrated, setting the baseline to zero and incorporating the correct event time. The pulses in the ATWD and FADC waveforms will coincide due to correct DOM calibrations.

Then pulses are extracted by a $feature - extractor$ (FE) algorithm (see 4.1.2) that determines the beginning of a pulse (the Leading Edge, LE), its width (Time Over Threshold, TOT) and integrated charge (Analog to Digital Converter, ADC value). A typical waveform and pulse are shown in Figure 3.7. The pulses can be determined with ns precision, which enables the detector to know very accurately when and where the Cerenkov light was detected, creating a basis for the track reconstruction (see section 4.3).

Triggering the events

To reduce the data volume, the DOMs will only transmit data if a certain trigger is passed. The DOMs are able to communicate between their top and bottom neighbors, which is used in the trigger system. Only if a DOM has a neighboring

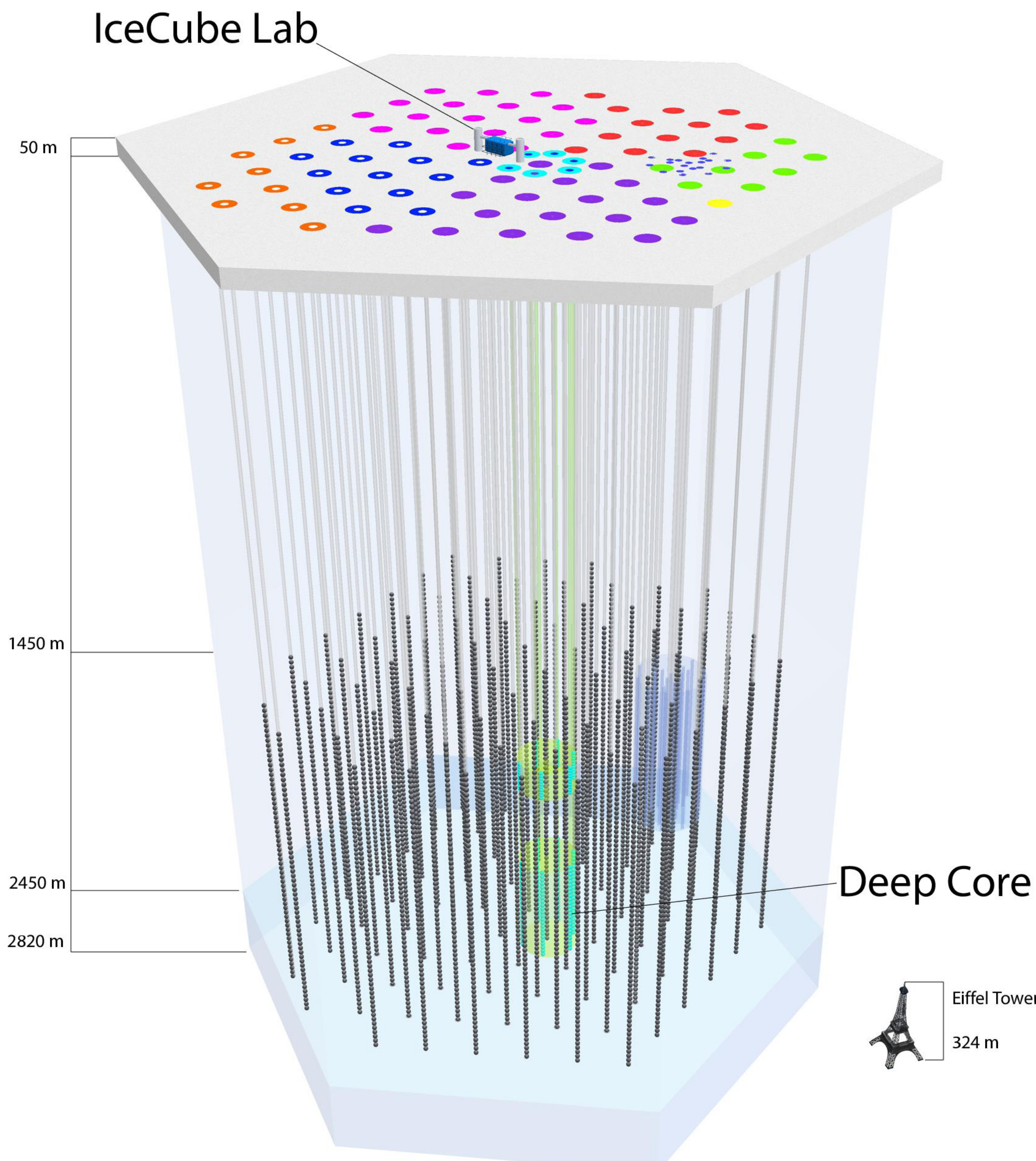

Figure 3.4: A schematic view of the IceCube detector [50]

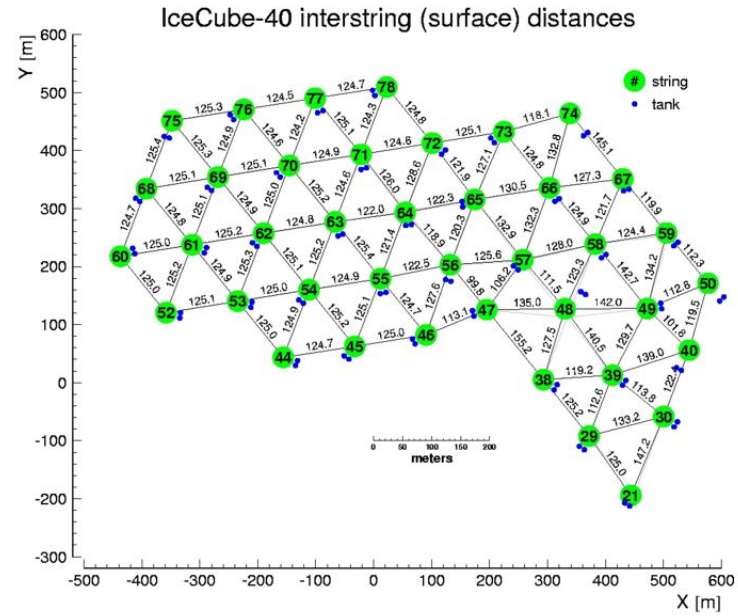

Figure 3.5: The top view of the IC40 detector array. Data of the detector with this geometry was used in this report.

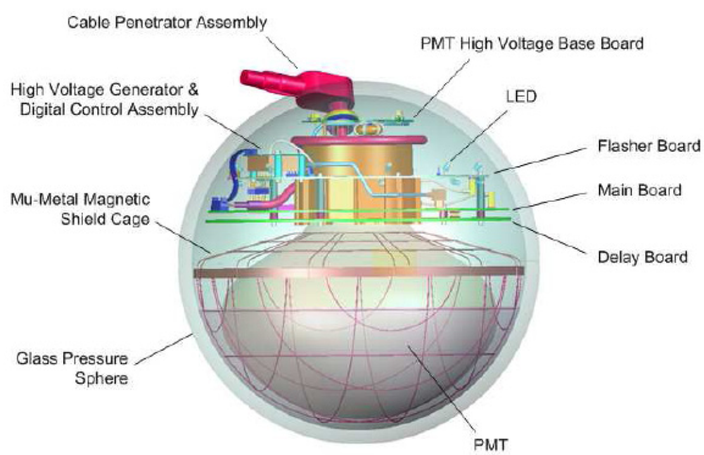

Figure 3.6: A schematic view of an IceCube Digital Optical Module (DOM) [46]

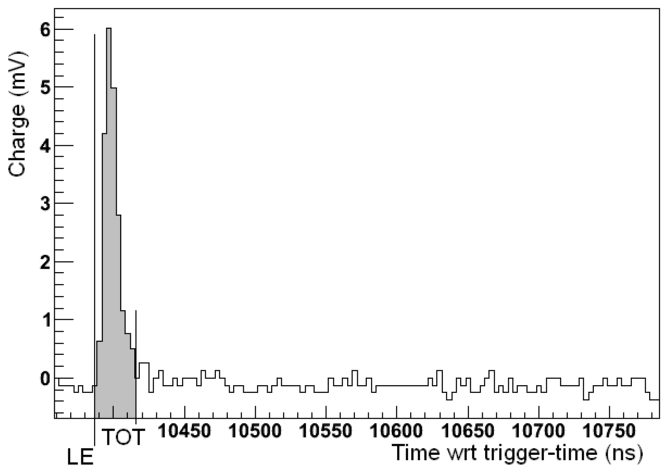

Figure 3.7: A waveform is illustrated here. The time with respect to the trigger-time is given in ns, and the charge in mV. The Leading-Edge (LE) is given by the vertical line, and the Time Over Threshold (TOT) determines the duration of the pulse. The pulse is integrated, which gives the total charge (ADC value) of the pulse. This pulse is typically a single photon-electron (single PE) pulse.

DOM firing within a certain time, the DOM will save the waveform and transmit it to the surface. This will trigger an event, where all DOMs that detect a photon and lie close to other fired DOMs (on the same string or on neighboring strings) provide full ATWD and FADC waveform information, which yield so-called Hard Local Coincidence (HLC) hits. Other DOMs detecting a photon that lie more isolated (i.e. having no neighboring DOM that fires) will only transmit a so-called Soft Local Coincidence (SLC) hit, which does not include a full ATWD or FADC waveform, but only a three bin SLC waveform. This limits the data volume of an event.

In the surface data-acquisition (DAQ) station all the waveforms are stored for further analyses [51]. For the IC40 detector, the trigger rate is about 550 Hz. This rate has to be scaled down by several filters at the South-Pole ("online filtering") before the data is sent via satellite to the Northern Hemisphere for more elaborate investigations, see section 4.4.

3.4 Software

The basic processing software in the IceCube collaboration is built in a highly modular framework called *IceTray* [52]. The framework provides base classes for low level calibration and feature extraction as well as high level analyses methods, in a Python environment.

However, the software package, used for the analysis presented in this report, is a separate ROOT based software package, IcePack. It was developed by Nick van Eijndhoven in 2001 in Utrecht, and was based on the NCFS package used by the ALICE collaboration in CERN [53]. The structure is made such that the user is able to combine the low level information of the detector directly with a top end analysis research. This stand alone software package comprises of a separate feature extractor that was optimized to work with the IceCube waveforms and contributed to the improvement of the general feature extractor now used by the IceCube collaboration. This is summarized in section 4.1.2.

Chapter 4

Reconstruction and Simulation

Nearly all triggered events in the IceCube detector consist of events not related to cosmic neutrinos. The vast majority is "reducible" background, and consist of muons, originated from cosmic rays. Because these muons travel downwards through the detector, they are easily eliminated by taking only events coming from the Northern Hemisphere, using the Earth as a physical filter. Since the IceCube observatory is located at the South Pole, these events are dubbed $up-going$. The "irreducible" background events however consist of background neutrinos, also originating from cosmic rays, but now from the Northern Hemisphere. Unlike muons, these neutrinos will not be filtered out by the Earth. To reduce this type of background, we employ a narrow angular window around the GRB position, taking only tracks which point back within a few degrees of the GRB (section 4.6.2). The key to succes, however, lies in the reconstruction of the tracks (section 4.3), and is limited by the quality and accuracy of this reconstruction. After passing several trigger and filter levels (section 4.4), and with the best reconstruction algorithms available for the IC40 configuration (section 4.3.2), the final data-sample is still dominated by atmospheric muons traveling downwards through the detector. This is because the tracks of these muons were $mis-constructed$, and point back to a point in the Northern Hemisphere, with the possibility of falling within the opening angle around the GRB position (see Figure 4.14). Furthermore, atmospheric neutrinos will also traverse through the Earth, giving rise to a uniform background over the whole sky. Fortunately, the probability distribution function (pdf) of several (quality) parameters of these background events is substantially different from those of the signal events due to the mis-construction and energy difference of atmospheric neutrinos. This enables us to enlarge the signal over background ratio by applying some cuts on these parameters (see section 4.6.2). The parameter cut values are determined by comparing "off source" experimental data, all consisting of background events, with simulated signal events. This is further explained in section 4.5.

The track reconstruction algorithms of the IceCube detector use the arrival-time of the Cerenkov light emitted by the muon. As was explained in section 3, the DOM will give a signal when detecting a light pulse. From this signal the specific time and amplitude need to be extracted, before a track reconstructing can be performed. Using so-called hit-cleaning methods, noise hits[1] are removed, which improves the track reconstruction substantially. Intuitively, extracting all the hits with their most exact timing will improve the track reconstruction, although this effect is not always very evident, as shown in section 4.1.3.

4.1 Hit extraction

The Cerenkov light from the muon will induce an electrical signal in the DOM, which is recorded as a waveform. This waveform will have a specific shape, length and height. It is analyzed to determine the correct arrival time and amplitude (i.e. integrated charge) of the light pulse, the so-called feature extraction. The feature extraction will determine the hit time, the so-called leading edge (LE), the integrated charge (ADC value), and the time over threshold (TOT) that is equal to the length of a pulse. In Figure 3.7 these features are clearly shown for a simple pulse. When dealing with more 'elaborate' pulses, i.e. waveforms with more than one pulse that cannot be easily distinguished because they lie to close to each other, the task of extracting a reasonable LE, ADC and TOT for each pulse becomes more complicated.

There are a few analytical modules available for this task. The feature extractor used on the data of this thesis was the general IceCube feature extractor module (FE) that was written by Dmitry Chirkin [54]. It was developed in 2003 and had its first release for the standard IceCube software (IceTray) in 2005, where it was used until 2010. In 2010, a new or updated feature extractor (NFE) was developed by Marius Wallraff [55], which will be used as a general feature extractor for IceCube in the coming years. In the same year, a third feature extractor, originally developed to analyse the AMANDA waveforms, was updated to work with the pulses from IceCube, in Brussels. This third feature extractor, the IcePack feature extractor (IcePackFE), is a stand alone algorithm that runs as a module in the ROOT based package, IcePack [56]. For comparison reasons of different analyses and consistency in the data, it is important to use one standard, robust and stable algorithm. Furthermore, the applied method is required to be the same as the one run on-line at the South-Pole (i.e. for filtering) where only limited computing power is available. In the analysis presented here the original feature extractor (FE) is used. However, the development of the updated IcePackFE not only helped me to gain a better understanding of the low level features of the data, but also discovered some disadvantages concerning the general FE and NFE. Moreover, for the IC59 data, the follow-up

[1] Noise hits are either caused by electronics in the DOMs, or are isolated hits which cannot be linked with the muon because they lie at unphysical time and distance from where the muon traveled through the detector.

of the IC40 configuration, also pulses from the FADC signal were extracted. Combining the hits of the two signals posed problems in the timing extraction because of the used feature extractor. By using the IcePackFE this issue can be analyzed objectively. In the following section a short outline is given on the IcePackFE, and a comparison is made between the three different methods.

4.1.1 Standard Feature Extractor and New Feature Extractor

As both IceTray feature extractors are not developed nor improved by the author, only a short summary and the possible pros and cons of the method will be given here. For a total overview and in-depth description of the algorithms that are used, the reader is referred to [55].

The FE and NFE are both incorporated in the IceTray software framework [52]. These two feature extractors are based on the same algorithms. Different algorithms are devised and optimized for specific waveforms. The so-called first and second single-pulse algorithms are used for "simple" AWTD waveforms. The first and second multi-pulse algorithms extract hits from "complex" ATWD waveforms containing more than one hit and is based upon the method of Bayesian Unfolding, [57]. The FADC waveforms are analyzed by a specific FADC algorithm and an algorithm is devised for the SLC waveforms.

Because different algorithms are used for different types of waveforms, a $pre-evaluation$ algorithm is needed to determine the waveforms complexity. This pre-evaluation method is called "Eva" and will flag a waveform as being a "simple", "complex" or "slc" waveform. Every group will then be analyzed by its own algorithm. The basic idea behind this method of using multiple algorithms for different waveforms, is that it will speed up the hit extraction procedure without lowering the performance, which is essential for the online processing at the South Pole. Simple waveforms are analyzed quickly, and do not need a more time-consuming algorithm than complex waveforms.

The single pulse extraction algorithm for "simple"waveforms is based on a threshold method, fitting the rise of a pulse with a parabolic curve. The intersection of this parabolic fit and the threshold will result in the leading edge time of the extracted hit. The trailing edge time is given by the time the pulse falls below the threshold, indicating the end of the pulse. The charge of the pulse, the ADC value, is now calculated by integrating the pulse from the LE to the TE.

As mentioned, the multi-pulse algorithm for "complex" waveforms is based on the method of Bayesian Unfolding described by G. D'Agostini, [57]. As stated in [55], the aim of the Bayesian Unfolding method is to undo smearing and distortion effects caused by the experiment's hardware. The method of the unfolding technique is based on fitting the waveform by a sample of single photon-electron pulses (single PE), dividing bigger pulses into single PE pulses. In theory, this method is capable of extracting the build-up of a big pulse, because each pulse is a combination of at least one single PE pulse, since one cannot have a physical pulse that is smaller than or different from a single PE

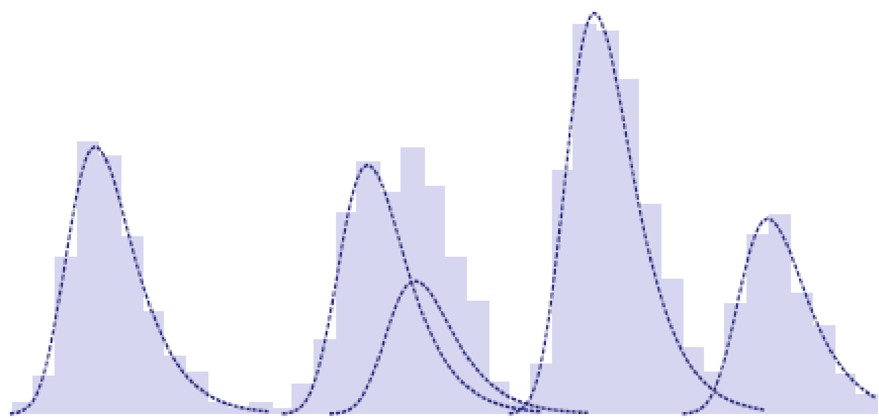

Figure 4.1: Several pulses are drawn in one waveform. The Bayesian Unfolding method is illustrated by the dashed lines that outline the determined pulses of the waveform, courtesy of Marius Wallraff [55]

pulse. An illustration for this method is given in Figure 4.1 where the waveform is build-up by five SPE like pulses.

4.1.2 IcePack Feature Extractor

The ROOT based software framework IcePack [56] also incorporates a feature extractor, the IcePack FE, which is based on a very different and independent method. This IcePack FE was developed by Nick van Eijndhoven and Garmt de Vries-Uiterweerd in 2007 at the Utrecht University [58]. At that time, it was devised for the AMANDA data. With the use of this feature extractor and other modules of the IcePack software package, a low level analyses of the data is possible by incorporating the raw and calibrated waveforms in the framework, as well as an end level analysis using all available track reconstructions and analyses methods available from the IceCube collaboration and ROOT framework. The IcePack FE was updated in 2010 at the Vrije Universiteit, Brussels, and compared to the FE and NFE for its performance and improvements, which will be described below.

The procedure that the IcePack FE follows is summarized in the flow diagram of Figure 4.2. The IcePack FE has a generic method to extract hits for all the different waveforms. Because the IcePack FE will calculate its own baseline, it is capable of extracting hits from both "raw" (uncalibrated) and "calibrated" waveforms. First, the waveforms are subjected to a *peak search* function that has been optimized for the waveforms of the IceCube detector. This search function uses several steps and algorithms to determine all the peak values of each pulse, which is described below in detail and summarized in the flow diagram. The peak values above a certain threshold, which is based on a baseline

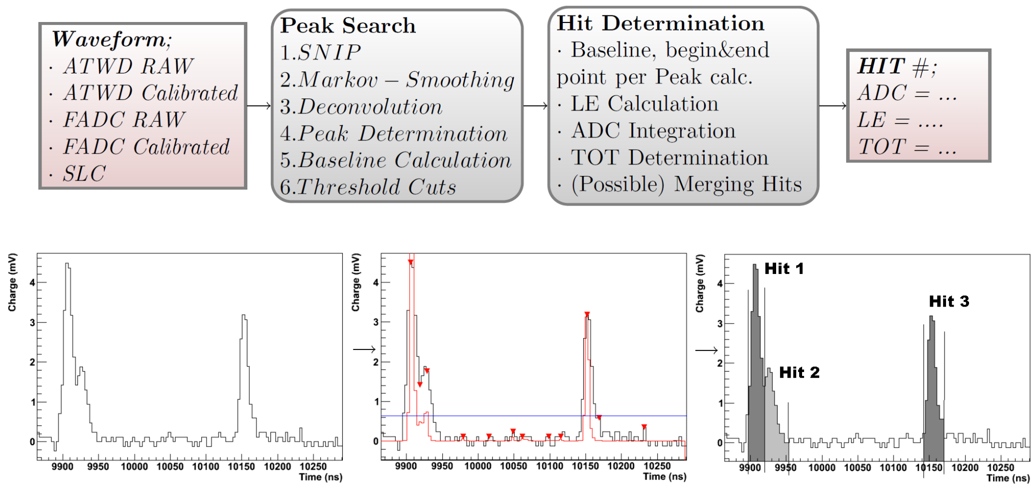

Figure 4.2: Flow diagram of the feature extraction procedure of IcePack. Starting with a specific waveform (here an ATWD calibrated waveform is illustrated), a peak search function is used to find all peak values of the waveform. These peak values are illustrated by the red arrows in the middle waveform. The search function uses different algorithms to find all the peak values, which are explained in the text. The peaks that pass the threshold cut (illustrated by the horizontal blue line in the middle waveform), will form the basis for the pulse extraction. The LE, ADC and TOT values are determined, recording all the necessary information for each detected hit. Further details on the feature extraction method is provided in the text.

determination of the waveform, are used to determine the hits. The starting point (Leading Edge (LE)) and end point (Trailing Edge (TE)) of every pulse is determined, as well as the Time Over Threshold (TOT) that is equal to the duration of the pulse, and the pulse is integrated to calculate its total charge (Analog to Digital Converter value (ADC)). When pulses lie very close together, and no apparent differentiation is possible, the pulses are merged, by adding their charge and combining the LE values. All of these specific steps followed by the IcePack FE are explained in detail in the following sections.

Peak Finder

The basis algorithm of the IcePack FE is the *peak search* function from the so-called *TSpectrum* [59] module of the ROOT framework [60]. The peak search function is built to identify all the peaks in each spectrum with the presence of the continuous background and statistical fluctuations. It is able to identify peaks close to the edge of the spectrum region and peaks of pulses that lie close together.

The flow diagram in Figure 4.2 summarizes the different algorithms used by the search function in chronological order. The search function is based on a deconvolution algorithm to find the peak values of every pulse. Before the deconvolution is performed, the function uses a background suppression method and then a so-called *Markov smoothing* algorithm to emphasize the pulses in the waveform. A short description on the methods used by the search function are provided here, including the specific predefined parameter values used for the (ATWD and FADC) IceCube waveforms (see table 4.1). Further details and references of the methods can be found in the documentation of the *TSpectrum* module [59] of the ROOT software package.

The background suppression algorithm is based on a so-called Sensitive Nonlinear Iterative Peak (SNIP) clipping algorithm. In short, this algorithm determines the background spectrum by taking an average over several number of bins, determined by a predefined clipping window that is set to the default value of three bins. Before the deconvolution algorithm is used to determine the different pulses in the waveform, the background spectrum is subtracted from the waveform.

A *Markov smoothing* method [61] is used to derive a new spectrum that emphasizes the peaks and suppresses statistical and background fluctuations even more. To illustrate the idea in short, we suppose a small ball, placed on the edge of an irregular well, illustrated on the left in Figure 4.3. A classical ball would be stopped by the first obstacle on the top left of the well, but if it was a quantum one it could penetrate through this obstacle (quantum tunneling) and proceed its way down into the well, finally oscillating at the bottom. The probability for the ball to jump to the left is $p_{left} = exp[(N_{i-1} - N_i)/\sqrt{N_{i-1} + N_i}]$ and for a jump to the right $p_{right} = exp[(N_{i-1} - N_i)/\sqrt{N_{i-1} + N_i}]$, where N_i are the number of counts in bin i. By letting the ball jump several times, and tracking the probability to end up in a point of the well, the structure of the bottom (or peak for that matter) is recovered. This is shown on the right side of figure 4.3.

To determine the peak values of every pulse of the waveform, a deconvolution algorithm is used. The deconvolution algorithm is able to decompose so-called multiplets, determining the built up of larger pulses by several smaller pulses. The deconvolution is based on the mathematical equation;

$$y(i) = \sum_{k=0}^{N-1} h(i-k)x(k), i = 0, 1, 2, ..., N-1 \tag{4.1}$$

where $h(i)$ is the impulse response function (presented in a $N \times N$ matrix form) and x and y are the input and output vectors, respectively. N is the length of the x and h vectors. The observed spectrum, given by y, is built up by the original spectrum x described by the response function h. To find the original spectrum x, the Gold deconvolution algorithm [62] is used[2]. This algorithm was derived in 1964 by Raymond Gold and uses an iterative unfolding method to determine an

[2]Several algorithms can be used to perform deconvolution of a waveform (Fourier, VanCittert etc), but the Gold algorithm is found to be the most stable [59].

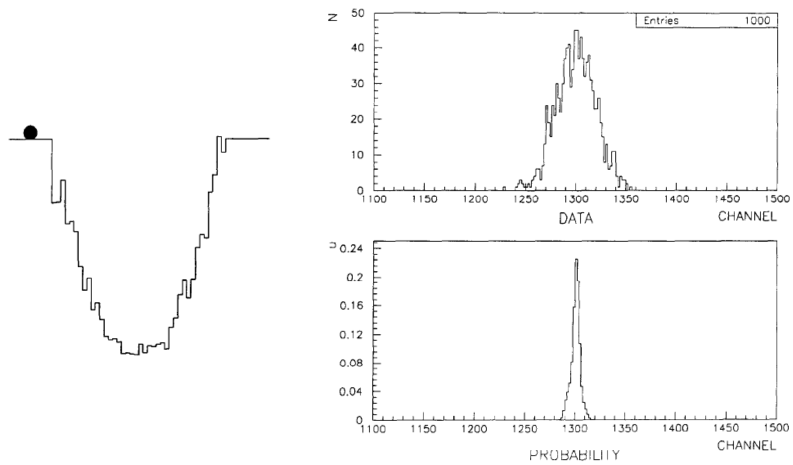

Figure 4.3: On the left, a illustrative example of a well that is used to describe the idea behind the Markov smoothing. On the right a Gaussian peaked dataset is drawn with its probability distribution $u(i)$ below [61]

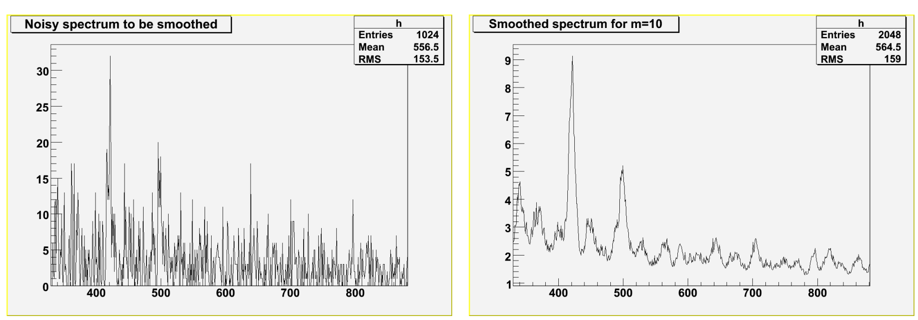

(a) Begin spectrum

(b) Smoothed spectrum

Figure 4.4: Two spectra are given, recorded in a specific time window. The effect of Markov Smoothing is shown by comparing the original spectrum with the smoothed spectrum, using an average window of 10 [59]

approximation of the responds function $h(i)$. In a iterative procedure, successive approximations of the response function $h(i)$ are generated that converge to the best approximate solution. The method starts with a arbitrary positive vector $x^{(0)}$ [3], from which an approximated response function h' can be derived following $h'_{ii} = x_i^{(0)}/y_i$. Using the initial equation 4.1, an approximated output spectrum y' is calculated. Successively, "next" order approximations of the input vector ($x^{(k+1)}$) are determined following

$$x_i^{k+1} = \frac{y'_i}{\sum_{m=0}^{N-1} h'_{im} x_m^{(k)}} x_i^{(k)}, \ i = 0, 1, ..., N-1 \tag{4.2}$$

For every approximation step (k), the response function h' is calculated. After several iterations, the response function will yield an appropriate function to describe the unfolding of the waveform, and enables determination of the correct peak values.

To illustrate the performance of the deconvolution algorithm, a waveform with several pulses is illustrated in Figure 4.5(a) and 4.5(b). The deconvolution spectrum is drawn by the red line, and the red arrows indicate the peaks in the waveform. In waveform (a), the large pulse on the left has been unfolded into one small pulse followed by a bigger pulse. Also the subsequent pulses are accurately decomposed. The pulse of waveform (b) has been decomposed in one large peak followed by a small second peak. The blue line indicates the threshold for the peaks, see section 4.1.2.

Peak function parameter values

Several parameters are defined for the different algorithms of the peak search function, summarized in table 4.1. The number of iterations used by the deconvolution algorithm is set to 50. The so-called sigma value is determined by the width of each pulse and indicates the minimum distance between subsequent peak values. This value is set to its minimum value of 1, which enables the identification of two pulses that lie at least one standard deviation value apart from each other. The total number of peaks that can be extracted are set to 100, and the minimum pulse height is set to 0, to ensure that all possible peaks are recorded.

The so-called $function\ threshold$ is defined as the minimum peak amplitude. The peaks need a higher amplitude value than 0.2% of the highest amplitude peak value in the waveform, to be recorded by the deconvolution algorithm. A second threshold is defined as the *peak acceptance level* that is based on the baseline plus its spread, see section below. All the peak values that lie above the peak acceptance level are used for the hit extraction procedure.

[3] The method starts with the vector $x = [1, 1, ..., 1]$.

Table 4.1: IcePack Feature Extractor Parameters

Parameter	IceCube waveforms	AMANDA waveforms
Deconv N-iterations	50	3
Sigma	1.	1.5
Max Peaks	100	10
Min Pulse height	0	50
Function threshold	0.2 %	5 %
Peak accept level	$Q_{baseline} + 5\times\sigma_{baseline}$	0

Baseline

After finding all the peaks in the waveform, the IcePackFE will proceed by calculating an "overall baseline". This baseline ($Q_{baseline}$) is equal to the vertical median of all the bins that are lower than 10 % of the maximum bin content. The spread of the median determines the $\sigma_{baseline}$ value. This is a very quick thumb-rule calculation, but robust enough for the feature extractor. All the peaks found by the search function with a higher amplitude than the *Peak acceptance level* ($= Q_{baseline} + 5 \cdot \sigma_{baseline}$) are used for the hit extraction procedure. This threshold is illustrated by the blue horizontal line in Figure 4.5.

When two pulses lie close together, the baseline for the subsequent pulse needs to be corrected. An $effective$ *baseline* is determined following

$$Q_{baseline\ effective} = f_{baseline} \times (Q_{lower\ boundary} - Q_{baseline}) + Q_{baseline}, \quad (4.3)$$

where $Q_{lower\ boundary}$ is the charge of the lowest bin between the subsequent peaks. The $f_{baseline}$ is set to 0.5, setting the effective baseline in between the original baseline and $Q_{lower\ boundary}$. This effective baseline is used for the Leading Edge calculation.

Leading Edge, Integrated Charge and Time Over Threshold

All peaks passing the *peak acceptance level* threshold are used for the hit extraction procedure. The IcePack FE will determine the LE, ADC and TOT values for every pulse. The waveform is divided into several regions that contain at most one pulse. The lower and upper boundary of the regions are defined by the bin with the lowest charge in between two peaks, or the begin and end point of the total waveform.

The leading edge (LE) is calculated by fitting a straight line along the steepest rise of the pulse before its peak value. This line is extrapolated down to intersect with the effective baseline or the overall baseline, whichever is the highest, resulting in the leading edge of the pulse.

The integrated charge (ADC value) is determined by integration over the pulse, subtracted by the overall baseline. The lower boundary of the integration is given by either the leading edge, or the lower region boundary of the pulse, whichever comes last. Accordingly, the pulse is integrated up to the upper region boundary or at the point where the waveform drops below the overall baseline, whichever comes first.

The so-called trailing edge (TE), indicating the end of the pulse, is determined by the endpoint of the charge integration. The Time Over Threshold (TOT) is then given by the $TE - LE$.

Merging pulses

The IcePackFE performs further "quality" checks on the pulses, merging the pulses if one of the values for the LE, ADC or TOT was ill defined. In the following situations this is done.

- When a peak is found to be located on the rising edge of a following pulse, and the adjacent bin to its right is equal or higher than the peak itself, it will be merged with the later pulse. Figure 4.5(a) is an illustrative example of this situation. The first peak lies on the rising edge of the following bigger pulse, making the charges and leading edges of both peaks ill defined. The LE of the first pulse is taken, and the ADC values are added when combining the pulses.
- One could imagine the beginning of a pulse to be nearly flat because its peak is superimposed on the falling slope of a precursor pulse. The leading edge value will be set far below the lower region boundary. In that case, the two pulses are also merged, adding the ADC values together and taking the LE of the first pulse. See Figure 4.5(b) for an example of this situation.

4.1.3 Comparison of the available feature extractors

We have discussed three different feature extractors. Here we highlight the differences between the IcePack feature extracter and both IceTray extractors. The IceTray feature extractors have much in common, and are based on the same algorithms and principles. The subtle differences between the FE and NFE and improvements of the NFE are clearly described by Marius Wallraff [55].

Different methods

A few intrinsic differences are highlighted; firstly, the IceTray FE's use different algorithms for waveforms with different complexity assigned to them. The IceTray FE's divide the ATWD waveforms into two main groups, labeling them as being either "simple" or "complex". The algorithm that is used for this division, is based on a number of thresholds that determine if pulses are too long, too high, or too close together. The IceTray FE's use a fast algorithm that can be run over "simple" waveforms to speed up the extraction process, and uses

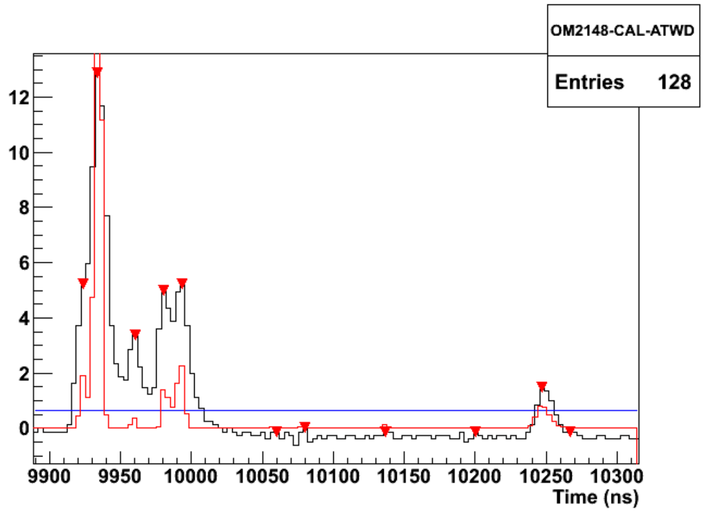

(a)

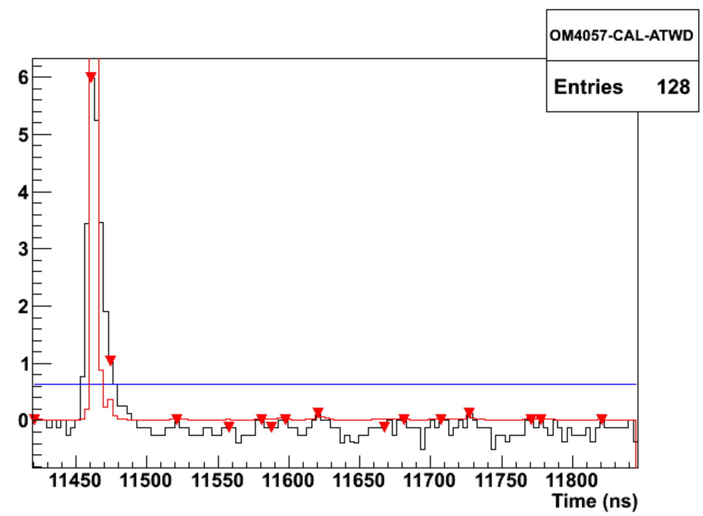

(b)

Figure 4.5: Two ATWD waveforms are drawn from IC40 experimental data. The time with respect to the trigger-time of the event is given on the x-axis, against the charge in mV on the y-axis. The deconvolution spectrum is illustrated in by the red line, using 50 iterations. The algorithm finds all possible peaks, indicated by the red arrows. The threshold for the peaks is indicated by the blue horizontal line, all peaks above the threshold are taken into account for the hit extraction. (a) This waveform illustrates how a bigger pulse is decomposed of several smaller pulses. When the pulses are not clearly separable, they are merged, which is the case for the first two peaks, see section 4.1.2. (b) This waveform illustrated how a subsequent smaller peak lies on the tail of a large peak. Also in this case the hits are merged, see section 4.1.2.

a more elaborate algorithm for the "complex" waveforms. On the other hand, the IcePack FE uses one single algorithm for all the waveforms.

The swiftness of the algorithm is important because the algorithm should be able to handle the large data-set at the South-Pole with small computing power. However, because the feature extractors run with totally different software packages (IceTray vs IcePack), a comparison of their processing speed is not trivial and falls beyond the scope of this research. It should be noted that all feature extractors are optimized to run swiftly. In case of the IcePack FE, it uses only fifty iterations instead of a thousand, which would have somewhat increased the resolution of the peak finder.

A second essential difference is that the IcePackFE does not split bigger pulses into single PE pulses, but sometimes even merges pulses, when there is no clear division possible. The basic philosophy behind this is "only use what you observe". The IceTray FE's use a Bayesian Unfolding algorithm, which determines how a pulse is built up by single PE pulses. The idea behind splitting bigger pulses into single PE pulses, is that the track reconstruction algorithms, like the MPE fit (see section 4.3.2), are optimized to work with single PE hits. The reconstruction algorithms will not take the total charge into account, when reconstructing a track. Ideally, one should feed the reconstruction algorithms with single PE pulses, hence the choice to split the pulses by the IceTray FE's.

There are, however, a few drawbacks to this method. Firstly, the Bayesian Unfolding algorithm splits pulses in theoretical single PE pulses, which are not necessarily the original physical pulses. A study on the shape of the pulses in the different waveforms was done by Chistopher Wendt [63]. But despite of a thorough research on the pulse shapes, for substantial amount of waveforms, the Bayesian Unfolding seems to split the pulses too much, more than once resulting in many unphysical hits that are much smaller than single PE pulses. The question thus remains if the track reconstruction will be improved by using the split pulses from the IceTray FE's, or whether it works better using the more conservative hits from the IcePack FE.

The leading edge determination differs slightly between feature extractors. Where the IcePack FE takes the steepest rise of a pulse, and extrapolates its tangent to the effective baseline of the pulse, the IceTray FE's use the intersection of the fitted single PE pulse with the baseline to determine the leading edge. This results in a slight offset of leading edges between the feature extractors. This offset was also found when using the same FE for hits from the FADC and the ATWD channels, resulting in a 15 ns offset incorporated in the DOM calibrator [55]. This offset was partly due to the use of the IceTray FE. Further investigations are currently being performed to check if the IcePackFE also gives a certain offset, or if this offset is entirely due to the used FE.

Certain thresholds are also set differently in the various feature extractors. These thresholds determine if a hit is recorded or not, and depend on the algorithms. Thresholds are set to eliminate noise, and to speed up the methods by ignoring the small pulses. As will be shown below, the IcePackFE is more sensitive for the smaller pulses. The basic idea for a feature extractor should be to locate every pulse first, before each pulse is subjected to a hit-cleaning process, eliminating all the unphysical small pulses.

Feature Extractor Performances

The data used for a comparison between the three feature extractors, is IC59 experimental data (test-run 113944) and IC59 simulated Monte-Carlo Corsika background events (run 2870.000), consisting of down going muons. During the period in which I performed my research, several low-level checks were performed on this data by the IceCube collaboration, in particular by the IIHE group in Brussels. The ATWD waveforms are comparable to the waveforms of the IC40 data used in this thesis.

First, the performance of the feature extractors is compared by determining the amount of missed hits, using the experimental data. This is done by subtracting the LE values of all first hits found in each waveform. A missed hit by a feature extractor, will result in a big difference in LE values, as the subtracted LE values will not belong to the same hit. Figure 4.6(a) shows that the original FE is missing a substantial amount of first hits compared with the IcePack FE, about 3900 for the total 80500 events (5 %), indicated by the entries on the right of the peak. However, on the left side of the peak (below 0), the two histograms are similar, meaning that there are very few hits missed by IcePack FE that are picked up by the other two IceTray FEs. Figure 4.6(b) shows a large reduction of missed hits by the NFE. For the same amount of entries, the NFE only misses about 500 first hits (0.6 %). A further inspection by eye shows that the majority of missed hits by the IceTray FEs are small hits. This is further acknowledged by Figure 4.8(c), where most of the unfiltered hits of IcePack FE have a very low (< 1 Photon Electron) charge. These very small hits are considered noise hits and will be eliminated by the hit-cleaning procedure (section 4.2). However, it is shown here that the sensitivity of the IcePack FE is better than the sensitivity of the IceTray FE for small hits.

An investigation by eye shows that the majority of the hits that account for a LE difference of $< -10\ ns$, are due to the large offset in LE values for complex large pulses when using different feature extractors.

It is noted that the peak of the histogram lies just below 0, indicating a structural offset in leading edges due to the use of different methods. The total difference is never more than 400 ns, which is the total time-span of the ATWD waveform. The exception is the case where a feature extractor does not find any hit in the waveform. In that case the difference in LE is around 10.000 ns (the typical trigger-time of the detector), falling out of the scope of the histogram.

When comparing the performance of the feature extractors for more complicated waveforms, we have found that the IceTray FE's generate more hits because of the Bayesian Unfolding algorithm. An example of such a waveform is shown in Figure 4.7. Clearly, this waveform will be evaluated as being "complex". The leading edges are indicated by the blue lines, which are scaled to the ADC value of the corresponding pulse. From this figure, we learn that indeed the IceTray FE's measure more hits than the IcePack FE. The NFE is the most compatible with the IcePack FE, but the IcePack FE seems to result in the

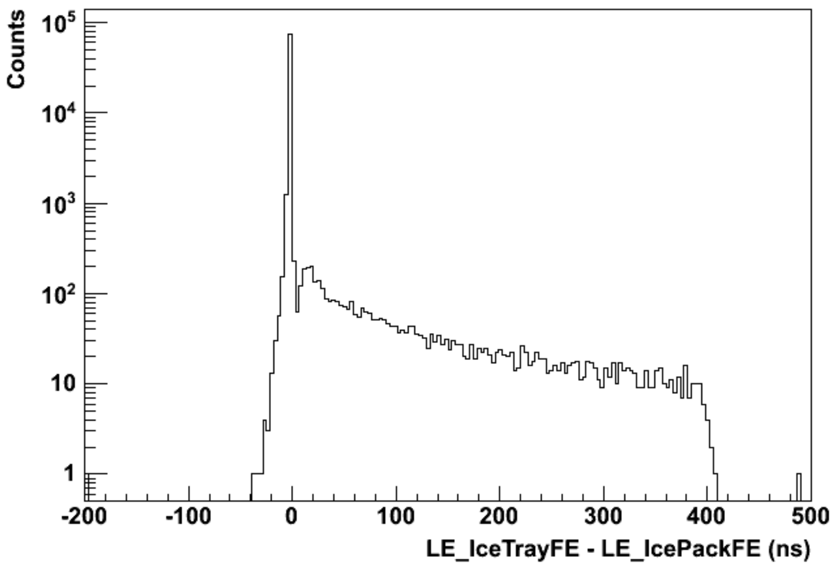

(a)

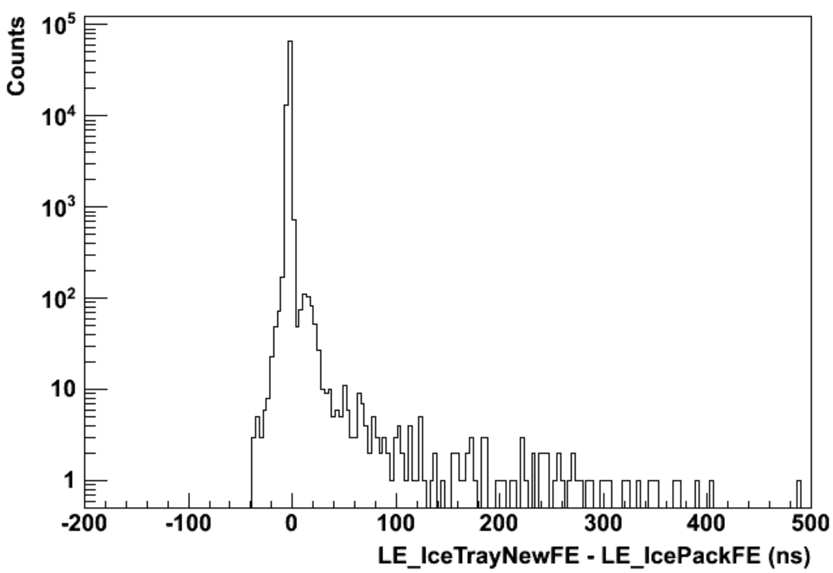

(b)

Figure 4.6: The leading edge of every first hit is compared for IceTray FE's compared to IcePack FE. More detail is found in the text.

most reasonable hits. It will be shown below that this also improves the track reconstruction, see table 4.2.

The charge (ADC) distributions for different feature extractors are illustrated in Figure 4.8. For all three feature extractors the majority of the pulses have a charge of around one photon electron (PE). The IcePack FE shows a small excess of larger pulses compared to the IceTray FEs, and reconstructs small charged pulses well. Pulses with a charge < 0.15 PE are considered noise peaks (visible in Figure 4.8(c)). These pulses are removed by the hit-cleaning procedure, resulting in the distribution of Figure 4.8(d). It is noted that a substantial amount of pulses extracted by the IceTray FE have a charge ~ 0.5 PE. This is caused by the pulse-splitting procedure of the IceTray FE, where large pulses are spit into (too) small pulses with a resulting charge of < 1 PE per pulse.

Figure 4.9 shows no clear difference in the number of extracted hits per event for the different feature extractors, because all feature extractors conclude with a majority of single PE pulses. Therefore, a calibration of the charge for each DOM can be performed by taking the median value of the ADC distribution[4]. Due to the high resolution of the Photo Multipliers of the DOMs, single photons are detected. The emitted Cerenkov light also comprises of single photons, which accounts for the majority of the light in the detector. This amplitude calibration is the subject of the research of a fellow student, working on a similar dataset.

In the end, the feature extractions form the basis for a good track reconstruction. For a performance comparison on that level, the first guess algorithm "Linefit" and the likelihood reconstruction "Pandel" are run over three different hit-samples of the same data, produced by the different feature extractors . For a full description on the track reconstructions, see section 4.3. For now, it is important to know that the $Linefit$ is a quick first guess reconstruction and uses only the first hit detected by a DOM. The *Pandel* reconstruction uses all hits and calculates a likelihood value from the first guess track and the total hit pattern, based on the probability for each hit time to occur under the given track hypothesis. The likelihood value is maximized by an iterative procedure, resulting in an improved track, [64].

The two track reconstructions are run on the same simulation dataset, which is analyzed by either the original IceTray FE, the new IceTray FE or the IcePack FE. Moreover, the reconstructions are performed again, using a hit-cleaning procedure (see section 4.2) to investigate its effect on the three different feature extractors. The performed track reconstructions are compared to the original simulated (Monte Carlo) track, determining the angle between the reconstructed track and the true (Monte Carlo) track. The median of all the angles between the tracks is a good indication of performance and accuracy of the track reconstruction. This is illustrated in Figure 4.10. The median of all angles provides a comparison parameter for the different data-sets, see table 4.2.

Background simulation data (Corsika) of the IC59 detector at filter-level 2 is

[4]The calibration of the charge was already performed for the hits used to derive the ADC distribution of Figure 4.8

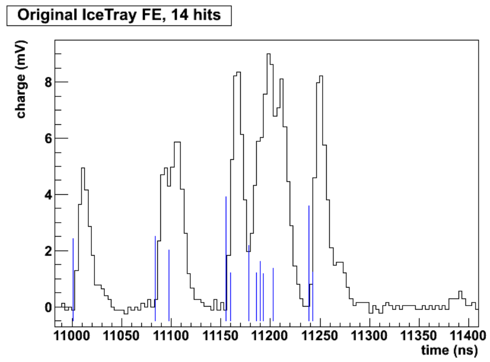

(a)

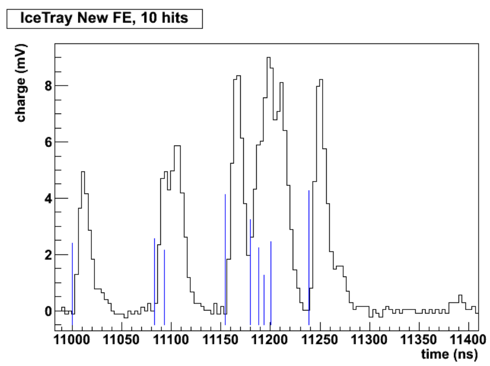

(b)

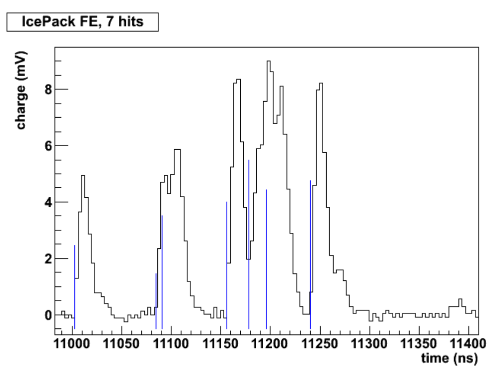

(c)

Figure 4.7: Waveform of the ATWD channel is drawn. The time in ns indicates the time with respect to the trigger-time of the event, and the charge is given in mV. The same waveform is shown, but evaluated by the three different feature extractors, resulting in different hits with different leading edges, indicated by the blue lines. These lines are scaled by the ADC value of the indicated hit.

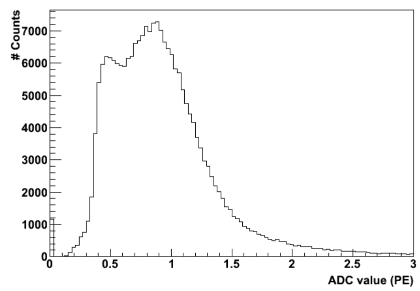

(a) Original FE

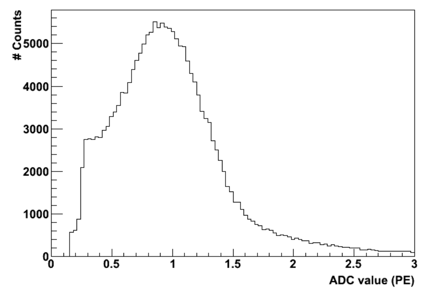

(b) New FE

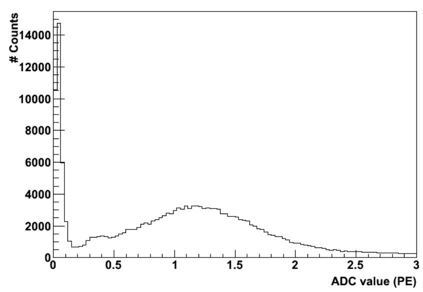

(c) IcePack FE, no hit-cleaning

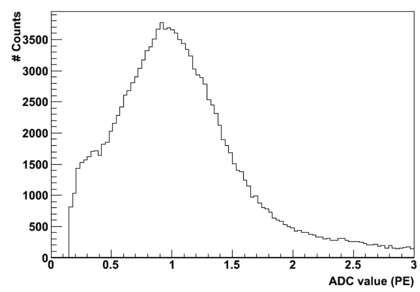

(d) IcePack FE, with hit-cleaning

Figure 4.8: The charge (ADC) distributions of the hits that were produced by the different feature extractors. The IceTray FE's show a clear single PE peak ((a) and (b)), with very few hits having more than 2 PE charge. A substantial amount of hits with $\sim$0.5 PE charge is visible for the IceTray original FE, as well as for the IceTray NFE. This is caused due to (over)splitting of pulses, where larger pulses are split into pulses with a charge < 1 PE. The ADC distribution for the IcePack FE hits ((c) without hit-cleaning and (d) with hit-cleaning procedure performed) shows that the majority of the pulses have a single PE charge, although the number of larger pulses (> 1 PE) are a bit more for the IcePack FE. The noise peak for very low ADC value hits are filtered out by the hit-cleaning procedure, which causes the removal of very low charged pulses that are visible in (c) but not in (d), see section 4.2

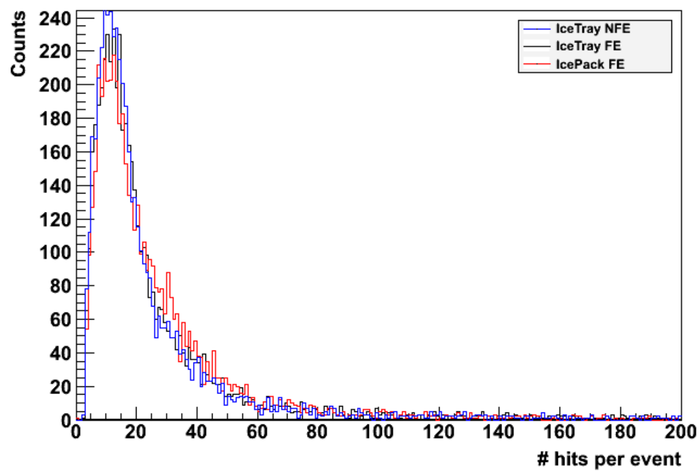

Figure 4.9: The number of hits per event are drawn. No clear difference is seen between different feature extractors, because of the dominating single PE pulses.

used (see section 4.4). The hits of the IceTray FE's have therefore already been subjected to a hit-cleaning procedure, filtering out all the hits with small ADC values. The hit-cleaning performed on this data is only an isolated hit-cleaning procedure, see section 4.2. For the IcePack FE hits, the hit-cleaning procedure also filters out all the hits that have an ADC value of below 0.15 (PE), see Figure 4.8.

From table 4.2 we learn that the performance of Linefit first guess reconstruction is independent of which feature extractor is used. As the Linefit only uses the first hit of every DOM, one would not expect to see a difference in performance using the NFE or the IcePack FE. But even using the original FE, which misses about 5 % of all the first hits, does not influence the resolution

Table 4.2: Comparing the different feature extractors; the median of the distribution of the angles between MC track and reconstructed tracks are given in degrees

Track reconstruction	hit-cleaning	original FE	New FE	IcePack FE
Linefit	off	33.9	33.9	33.9
Linefit	on	26.2	26.2	26.2
Pandel	off	30.4	29.8	30.4
Pandel	on	22.3	22.1	20.4

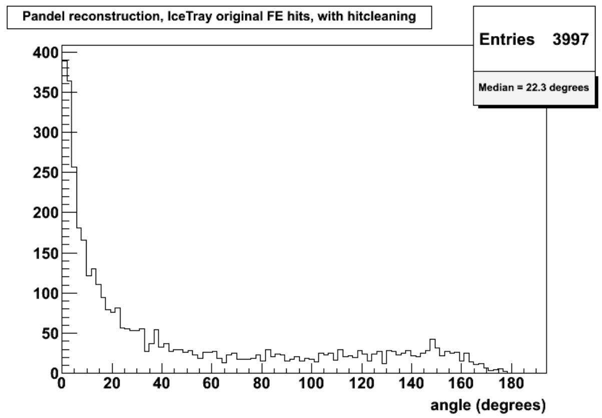

(a)

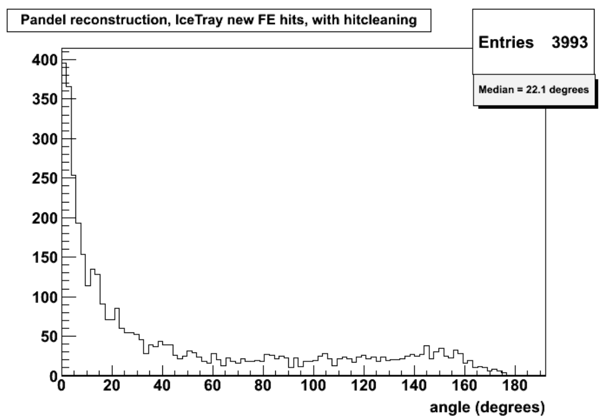

(b)

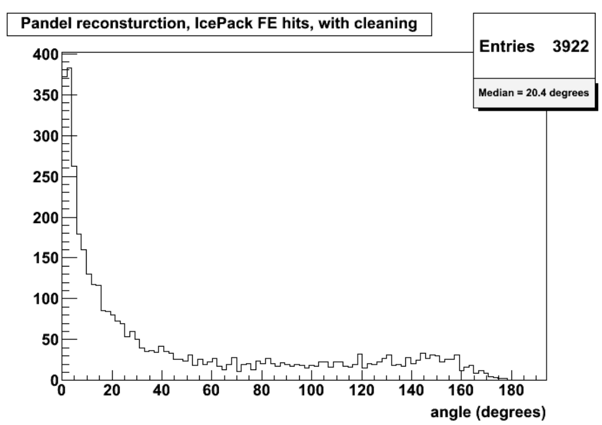

(c)

Figure 4.10: The angle between the Pandel reconstructed track and the original (Monte Carlo) track is plotted. The same data is used, with a different feature extractor. The median of all the angles between the tracks gives a good comparison between the different feature extractors. The Pandel reconstruction performs better with the IcePack FE data.

of the track reconstruction. However, the hit-cleaning procedure influences the performance of the Linefit substantially, similarly for all three feature extractors.

When looking at the Pandel reconstruction, a small difference is visible between the data-sets of the different feature extractors, but the majority of the improvement is again made by using the hit-cleaning procedure. The difference for the Pandel reconstructed tracks with hit-cleaning is illustrated in Figure 4.10. The cleaned IcePack FE hits form the best data-sample for the Pandel reconstruction. One could argue therefore that extracting hits with the IcePack FE (using a basic method to extract hits), improves the data so that a better track reconstruction is possible ($\sim$ 10% lower median for the angle between the MC track and reconstructed track).

4.2 Hit cleaning

After finding all the hits, and before performing a track reconstruction, it is important to remove noise hits, obtaining a cleaner sample of physical hits. Table 4.2 shows a direct improvement of the angular resolution for both track reconstructions by using a hit-cleaning procedure.

In the short duration of an event, the IceCube detector is still contaminated by several types of noise. Electronic noise that is generated by electronics in the DOMs or in the DAQ system cause small pulses. Other noise hits due to photons that are not related to the physical event (muon or other particles in the detector) will cause "normal" pulses, but are usually "isolated hits". These hits have no neighboring DOMs firing at the same time.

The hit-cleaning procedure tries to remove these noise hits, by filtering unphysical hits that do not pass the thresholds for the ADC and TOT values. Also, the isolated hits are removed from the data-sample, by eliminating hits that have no hit from another DOM within a certain radius and time window.

As the data that was used in the track reconstruction comparisons was taken at filter level 2, the original hit-cleaning procedure of IceTray was already performed on the data-sample. The large improvement in the quality of the track reconstructions that resulted from the use of the IcePack hit-cleaning method clearly indicates potential for improvement on the basic hit-cleaning. However, a thorough investigation into a further improvement in hit cleaning falls outside the scope of this Thesis.

4.3 Track reconstruction

The large ($\sim$ 550 Hz) event rate in the IC40 detector needs to be reduced by several filters to a more manageable data volume, before the data can be transferred to the research centers outside Antarctica. The filters use a first-guess track reconstruction for a crude direction cut, which have to be performed "online", at the South-Pole. The first-guess algorithm should be both fast and reliable, making sure no signal events are thrown away besides minimizing CPU time to cope with the event-rate at the South-Pole. After the events are selected, a more thorough and CPU consuming likelihood track reconstruction is performed. Using the first-guess tracks as a seed, these track reconstructions calculate and maximize the likelihood of each hit with respect to the hypothesis track. The likelihood reconstruction can achieve around one-degree accuracy for the IC40 data used for the analysis performed in the presented report, [65].

4.3.1 first-guess track reconstruction

The first-guess methods provide a track that can be used as an initial hypothesis for the likelihood reconstruction. These first-guess methods do not need an initial track, but produce a track with a fast analytical algorithm from the hit information only.

Direct Walk

One effective algorithm used for a first-guess reconstruction is the so-called Direct Walk algorithm [64] [66]. It was developed and used by the predecessor of the IceCube detector, AMANDA [64]. The algorithm uses the geometry of a Cerenkov light cone, taking the first hit of each DOM that passed the hit-cleaning procedure. The method is extended for the IceCube detector, to be able to recognize multiple tracks in one event. This will allow for the reconstruction of muon bundles or other multiple tracks in the detector, but also suppresses background event from double muon events, traveling through the lower and upper detector, otherwise reconstructed as one upward going track [66]. A further improvement was implemented to provide more accurate time residuals, which incorporate the time-jitter that is caused by the resolution of the detector [67].

The procedure starts by connecting hits with a straight line, so-called track elements (TRELs), if they lie at a certain distance and have a certain time difference

$$|\Delta t| < \frac{d}{c} + 30(ns) \begin{cases} with\ d > 75m & for\ AMANDA \\ with\ d > 120m & for\ IceCube \\ with\ d > 50m & for\ DeepCore \end{cases} \tag{4.4}$$

The TRELs have a certain direction, pointing from one DOM to the other. For every TREL, a number of associated hits (N_{AH}) is obtained, by requiring that each hit fulfills both the conditions

$$\begin{aligned} &-30 < \delta t < 300\ ns\ , \\ &d_{hit}/\lambda < F \end{aligned} \tag{4.5}$$

Here δt is the time residual, determined by the time difference of the actual hit time (t_0) and the expected hit time (t_{geo}) if it was a direct hit from our track hypothesis, the TREL. The d_{hit} (in meters) is the distance traveled by the photon, λ is the photon scattering length (in meters) and the default value set for the parameter F is around 3. One advantage of the Direct Walk algorithm is that specific values, as the scattering length in the ice, the minimal distance between DOMs to provide a TREL and the minimal residual time can be set for different detector geometries. This enables a specific optimisation for DeepCore, using separate values for DeepCore and IceCube that improves the track accuracy [68].

Before a TREL is recorded as a Track Candidate (TC), it must fullfill the quality conditions

$$\begin{aligned} n_{associated\ hit} &\geq 1, \\ q_{trel} &\geq 0.8 \cdot q_{trel\ max} \end{aligned} \tag{4.6}$$

where $n_{associated\ hit}$ are the associated hits for a TREL. A quality value q_{trel} is allocated for each TREL, which needs to be at least 80 % of the maximum quality value $q_{trel\ maximum}$ found for all the TRELs in the event.

To obtain the q_{trel}, all the associated hits are projected straight on the TREL. In principle, for a good track reconstruction of a muon track by the TREL, a uniform distribution of the projected hits is expected. However, in the case where the projected hits lie on opposite sides of, or are clustered somewhere along the TREL, it is not probable that the TREL gives a good approach for the original muon track, as it will probably be influenced by isolated hits that have nothing to do with the original muon. The spread of the projected hit distribution is used to determine the quality value (a large spread indicates a uniform distribution yielding a high q_{trel}), as well as the span of the projected hits, which is determined by the distance between the furthest projected hits and the TREL (a large span yields a low quality parameter). The specific equation for the quality parameter is provided in [66].

Finally, the selected TRELs form the Track Candidates,TCs. These TCs are clustered into one track if the directions between the TCs are not more than 15° apart, and lie within a maximum distance (set to 20 meters) of the final clustered track. Therefore, the method is capable of reconstructing multiple (muon) tracks in one event. This is very useful as the so-called "double-muon" events occur regularly in a kilometer-scale detector, and form a large contribution to the up-going background events due to mis-construction of the two tracks in one event (see Figure 4.14).

Linefit

The Linefit first-guess algorithm is based on a χ^2 minimization procedure [69] [64]. The Linefit always produces one initial track based on the hit-times of every first hit in a DOM, with an additional option of weighting the hits using their ADC value. In contrast with the Direct Walk algorithm, the Linefit does not take the geometry of the Cerenkov cone into account, and has no option of using the ice-properties as an optimizing parameter. It simply assumes that the light travels along a straight line with velocity v. For the larger IceCube detector (compared to AMANDA), the Linefit procedure is faster than the Direct Walk, and therefore was used as the "online" first-guess reconstruction at the South-Pole for the IC40 detector.

The algorithm fits the free parameters, vertex position (r) and velocity (v), of a hypothetical straight track to the one-dimensional projection of an observed pattern of hits [64]. The χ^2 is minimized by differentiation with respect to these free parameters, given by

$$r_i \approx r + v \cdot t_i, \tag{4.7}$$

$$\chi^2 \equiv \sum_{i=1}^{N_{hit}} (r_i - r - v \cdot t_i)^2, \tag{4.8}$$

where N_{hit} is the number of hits in the event, v and r are respectively the velocity of the track and the distance to the hypothesis track, r_i is the location of each DOM and t_i is the time of the hit. The minimization can be solved analytically by

$$\begin{aligned} r &= < r_i > - v \cdot t_i, \ and \\ v &= \frac{< r_i \cdot t_i > - < r_i > \cdot < t_i >}{< t_i^2 > - < t_i >^2} \end{aligned} \tag{4.9}$$

Here $< x_i > \equiv \frac{1}{N_{hit}} \sum_i^{N_{hit}} x_i$ denotes the mean of the parameter x with respect to all hits. The algorithm produces a track with a vertex point r and a direction given by the velocity vector v.

4.3.2 Log-Likelihood reconstruction

Further improvement of the track reconstructions is obtained by a likelihood method, taking the first-guess tracks as a seed, or a first hypothesis. The basic idea of the likelihood reconstruction algorithms is to find a track with certain set of parameters {a}, which corresponds to the most probable track for the measured hits in our event {x}. Thus optimizing the function

$$\mathcal{L}(x|a) = \Pi_i p(x_i|a) \tag{4.10}$$

where $p(x_i|a)$ is the probability of observing the measured values x_i for given different parameters {a} [70]. Suppose that r_0 is an arbitrary begin point on the track. At time t_0 the muon passes r_0 with energy E_0 and direction $\hat{p}$, see Figure 4.11. The Cerenkov light is emitted at a fixed angle of θ_c relative to $\hat{p}$.

From all the measured parameters (LE, TOT, ADC and from that the computed energy loss of the muon), the timing (LE) is the most accurate measured parameter. Therefore the Pandel function only determines how probable a certain hypothesis track is when a photon is detected at time t_i in DOM i. The Pandel function, which takes the absorption and scattering lengths of a photon in the ice into account, takes the form of a $gammafunction$ [71] [64]. The Pandel function has some convenient properties, as it is normalized, easy to compute and it is able to use multiple hits from one DOM. However, it has the disadvantage that it cannot handle negative (expectation) times, which may result from a time-jitter in the electronics of IceCube. A convolution of the Pandel gamma function and a Gaussian, which accounts for the finite time resolution of the detector, is used to incorporate the time-jitter in the electronic read-out elements of the detector [67].

MPE-fit

The best likelihood function available for the IC40 data within the IceTray framework, is the so-called Multi Photo Electron (MPE) fit [65], and is used in this analysis as our final track. The method is based on the Pandel reconstruction algorithm, and is a follow-up of the Single Photo Electron (SPE) fit. The difference with the SPE fit is, that the MPE fit uses the time of the first hit of the DOM, as well as the charge of the hit to minimize its likelihood. Two "quality" parameters are determined for each reconstructed track.

The *reduced log−likelihood* (*rlogl*) is equal to the (minimized) log-likelihood value of the fit divided by the degrees of freedom of the fit. The degrees of freedom of a fit is determined by to the number of associated DOMs (N_{DOMs}, the number of DOMs used for reconstructing the track) subtracted by the number of free parameters of the track (five in total, namely θ, ϕ, x, y and z forming the vertex of the track). One needs to divide the log-likelihood by the number of degrees of freedom in order to put all events on equal footing. The likelihood value for a fit with a low number of associated DOMs is much smaller than for a fit with a large number of associated DOMs. By dividing by the degrees of freedom, the events can be compared equally with the *rlogl* value.

The uncertainty of the fitted track is also determined and expressed as the Paraboloid error (see section 4.3.2). These quality parameters have a well defined *probability distribution function* (pdf) for signal and background events, which allows us to eliminate the background events from our sample by applying cuts on these parameters. Along with the most accurate fit possible, this should provide a stable basis to suppress a substantial amount of background without loosing a lot of signal events, see section 4.6.1

A comparison between the performance of the MPE-fit, the first-guess Linefit and the Pandel reconstruction is shown in Figure 4.12.

Paraboloid error

Although the MPE-fit does a good job at finding the direction of the original track (see Figure 4.12), it is useful to get an idea of the resolution of each track separately, without having the information of the original muon track. Therefore, a method to calculate the angular resolution of the track is derived. Within a 10 degree cone around the direction of the track, the Log-Likelihood function is fitted through a grid search. This results in a 2D Gaussian variance of the fit, where the combined width of the Gaussian gives a good estimate of the tracks resolution by

$$\sigma \equiv \sqrt{\frac{\sigma_\theta^2 + \sigma_\psi^2}{2}} \tag{4.11}$$

For a full detailed mathematical overview of this approach, see [72]

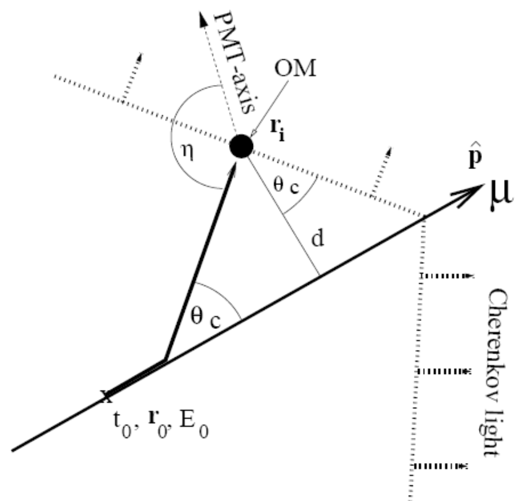

Figure 4.11: The muon track is illustrated with the Cerenkov light front. The definition of the variables can be found in the text [64]

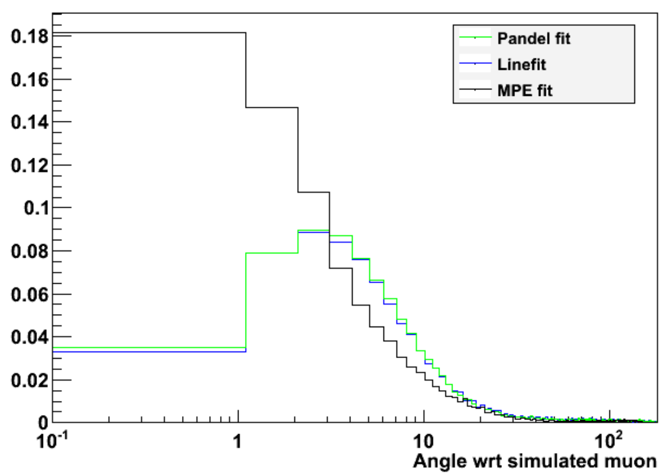

Figure 4.12: The angle between the reconstructed track and the simulated Monte Carlo track is normalized and illustrated in this figure. The difference in resolution is visible for the first-guess track reconstruction Linefit, the Pandel reconstruction using the Linefit as a seed, and the MPE reconstruction.

MuE energy reconstruction

The muon passing through the detector will loose energy as it emits Cerenkov light, which allows us to make an estimate on the energy of the muon. Because the path of the muon extends beyond the detector volume, the estimated energy loss will always be an underestimation of the reality. To keep our analysis as model independent as possible, the estimated energy of the muon is only used to scale the paraboloid error, see section 4.6.1.

A simple but inaccurate way to determine the (relative) energy produced by a muon in an event, is by counting the total number of DOMs that recorded a hit, N_{DOMs}. To define the energy of the event, the number is multiplied with a conversion factor, although usually just the number DOMs with a hit are compared for each event. This value is sometimes optimized by taking the total charge of every DOM that recorded a hit, but it will never be an accurate determination as it does not take the scattering or light absorption into account, which is different for each part in our detector.

A more sophisticated way of determining the energy of the original muon, is done by the MPE mueEn package, which estimates the energy loss per track length. The scattering and absorption of each part in the detector is used by this procedure, leading to a much more accurate energy determination. This energy estimation is done after the MPE-fit is determined, and is used in this analysis to scale the paraboloid error with the energy.

4.4 Data Filtering

Approximately one in about five million triggered events in IceCube is an astrophysical interesting neutrino signal event. The trigger rate in the detector is about 550 Hz, making rigorous filtering and cleaning of the events and hits a main task in every step towards a discovery. The GRB analysis described in this report was performed on data from the IceCube detector in its 40 string configuration. This data was processed to the so-called $filter - level$ 2, where all the needed filtering, hit-cleaning, first-guess and log-likelihood track reconstructions were performed and are readily at hand. In this section an overview is provided on the data filtering process [73]. Further filtering of the data specifically done for this analysis will be described in section 4.6.

Level 1 and Online Muon Filtering

The first filter level is obtained "online", at the South-Pole. Only the events that pass this filter are transferred for further analyses to other research centers outside the Antarctic. After an event has been triggered (see section 3.3), all hits in a surrounding time window of 6 μs are recorded. The first cleaning is done directly, storing only the hits that have one of their four neighboring DOMs firing as well, within 1 μs. Directly after the event has been stored, the Linefit first-guess algorithm determines a possible track. There are several filters that all use the first-guess track to flag their desired event sample. The events in

Table 4.3: Summary of filtering procedure for IC40 data

Filter Level	Process / Selection
Level 1	$\theta_{Linefit} \geq 90°$
	$\theta_{Linefit} \geq 70°$ for $N_{hits} \geq 10$
	$\theta_{Linefit} \geq 60°$ for $N_{hits} \geq 40$
	$\theta_{Linefit} \geq 50°$ for $N_{hits} \geq 50$
Level 2	Log-Likelihood reconstruction
	$\theta_{Log-Likelihood} \geq 80°$
	rlogl and Paraboloid error calculation

this analysis are filtered by the $Muon\ Filter$, which focuses on muon-track like events. The easiest way to reject the bulk cosmic ray muons would be to select exclusively up-going tracks. However, for neutrinos in the PeV and EeV region, the earth becomes opaque. These high-energy neutrinos will only show up in the direction close to (including just above) the horizon, making it worthwhile to combine specific declination cuts with certain energy criteria. The muons from high-energy neutrinos will still stand out from the cosmic ray background muons because of their much higher energy, unless the neutrino interacts far away from the detector, whereas the incident muon will loose a great deal of its energy before arriving at the detector. A quick estimator used to determine the energy of the muon (that provides an indication of the original neutrino energy) is the number of DOMs that have registered a hit, N_{DOMs}. The Muon Filter therefore accept down-going tracks, provided that the N_{DOMs} is large enough, as summarized in table 4.3.

Level 2 Filtering

The second filter level (level2) is performed "offline". A thorough and time consuming log-likelihood reconstruction, energy and Paraboloid error calculation is carried out on the level-1 filtered data that is transported from the Pole. The determinations of the energy and the Paraboloid error are only executed if the likelihood track has a zenith angle $\geq 80°$, saving CPU time. It is not possible to perform a MPE-fit on all events, which also is the case for the calculation of the Paraboloid error. This decreases the data-sample because the analysis only takes MPE-fit tracks into account for which a Paraboloid error has been computed. Table 4.3 summarizes the thresholds of the filtering processes that were performed before the data was analyzed for this report.

4.5 Simulation

To get a proper understanding of our real experimental data, and to be able to optimize our dataset and track reconstructions, simulated data is needed.

Namely, the simulated events contain all the original parameters of the muon, and thus enable us to compare for example the reconstructed direction, rlogl and Paraboloid error of the experimental data with the corresponding values of the simulated Monte Carlo muon-tracks. By comparing the signals in the detector for "upgoing" mis-constructed background events and signal events, appropriate cuts on different parameter values can be determined, such that a substantial amount of mis-constructed background events can be removed without loosing too much of our signal events.

A large number of simulated events is needed to compare with the vast amount of experimental data. Because the interesting events are mainly high-energy events, and because the majority of the background events from cosmic rays are at lower energy, the generators will normally not generate particles in realistic proportions. As such, a larger number of high-energy events is simulated in order to increase their statistics, which are then scaled back to make a realistic comparison with real experimental data using a weighting function.

For the cosmic ray muon background events, the simulation package $Corsika$ [74] is used. Because the IceCube detector has a big volume, and the cosmic ray rate is quite high, roughly three percent of the events have two muons that pass through the detector in the same 6 μs trigger time window, so-called $double - Corsika$ events. These events are generated separately. The double and single Corsika data can be combined using their correct weights.

The signal neutrinos from the GRBs are generated by the $NuGen$ package (a successor of the $Anis$ package [75]). The energy spectrum of these signal neutrinos follow a E^{-2} spectrum, which is comparable to an average GRB spectrum. An in-depth comparison of this energy spectrum compared to the Waxman-Bahcall shaped GRB spectrum was performed by Martijn Duvoort [24]. Between the different simulations, no substantial difference is seen for the *pdf* of different detector parameters, such as the number of DOMs, number of hits per event, the paraboloid error and rlogl, which enables us to use the generic E^{-2} spectrum in the analysis.

After simulating the interactions that produce a muon, it is propagated through the ice and rock, by simulation of the Muon Monte Carlo (MMC) [77]. The propagation of the photons from the muons that pass through the ice, are simulated with the software toolkit $Photonics$ [78]. This step in the simulation is a crucial one, as the ice properties are the most uncertain parameters in the whole simulation. From all kinds of particle physics experiments the energy loss, decay and cross-sections of the simulated particles have been carefully measured [79]. However, the ice-properties of the ice is not a trivial task to determine. Certain $flasher\ runs$[5] and other calibration methods[6], have been

[5] A flasher run is a specific data-set that is obtained by using light emitting modules (flashers) of several DOMs that emit light in the detector. The amount of detected light by the other DOMs is used to determine the light propagation and scattering in the ice.

[6] Other methods that determine the light properties in specific regions of the detector, are obtained by investigating experimental data. The amount of detected light per DOM is determined, for instance by investigating how much light is detected by a DOM that lies close to a reconstructed track.

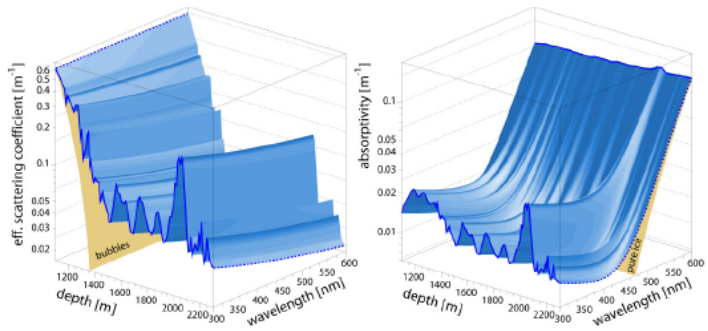

Figure 4.13: Maps of the scattering and absorption coefficients of the ice in the IceCube detector, as a function of wavelength and depth. The absorption and scattering heavily depend on the amount of dust in the ice. Moreover, the scattering also depends on the amount of air bubbles in the ice. [76]

performed, producing a map for the scattering and absorption coefficients of the ice, illustrated in Figure 4.13. This map of the ice properties is used by the simulation module that simulates the propagation of the photons through the ice in the detector.

Finally, the detector response to the photons arriving at the DOMs is simulated by the module $DOMSimulator$, [80]. Here the knowledge of the geometry and the location of each DOM are taken into account. Further more, random noise in the DOMs is generated to produce the most realistic data-sample possible.

4.6 Optimizing the data-sample

The data-sample after the level 2 filtering procedure is still contaminated by a vast amount of mis-constructed cosmic ray muon tracks, which misleadingly seem to come from to the Northern Sky. This is illustrated by Figure 4.14, showing background Corsika simulated data. The original muons all have a zenith angle of $> 90°$, traveling downwards in our detector. But numerous reconstructed MPE-fits have a direction upwards in our detector, with a zenith angle of $< 90°$. Most of these events are due to the double muon events, where two muons pass through the detector at the same time, see section 4.5.

Fortunately, the quality parameters (paraboloid error and rlogl) of these mis-constructed tracks have a different *pdf* than for the signal events. The experimental data, which consist predominantly of cosmic ray muons, is compared to simulated signal neutrino events to determine the best cut values to dissociate the signal and background events. For the GRB analysis described later-on, the cuts are optimized such that the best signal over background ratio is achieved. Cuts on the $rlogl$, the $paraboloid - error$ and the $opening - angle$

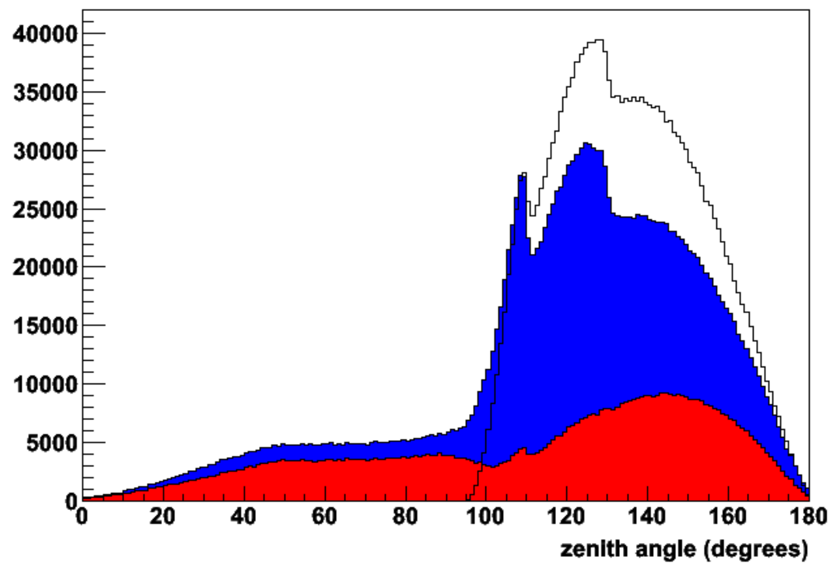

Figure 4.14: Zenith angle distribution for all events passing the Muon Filter. The black (thicker) line illustrates the distribution of all the original Monte Carlo muon tracks. The red filled curve illustrates the distribution of double Corsika event tracks, and the stacked blue curve illustrates the distribution of all single Corsika event tracks. The figure shows that some muon particles traveling down-wards through the detector, are misconstrued as up-going tracks and thus slip through the Muon Filter. The loosened zenith angular cuts for events with higher N_{hits} is also visible from the bumps in the histogram for higher zenith angles. Furthermore, the (almost) linear rise of the event-rate from 0° to 40° is due to the area increase of the declination band for lower zenith angles.

of the track with respect to the GRB are used in this analysis. Because a generic E^{-2} spectrum is used for our signal neutrino data-sample, the cut values for the parameters are an approximation for the best average cut values for the GRBs in our sample.

Quality checks on simulated data

To determine the quality of the simulation data for the detector, a comparison between the experimental data and the simulated background events will be made. This is done to show that the simulations are done correctly and we are able to understand our detector, before using the simulated signal data to make rigorous cuts to reduce the background. The simulated background data consist of double and single background muons, and muons originating from atmospheric neutrinos. The different simulated background datasets need to be combined with their specific weight, so that it will give a realistic representation for the events in IceCube.

Figure 4.15 illustrates the comparison of the simulation and experimental background data[7]. The number of hits and number of DOMs per event are in good agreement, between the experimental data and simulated background data. Both the rlogl and the paraboloid error (sigma) of the MPE-fit track reconstruction compare well. A (small) difference can be seen for the events with a higher amount of hits, the higher energy events. The simulation data for higher energy events show a lower amount of hits and DOMs per event compared to the experimental data. The difference could occur because the lower part of the detector is not yet simulated accurately enough. The ice in the lower part of the detector seems to be clearer than expected, but further research is ongoing on this subject. It should be clear that the ice-properties dominantly contribute to the uncertainty in the simulations. These checks show that the simulation data is a good representation of the real data, and it is therefore legitimate to use the simulated signal data-samples to optimize our final dataset.

4.6.1 Defining the cut parameters

For our data-optimizing procedure we use three parameters of the MPE reconstructed tracks, namely the $rlogl$, $paraboloid - error$ and $opening - angle$. The distributions of these parameters are illustrated in Figure 4.17. A clear difference can be observed between the distributions of these parameters for signal and background events. This will enable a background elimination procedure. It is noted that the shapes of the distributions will change when stringent cuts are applied, because the parameters are correlated with each other. As such, we will use an so-called GRID search to find the best cut values, see section 4.6.2. In this section we will describe how the parameters are defined for our experimental background and simulated signal data-samples.

[7]For the single and double muon background data, respectively Corsika data-sets 2712 and 2483 are used [81] [82]. The data-runs taken for the experimental background data are described in section 4.6.1

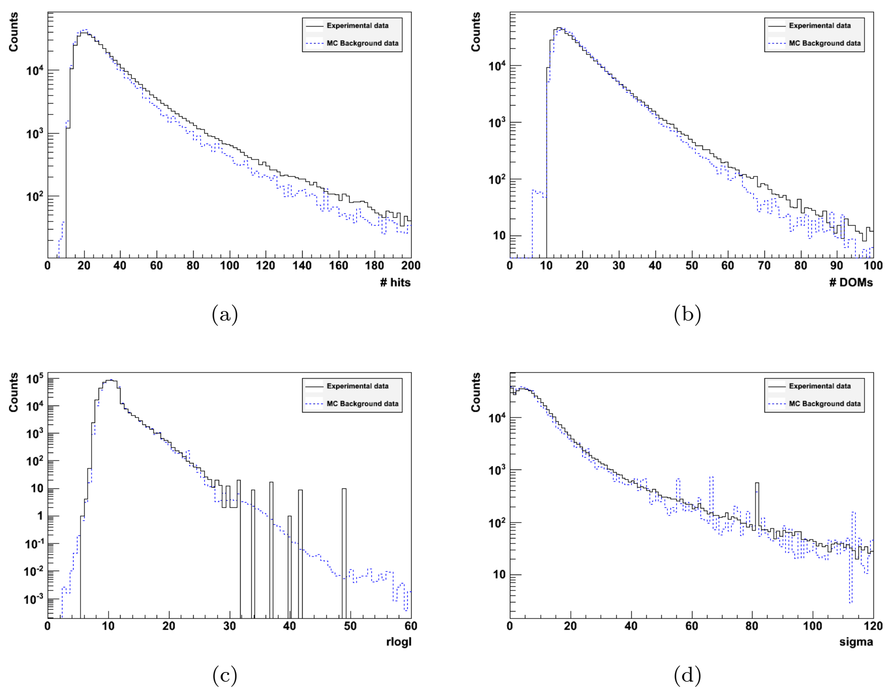

Figure 4.15: The simulated background data compares well with the experimental test data. For higher energy events (i.e. events with a large number of hits and DOMs per event) the simulation data shows a lower amount of hits and DOMs per event than the experimental data. This is possibly due to the very clear ice in the lowest part of the detector, which is difficult to simulate accurately. Further details are given in the text.

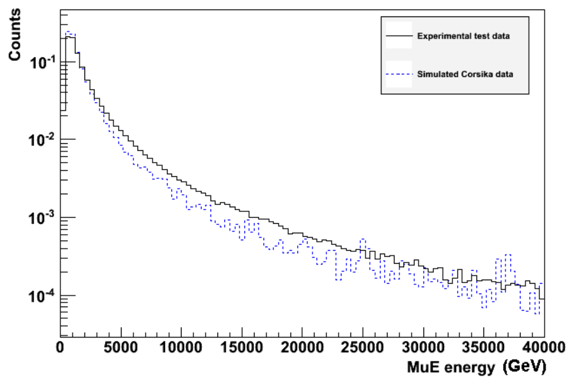

Figure 4.16: The estimated MuE energy is consistent between simulated and experimental data, apart from small deviations visible at higher energies due to the imperfect description of the ice model.

Paraboloid error scaling with the energy

The paraboloid error is determined by fitting a likelihood space around the final track reconstruction, and is determined by the combination of the standard deviation in both azimuthal and zenith direction, following equation 4.11. It is an important parameter, as it provides the standard deviation of the error for the track reconstruction on an event-by-event basis, without using information of the angle between the Monte Carlo muon track and the reconstructed track. Thus, a specific error for each reconstructed track can be determined for the experimental data.

However, it was found that the paraboloid error needs to be scaled with the energy of the event, to ensure a realistic estimation on the angle between the track reconstruction and the muon track (the 'real' reconstruction error) [83] [84]. For higher energy events, the paraboloid error gives an underestimation on the angle between the reconstructed track and the muon track. In other words, for higher energy events the resolution of the track reconstruction is larger than is indicated by the paraboloid error. Therefore, the paraboloid error should be increased for higher energies. The reasons for this effect is still under investigation and could be due to the imperfect description of the ice model.

The energy determination for this method was done by the MPE MuE energy reconstruction, as outlined in section 4.3.2. Both the paraboloid error of the simulated data and experimental data are scaled by this energy estimation. A consistency check of the energy estimation for simulated background data and experimental background data has been performed, see Figure 4.16. Also here, the energy estimations differ a bit for higher energy events, most probably due to the fact that the simulation underestimates the amount of detected light in the lower parts of the detector. Overall the energy estimation is stable and can be used for the paraboloid error scaling.

Experimental background and simulation data for parameter cuts

For the experimental (background) dataset, three runs on the 8th of March 2009 are used[8]. At the time these data-runs were taken, no GRB was detected, and thus the experimental dataset is "off-time" and "off-source". Therefore, the events can be considered as pure background events for this analysis. It is important to have separate datasets for only signal and only background events, because a possible existence of signal events in the experimental (background) dataset could influence the final tuning of the parameter cuts, as the signal over background ratio will increase when making the cuts.

Due to the asymmetry of the IC40 detector geometry, and because of seasonal variations in the total background event-rate, the background event-rates fluctuate for the different GRBs. This effect is explained in more detail in section 6.1.2, although it also needs to be addressed here, because the simulation and experimental data-sets used to determine the parameter cut values need to be a good representation of the final experimental GRB data-set.

Regarding the total background event-rate, a seasonal fluctuation is observed, illustrated in Figure 6.3. This yields a different overall background event-rate for every GRB data-set taken throughout the year. This seasonal variation is averaged by taking three data-runs that have an average total background event-rate[9].

Also, a fluctuation for the azimuth and zenith angular distribution of the reconstructed tracks is observed. This effect can be explained by the asymmetric geometry of the IC40 detector, which has a boomerang-shaped detector array, illustrated by Figure 3.5. Clear azimuthal preference angles for the track reconstruction can be observed, illustrated in Figure 6.4(b). The probability for a track to be reconstructed by the MPE fit is larger for specific azimuth angles. This yields a larger background rate for specific regions of the sky, but also effects the probability of a signal event to be reconstructed. Due to the Earth's rotation, the detector turns 360° in one day with respect to the fixed GRB positions on the sky. The background rate (and probability of a good reconstruction for a signal neutrino) will oscillate during 24 hours for every fixed GRBs position in the sky. However, only two hours of data are taken around every GRB, so the specific background rate for each GRB depends strongly on the time and position of the GRB with respect to the detector geometry, see Figure 6.5. Unfortunately this effect could not be incorporated in the experimental background and simulation data-sets, as it would have decreased the amount of entries too much[10], which are used for the procedure to determine the best cut

[8]Specifically run 00113177, 00113178 and 00113179 are used for the experimental background data.

[9]This explains the choice of the particular day in the year, 8th of March 2009.

[10]When incorporating this effect, we restrict our data-sample to include events with a track pointing to specific points within a specific time, corresponding to the GRB trigger times and

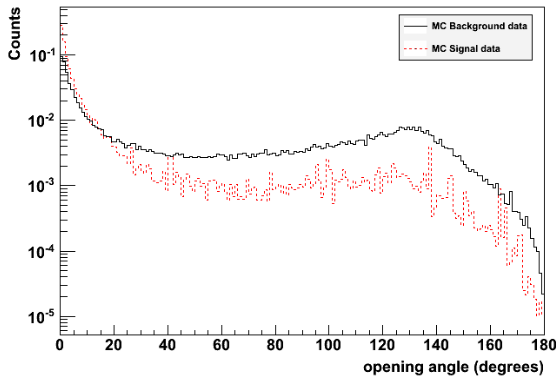

(a)

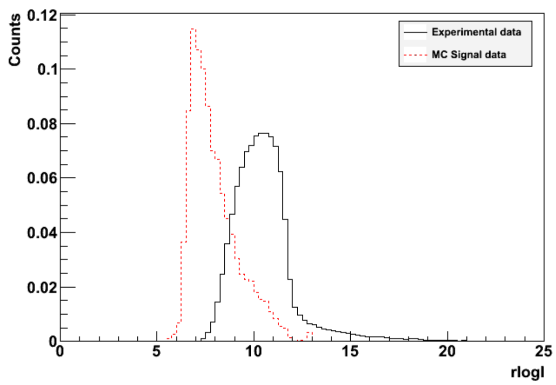

(b)

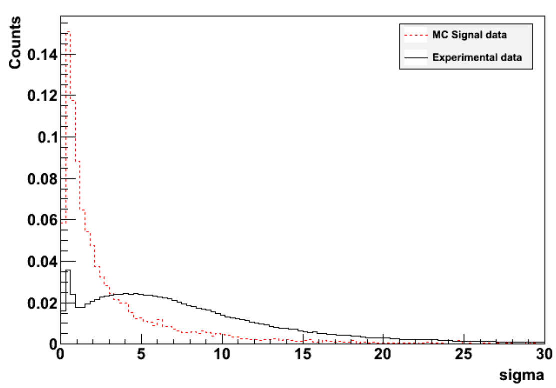

(c)

Figure 4.17: A clear difference is visible in the distribution of the three parameters between the simulated signal data and the experimental background data.

values. Therefore, the azimuthal fluctuation is not taken into account here.

However, the variation in the declination angles of the background tracks is incorporated in this method. The background event-rate varies between different declination bands, but is constant over a large period (>> one day) for every declination band. To incorporate this variation, the fixed GRB positions are used. For the simulated data, all the simulated signal neutrino tracks that point within 10° of the closest GRB position are used, and for the experimental background data (taken during one day), the angle between the reconstructed tracks and the closest GRB position is used in the optimizing procedure. Thus, for every GRB a declination band is used, which incorporates the variance in event-rates for different declination bands.

Opening angle determination

To reduce background events, an opening angle around the position of the GRB is taken. All events with an MPE track that fall outside this opening angle around each GRB position are removed in our real experimental data-set. As such, the optimum opening angle needs to be defined.

For our signal events, the angle between the simulated neutrino track and the reconstructed MPE-fit is determined. As mentioned above, only simulated signal tracks within an opening angle of 10° of the GRB position are used. The GRB position itself is not used to define the angles of the reconstructed particles because the neutrinos are not simulated to come from the GRBs. Note that by taking the direction of the simulated neutrino and not its induced simulated muon, the scattering direction of $\nu_\mu \to \mu$ is automatically taken into account. All the reconstructed MPE tracks that lie within the opening angle around the simulated neutrino track will be used to determine the optimum opening angle.

To determine how many background events pass the opening angle cut, the opening angle is taken around every GRB position. The GRB positions are taken from every GRB used in the analysis (see section 6.2), but are only a reference point in the sky as the experimental data is taken "off time" (no real GRB has been measured during that day). Each experimental background event with a reconstructed MPE track that points within the opening angle of the closest GRB position, is used to determine the cut value.

Thus, while tightening the opening angle, the area around the GRB positions will decrease such that an increasing number of background events will be filtered out as they do not point in a direction sufficiently close to a GRB position. At the same time however, also signal events with an inaccurate MPE-fit that do not point in the same direction as the original simulated neutrino, will be dropped. So an optimum has to be found.

---

positions with respect to the detector. This would decrease our data-sample substantially, leaving us with not enough events to perform the procedure to determine the optimizing cut values.

4.6.2 Optimization procedures

Eliminating as much background as possible, without cutting away too much signal, is our main goal in this procedure. The determination of the best cut values depends on the chosen method of evaluation. For each method, an iterative procedure has to be followed. Each cut on a parameter will change the distribution of the other parameters, as they are highly correlated. For instance, when the angle of a reconstructed track with respect to the GRB position is very large, the signal track will not point back directly to the GRB position, and its quality parameters like rlogl and the paraboloid error are bound to be worse than for an accurately reconstructed muon track. The best cut values are therefore found by using a grid search, changing one cut value at a time, calculating the signal over background ratio for every step. In this section, different algorithms are presented to calculate the signal over background ratio, finally choosing one set of cuts for our analysis.

Hard cut method

A method to make a comparison for each set of cuts, is to find the highest $\frac{\mu_{signal}}{\sqrt{\mu_{background}}}$ ratio. Here μ_{signal} and $\mu_{background}$ are the normalized number of the signal and background events respectively after the cut values have been applied. Unfortunately, this method tends to eliminate all background events, because of the asymptotic behavior for low background fractions, due to the $\frac{1}{\sqrt{\mu_{background}}}$ factor.

Soft cut method

A second method that can be used to find the best cut values, is by determining the highest value of the $\mu_{signal}(1 - \mu_{background})$ factor. Where again μ_{signal} and $\mu_{background}$ are the normalized numbers of signal and background events. This method does not tend to cut away all the background events, and will be compared to the Model Discovery Potential method presented below.

Model Discovery Potential

The Model Discovery Potential method (MDP) [85] was used in a number of other analyses on astrophysical point source studies [24] [86]. The method is optimized to enhance the discovery potential of an analysis, determining the best ratio of background and signal events. This is a slightly different approach compared to the other methods explained above, because the other methods only focus on optimizing the signal over background ratio. The MDP however, uses a calculation of the least amount of signal needed to make a discovery, when the final sample has a certain amount of background entries. With the value of the *least detectable signal* (lds) given some amount of background, compared to the amount of signal in the final sample, the best cuts are determined.

Since our background arises from cosmic ray events that hit the atmosphere at a steady rate, our background is described by a Poisson distribution.

To claim a discovery, a final data-sample has to show a significant enough deviation from a known background distribution. This deviation will count as a discovery when its probability value (P-value)

$$P(\geq n_{obs}|\mu_b) < 5.73 \times 10^{-7} \tag{4.12}$$

In short, the probability (P-value) of an observation of at least n_{obs} events due to (Poissonian) background distribution with a mean value μ_b, has to be smaller than 5.73×10^{-7}, which correspond to the area under the tails of a Gaussian distribution beyond five standard deviations. The MDP method aims at finding a data-set that has the lowest $P - value$, thus optimizing the data in favor of a discovery. The method is not limited to using integer values for the number of signal or background entries, and thus the normalized numbers of signal and background events can be used.

The minimal number of observed events needed for a 5σ discovery, $n_{crit}(= n_{obs})$, is determined by the number of background events. For each set of parameter cuts, this number is known, because a separate background data-sample is used. When applying a certain cut, one is left with a certain fraction of the background. Corresponding to this fraction, the minimal number of signal events (n_{crit}) is determined to claim the discovery.

With n_{crit}, it is now important to know how many events in the final sample are needed to produce this n_{crit} with a certain predefined probability, for instance 90%. The probability that one finds the number of critical events (n_{crit}) in 90% of the cases, is determined by $P(\geq n_{crit}|\mu_X) > 90\%$, where μ_X indicates the number of events in the final data-sample. The final data-sample consists of both background and signal. Therefore, $\mu_X = \mu_{background} + \mu_{signal}$. The background has been fixed by the specific cut value, so we find a so-called *least detectable signal*, $\mu_{lds} = \mu_X - \mu_{background}$ to find n_{crit} with a 90% probability.

Note that this *least detectable signal* is only determined by the $\mu_{background}$ and the predefined significance. Nothing has been done with the specific μ_{signal}, which, like our $\mu_{background}$, is found by applying the specific cuts on the signal data-set. Finally, the ratio of the μ_{lds} and μ_{signal} result in the desired MDP. The method will conclude with the parameter cuts that will give a minimum for the so-called Model Discovery Factor (MDF);

$$min\left(MDF = \frac{\mu_{lds}}{\mu_s}\right) \tag{4.13}$$

Taking the example in [85], imagine that after selecting some cuts, one is left with a Poisson background with $\mu_b = 3.0$, and the amount of signal entries are $\mu_s = 10.0$. The number of observed events, for which a discovery will be claimed, is $n_{crit} = 16$, as $P(\geq 16|3.0) = 1.27 \times 10^{-7} < 5.73 \times 10^{-7}$. If one needs to observe at least n_{crit} amount of entries in 90% of all cases, the total amount of entries needed is 21.3, as $P(\geq 16|21.3) = 0.90$, and consists of background (μ_b) and the *least detectable signal* (μ_{lds}). With $\mu_b = 3$, the final lds is found by $\mu_{lds} = 21.3 - \mu_b = 18.3$. The MDF will be $18.3/10 = 1.83$. Changing the cut values will result in a different MDF value, providing a search for the minimal MDF, and therefore the best signal over background ratio.

Comparing the methods and final filter level

After performing an iterative grid search for each cut on the different parameters, the three methods gave different optimum cuts, which are summarized in table 4.4. The true signal over background ratio ($r_{true} = \frac{\mu_{signal}}{\mu_{background}}$) is calculated. Naively, one could argue that the best cut values are obtained by the "hard cut" method, providing the highest r_{true}. However, only 11% of the signal neutrinos are kept for the final data-sample. In view of the (small) amount of GRBs used in this analysis and the low number of expected neutrino signal per GRB (on average much less than one per GRB), the "hard cut" method is not applicable for our analysis. Furthemore, the analysis method presented in section 5 is able to cope with a certain amount of background events, and needs at least 6 events for a statistical significant discovery. Therefore, the MDP method is used to optimize our final dataset, applying the cut values presented in table 4.4.

Table 4.4: Final cuts comparison

Parameter	$signal/\sqrt{background}$	$signal \times (1 - background)$	MDP method
Opening Angle	2	9	6.5
Paraboloid error	2.2	7.5	6
Rlogl	8.25	11.25	8
Background left	0.0003 %	10.69 %	0.10 %
Signal left	11.2 %	80.3 %	60.0 %
r_{true}	$3.7 \cdot 10^4$	7.5	600

Chapter 5

Method of the analysis

The IceCube detector is rapidly increasing in size and advancing technically in each year of its building phase, which takes place during summer months at the South-Pole. During the winter months, stable data runs are taken with a specific geometry of the detector. Each year can be analyzed separately, optimizing the analysis as one learns from the previous analyses. Compared to the 4 years AMANDA analysis of Martijn Duvoort [24], much is improved. The DOMs are improved with better readout, the detector volume has increased by an order-of-magnitude with respect to the AMANDA detector, and the ice-properties are much better understood, enabling a better simulation of the detector. The track reconstructions have been optimized to an accuracy of better than 1 degree.

Below a possible improvement is presented for the data-analysis method that is used in this report. Not only the arrival time of the neutrinos can be used to provide a signal when stacking the information of the GRBs. A method will be provided to use the information of the angle between the reconstructed track and the position of the GRB as well as the timing of each event. With these techniques, the potential of a discovery is increased.

Different analyses have been performed on the IC40 data, such as a model based search for prompt neutrino signals by Kevin Meagher [87], using the time and space difference of the neutrinos and the gamma-rays as a weight. A model-independent analysis was performed by Nathan Whitehorn [88], which is also sensitive for precursor and after-glow neutrino signals by using variable time windows around the time of the detected GRBs (the so-called GRB trigger-time).

The analysis that is outlined here is also sensitive to precursor and after-glow neutrino signals, as well as prompt neutrinos, within one hour before and one hour after the GRB trigger-time. Furthermore, by using different parameter cuts for our data, the final data-sample is optimized for neutrino signals with an E^{-2} spectrum. It has been demonstrated that the neutrinos from an E^{-2} spectrum yields the same signal in our detector as a Waxman-Bahcall spectrum, which would result in the same optimizing cut values (see section 4.5) [24]. The analysis can be viewed as a complementary analysis to the previous IC40 GRB neutrino searches, and as a follow-up on the analysis of Martijn Duvoort, who used a similar procedure in his analysis on AMANDA data [24].

Because of the small number of events in the final data-sample, a Bayesian method is chosen to determine if a significant signal is seen. The basic idea, the statistical method and a sensitivity analysis was derived by Nick van Eijndhoven in 2007, [89].

5.1 Time window stacking procedure

The most widely accepted model that describes the actual emission of radiation of the GRB is the fireball model [90]. Regardless of the actual mechanism that initiates the GRB, a jet of relativistic moving material is formed close to a heavy, dense compact object such as a Black Hole. The jet material punches through the dense material that surrounds the compact object.

In the jet, electrons and positron are expected to be accelerated, emitting synchrotron radiation and possibly Inverse Compton scattering due to present magnetic fields. Some models also predict acceleration of heavier charged particles, like protons and nuclei. These models describe the production of high-energy ($\sim 10^{14}$ eV) neutrinos due to charged pion production by proton-photon interactions, described in section 2.2. The neutrino spectrum of a GRB is usually described by the Waxman-Bahcall spectrum that is based on the observed gamma-ray photon spectrum of the GRB, see section 2.2.2.

The cross-section of neutrinos (that interact via weak-interaction) is much smaller than for the photons. As such, the produced neutrinos in the GRBs are able to escape earlier than the photons, because the jet will evolve from a hot optically thick plasma from which only produced neutrinos can escape, to a cooler optically thin plasma from which also photons are able to escape. However, the assumption that is made for this analysis is that all GRBs in the sample arise from the same generic mechanism, providing that the time difference at the source between the produced neutrinos and the photons is the same for all the GRBs in our final sample.

As Martijn Duvoort showed in his GRB analysis [24] with the AMANDA detector, the low mass of neutrinos will only result in an arrival time difference at Earth of the order of a microsecond, between a photon and neutrino that are produced simultaneously. This is negligible for the time resolution foreseen in the current analysis. The cosmological time dilation for each GRB separately will affect the arrival time of both the neutrinos and the photons equally. The median spread in arrival time of the gamma-ray photons will give a good indication of the spread in neutrino signal. However, the cosmological time dilation will influence a possible time difference between the arrival times of the neutrinos and photons from different GRBs. As such we will be restricted in the choice for our time binning as explained below.

Because the details of the GRB mechanism are unknown, the analysis aims to be as model independent as possible. Therefore, it aims to be able to detect a neutrino signal arriving within one hour before, and one hour after the GRB trigger-time. The two-hour windows per GRB are split up in bins of 60 seconds, and stacked upon each other. Whatever mechanism lies at the origin of the GRB, the neutrino signal with respect to the gamma-rays are expected to arrive at a comparable time difference for each GRB and are therefore expected to cluster within a single time-bin. Providing a large enough time window is chosen, the neutrino signal of all the GRBs will reinforce each other, increasing the discovery potential every time a GRB is added to the sample.

The time bins are chosen to be wide enough to capture all the neutrino signals in one bin, but not too wide, as the background increases linearly with the integration time. The choice for 60 second bins was made by Duvoort in [24]. It was based on the median of the spread of the arrival window of the prompt gamma-rays, the so-called $< T_{90} >= 30$ seconds[1]. As the GRB trigger can reside anywhere in the time duration of the gamma-ray signal, the time bin is taken to be twice the median of the duration.

The number of background events in the final data-sample are maximally decreased by several cuts and filters, described in section 4.6.1. However, a certain amount of background events is inevitable. Unlike the expected signal events that are expected to cluster in a single time-bin, the background events that manage to pass our filters and point back to a GRB within the two-hour time-window, will follow a random uniform distribution in our time-window. This enables our method to cope with a certain amount of background event. The principle of the analysis method presented here is to find the significance of observing a certain amount of signal events that cluster in a particular time-bin, compared with the total amount of (randomly distributed background) events in our two-hour time-window.

The time-window stacking procedure is illustrated by a toy-model in Figure 5.1(a). The signal events are drawn in blue, and cluster in the center time bin. The background events are illustrated in red and are uniformly distributed in the other time-bins.

5.1.1 Time dilation

As Gamma-Ray Bursts are located at cosmological distances, cosmological time dilation needs to be taken into account. The Universe expands while the neutrinos travel towards Earth, GRBs at different distances will exhibit different time dilations when observed at Earth.

The analysis is based on the assumption that generic mechanisms for all the GRBs in our sample will be similar, yielding a more or less generic time difference, $\mathrm{d}t_{source}$, between the production-time of the neutrino and of the escaping gamma-rays. However, due to the different distances at which the GRBs are located, the time difference that is observed at Earth, $\mathrm{d}t_{Earth}$, will be stretched by a factor of $z + 1$, where z represents the redshift of the source. Due to the fact that GRBs are located at different distances from Earth, different

[1]The T_{90} parameter represents the time in which 90% of the prompt gamma-ray photons are detected, running from 5% to 95% of the detected signal.

redshifts z are observed[2]. The stacking procedure of the time-windows for all the GRBs will introduce a spread in the $\mathrm{d}t_{Earth}$. To ensure the signal neutrinos will still cluster in the same time-bin, we enlarge the width of every time-bin by a factor $< z > \; + \; 1$ with respect to the previous bin from the center bin onwards [24]. The average redshift $< z >$ for the GRBs in our final data-sample is approximately 2, such that the bins are enlarge with a factor of 3 compared to the previous bin[3]. Thus, our stacked two-hour time-window will be split up in 9 bins (in seconds) accordingly; [-3600,-1200], [-1200,-390], [-390,-120], [-120,-30], [-30,30], [30,120], [120,390], [390,1200], [1200,3600]. See Figure 5.1(b), which illustrates the variable time-binning.

Using variable time bins will have an influence on the sensitivity of our analysis. When the width of a bin is enlarged, the average number of background events in the bin is increased, which decreases the significance of an observed number of signal events in that bin. Although the width of the center bin will remain 60 seconds in case of the variable bin size method, it has been found that the significance of the observation (the so-called $P - value$ which is obtained by the Ψ method explained in section 5.2) for signal events clustering in the center bin is also affected by the use of variable binning [24]. To illustrate this effect, a comparison is made between two time-profiles using a fixed and variable binning respectively. A toy-model example is chosen with 10 background events uniformly distributed in the two-hour window, see Figure 5.1(a) and 5.1(b) for the fixed and variable binning respectively. The significance of the observation is determined, for various number of signal events that fall in the center bin. The $P - values$ are provided in table 5.1.1, which show that the significance is slightly lowered by the use of variable bin sizes. This is the price paid to include the time dilation effects for the arrival time-difference of neutrinos and photons from different GRBs.

Note that the analysis method can also be performed on a single GRB data-set. In such a case, a fixed binning method is appropriate. In the further description of the analysis method, the "regular" 60 second time bin is used to explain the statistical approach of the analysis. This is done to facilitate a comparison between the studies of Nick van Eijndhoven [89] and Martijn Duvoort [24].

5.2 Ψ statistics

A toy-model is introduced to illustrate the method that will be used to determine the significance of an observation in this analysis. The toy-model example is the same that has been used by Martijn Duvoort in [24]. After all cuts and filters have been performed on the toy-model data (see sections 4.4 and 4.6),

[2]The highest redshift observed to date is 8.2 for GRB 090423 [91]. Although this GRB was detected during the period of data taking by the IC40 detector, it cannot be incorporated into our GRB catalog as the GRB 090423 did not lay in the Northern Hemisphere

[3]For a total of 18 GRBs, which were detected by the SWIFT satellite, a calculation of the redshift was possible, by the UVOT, XRT and GROND ground based telescopes.

n_{signal} central bin	P-value regular 60 s bins	P-value variable bins
1	6.32×10^{-2}	2.36×10^{-1}
2	9.67×10^{-3}	3.77×10^{-2}
3	1.13×10^{-3}	3.14×10^{-3}
4	42.71×10^{-5}	1.80×10^{-4}
5	1.1×10^{-6}	7.8×10^{-6}
6	1×10^{-8}	2.2×10^{-7}

Table 5.1: Comparison between the significance for variable time bins and regular 60 seconds time bins. The center bin contains n_{signal} number of entries. Table is from Martijn Duvoort, [24]

the final data-sample consists of 13 events, distributed in the two-hour window, see Figure 5.1(a). The 13 events consist of 10 background events randomly distributed over the 2 hours, and 3 signal events, which all fall in the same time bin. However, because 13 events are distributed in 120 bins, the fact of having a bin filled with 3 entries is not so significant. Determination of the significance can be performed in several ways. The analysis method presented here uses an exact Bayesian method, the so-called Ψ statistics, described in full detail in [89].

To understand the approach of the Ψ statistics method, the Bayes theorem is rewritten as

$$\frac{p(H|DI)}{p(H_*|DI)} = \frac{p(H|I)}{p(H_*|I)} \frac{p(D|HI)}{p(D|H_*I)} \tag{5.1}$$

where H is an hypothesis, and H_* is the hypothesis that H is not true. D is the observed data and I is some prior information. The evidence that H is true relative to when H is not true, can be expressed in a intuitive decibel scale as

$$e(H|DI) \equiv 10 \log_{10} \left[\frac{p(D|HI)}{p(D|H_*I)} \right] \tag{5.2}$$

so that with equation 5.1 we obtain

$$e(H|DI) = e(H|I) + 10 \log_{10} \left[\frac{p(D|HI)}{p(D|H_*I)} \right]. \tag{5.3}$$

Now, the Bayesian observables are introduced, $\Psi \equiv -10 \log_{10} p(D|HI)$ and $\Psi_* \equiv -10 \log_{10} p(D|H_*I)$. Since for a probability $p \leq 1$, the Ψ values are by definition positive. Combined with equation 5.2 this yields for the evidence that H is not true:

$$e(H_*|DI) = e(H_*|I) + \Psi - \Psi_* \leqq e(H_*|I) + \Psi. \tag{5.4}$$

This shows, that the evidence that H is not true (H_*) according to the data and a prior I, cannot be bigger than the evidence that H_* is true according only to some prior information plus the Ψ value for H. In other words, the Ψ

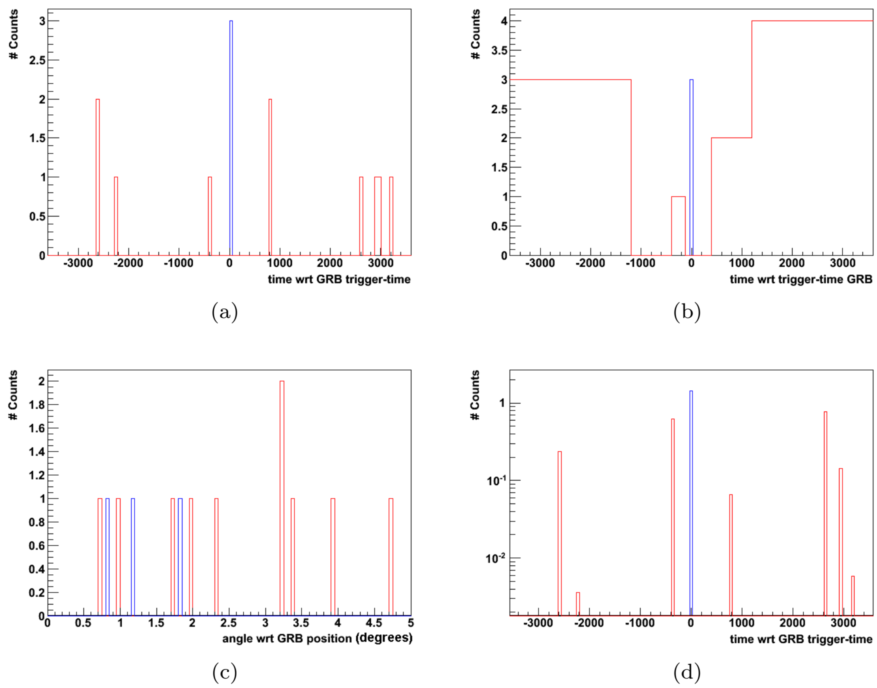

Figure 5.1: (a)This time histogram illustrates a toy-model situation, where three signal events cluster in the middle time bin, and the other ten background events are randomly distributed in the two-hour time-window. The bin-width is 60 seconds, and the GRB trigger-time determines the middle (zero) bin. All signal events are illustrated in blue, and the background events in red. To account for the time dilation effects between the different GRBs for which the time-windows are stacked, a variable time binning is needed, illustrated in Figure (b). Figure (c) illustrates the randomly taken angles for signal events (blue) and background events (red) with respect to the GRB position. For the toy-model example, two background events lie very close to the GRB position, as well as the signal events. Figure (d) illustrates the weighted time-window of the toy-model. It shows a suppression of most of the background events because of their low weight ($0 < weight < 1$). Also the signal events are weighted, which lowers the value in the center bin accordingly. Further details can be found in the text.

value (in dB) gives a degree of support for the hypothesis H to be false. By determining the Ψ value of our final data-sample, an exact calculation can be provided to investigate if the data shows significant deviation from an assumed background distribution.

The background distribution is given by the multinomial distribution from [92] in the case of N trials and m possible outcomes, following

$$p(n_1, n_2 n ... N_m|Nm) = \frac{N!}{n_1!...n_m!} p_1^{n_1} ... p_m^{n_m} \equiv p, \tag{5.5}$$

which also reflects the probability of a certain distribution of N entries (events in the final data-sample) distributed in m bins (120 bins of 60 seconds in our case). p_i represents the probability of a certain entry falling in bin i, which is static and independent to any other bin.

Combining equation 5.5 with the Ψ values defined above, an exact Bayesian Ψ value can be determined for each distribution of events as

$$\Psi = -10 \left[\log_{10} N! + \sum_{k=1}^{m} (n_k \log_{10} p_k - \log_{10} n_k!) \right] \tag{5.6}$$

Unlike the so-called "frequentist" approach explained in section 5.2.2, the Ψ method does not investigate the significance of a certain number of events found in one particular time bin, but rather determines if the two-hour time-distribution as a whole deviates from a background distribution.

The probability of a background event falling in a particular bin is $p_i = 1/m$, as the background is distributed uniformly over m bins. However, the method is also capable of using a non uniform p_i, if the background rate changes in the two-hour time-window. By using a non-uniform background distribution to calculate the Ψ value, it is possible to incorporate certain asymmetry features of the detector or changes in the background rate, see section 6.1.2. Also other parameters, such as the angular difference between the GRB and the track, can be included into this method, using a non-uniform background distribution. As will be shown below, this could lead to an improvement of the discovery potential of the analysis.

The actual Ψ value of the toy model presented above, is found to be $\Psi_{observed} =$ 186.15. This value on itself does not tell us much about a possible signal, because the distribution of all the background Ψ values depend on the total number of events N and all possible configurations over the m bins. The $\Psi_{observed}$ needs to be compared to this background distribution of $\Psi_{background}$ to determine how significant the deviation is. There are two ways of determining this significance, one way is to calculate directly what the probability is for all the possible distributions. By calculating all the probabilities of all the distributions that can be found with a higher Ψ value, the significance (i.e. $P - value$) is acquired. In the second method the observed distribution is randomized numerous times, and the number of distributions with $\Psi_{random} \geq \Psi_{observed}$ relative to the total number of randomizations is determined. This second method is faster for a larger number of total events N, but intrinsically is subject to some statistical uncertainty. Both methods are described in more detail below, and will give a similar $P-value$, which is an indication on the significance of the $\Psi_{observed}$. The accepted criterion for claiming a discovery is $P < 5.73 \times 10^{-7}$, corresponding with the area under the 5σ tails of a Gaussian function.

Direct calculation of the P-value

The direct way to calculate the $P-value$ is by determining the probability of all the possible distributions of N events distributed over the m bins. This method gives an exact $P - value$, but is slow when dealing with a large N, because of the increasing number of possible distributions. Furthermore, to calculate the $P - value$ for an observation that has a non-uniform background distribution (see section 5.3), as well as for the weighting method described in section 5.3.1, this direct calculation method is not applicable. The total number of possible Ψ values become to large in these situations.

The number of possible configurations is determined by the Binomial configuration,

$$N_{config} = \frac{m!}{(m-k)k!}\frac{k!}{\prod_{j=1}^{N} x_j!}\frac{N!\prod_{k=0}^{N} p_k^{n_k}}{\prod_{k=0}^{N} n_k!} \tag{5.7}$$

where m, k and N are the total number of bins, the number of events in a specific bin and the total number of events respectively.

The first factor of the expression on the right-hand side gives the total number of possible configurations to find k events distributed over m bins. For example, two entries falling in either one of three bins, can be distributed in three different ways, (200, 020, 002).

The number of times that a specific content j can occur is taken into account by the second factor. In the example given above, one can interchange the (0) in the configuration (200), without changing the distribution.

The probability of every configuration is calculated by the last factor of the equation.

With the number of configurations and the probability of every configuration at hand, one can find the total probability of getting $\Psi_{background} \geq \Psi_{observed}$. In this manner one calculates the exact $P - value$.

An iterative method for calculating a P-value

The second method for determining the $P - value$ is by randomizing the total number of N entries multiple times over m bins, assuming some background distribution. A uniform distribution is assumed here, corresponding to the observed time histogram. This method is also capable of using non-uniform distributions (see section 5.3). By adding all the number of distributions that have $\Psi_{random} \geq \Psi_{observed}$, the $P - value$ is determined as

$$P - value = \frac{n(\Psi_{rndm} \geq \Psi_{observed})}{\#_{randomizations}} \tag{5.8}$$

In other words, when observing a high $\Psi_{observed}$, a small number of Ψ_{rndm} are generated with a higher value, yielding a small $P - value$. This indicates that the observed distribution is not compatible with the background.

The corresponding $P - value$ of a 5σ discovery must be $< 5.73 \times 10^{-7}$. In the case of a (very) large $\Psi_{observed}$, which would be significant enough for a 5σ discovery, approximately one generated Ψ_{rndm} will be larger than the $\Psi_{observed}$ in $\sim 10^8$ generated randomizations. Therefore, to minimize the statistical fluctuations that are subjected to this method and to be able to obtain a non-zero $P - value < 5.73 \times 10^{-7}$, at least 10^9 random trials are generated.

Figure 5.5(a) shows the distribution and specific $\Psi_{observed}$ (blue line) for the GRB toy-model given above. The $P - value$ for this specific toy-model is $P = 1.13 \times 10^{-3}$, which will not result in a discovery.

5.2.1 The "unblinding" procedure

For every analysis that is performed on data from the IceCube detector, a so-called "unblinding" of the data has to be granted by the collaboration, before someone is allowed to perform an analysis on the final data-sample to define the significance of the observation. The sensitivity of the method and how background events are reduced need to be determined a-priori (without knowledge of the actual observation), using a separate data-set that is independent of the final data-set. This procedure was followed in section 4.6.1 to determine the parameter cut values by using an "off source / off time" data-sample. In other GRB analyzes methods mentioned in the beginning of the report [87] [88], also the signal sensitivity is obtained in this manner.

In the presented analysis, the total number N of events in our final data-sample as well as the background Ψ_{random} distributions are determined using the final data-sample, although the data is still not "unblinded" at this point. Namely, the Ψ_{random} distribution only depends on the total number of events in the final data-sample, N, and the number and width of the bins m. This allows us to determine the sensitivity of the method, by calculating how many (signal) events are needed in a bin (for example the center bin) to claim a 5σ discovery. The final data-sample is "unblinded" by determining the specific time-distribution of the final data-set that yield one $\Psi_{observed}$ value, from which the $P - value$ follows. Although the "unblinding" procedure lies beyond the scope of my thesis research, a sensitivity of the method is determined accordingly in chapter 7.

5.2.2 A comparison with Poisson statistics

To determine the significance of the deviation of the observed data-sample from a general background distribution can also be done in an other way, by using the so-called "frequentist" approach. The difference between the two methods was investigated by Martijn Duvoort in [24], and a short outline of his work is given here.

The principle difference of the Ψ method compared to the "frequentist" approach is that the Ψ method evaluates the probability of the total two-hour time distribution with the multinomial distribution of equation 5.5, whereas the "frequentist" approach investigates the probability of finding a certain number of events in a single bin separately.

For a total number of events N that are randomly distributed over the two-hour window, the average number of events per bin is given by $\mu = N/n_{bins}$, with n_{bins} the number of bins in the two-hour time window. Thus, each bin has a constant number of expected background events. The number of entries per bin is therefore described by a Poisson distribution. The probability of finding n_i entries in bin i is given by

$$p(n_i|\mu_i) = \frac{e^{-\mu_i}\mu_i^{n_i}}{n_i!}. \tag{5.9}$$

The mean number of entries $\mu_i = \frac{N}{n_{bins}}$, is a real number. Applying this probability to the example above with 10 background events and 3 signal, we find a $P - value$ of $p(3|13/120) = 1.9 \times 10^{-4}$. This looks very promising, but one has to take the so-called 'trial factor' into account when using this method. The method calculates the probability of finding a certain amount of entries in a specific bin, but it can be any of the 120 bins in the two-hour window. The Poisson distribution in each bin gives rise to statistical fluctuations, which has to be taken into account when providing the correct $P - value$. In a first order approximation, the $P - value$ has to be corrected as follows;

$$P_{after-trials} = N_t \times P_{before-trials} \tag{5.10}$$

where N_t is the number of trial factors, in our case the number of bins (120). In our example this gives a corresponding realistic $P - value$ of $P = 1.9 \times 10^{-4} \times 120 = 2.28 \times 10^{-2}$. This is larger than the $P - value$ ($P_\Psi = 1.13 \times 10^{-3}$) found by using the Ψ statistics.

The fact that we find a more conservative $P - value$ when using the "frequentist" approach is due to the following reason. We consider an experiment which has two outcomes, a and $\bar{a}$ (not a), with a probability p and $\bar{p}$ respectively. Because only two outcomes are possible, $\bar{p} = 1 - p$. Thus, the probability of observing $\bar{a}$ in two subsequent experiments is given by

$$\bar{p}^2 = (1-p)^2 = 1 - 2p + p^2 \tag{5.11}$$

For a small probability of finding a, $p^2 \approx 0$ and the equation above simplifies to $\bar{p}^2 = 1 - 2p$. Following this reasoning for n independent measurements of $\bar{a}$ will yield a probability

$$\bar{p}^n = 1 - n \cdot p + (n-1) \cdot p^2 - (n-2) \cdot p^3 + (n-3) \cdot p^4 ... \tag{5.12}$$

A plus sign occurs for every even order term, which is the reason that the probability of finding no observations, $\bar{p}^n$, is less constrained by the probability of an observation multiplied by the trial factor, $\bar{p}^n > 1 - n \cdot p$. Therefore, the "frequentist" approach would yield a too conservative $P - value$ for the observation. [24]

A second reason why the "frequentist" approach using Poisson statistics will not result in the same $P - values$ as the exact values from the Ψ statistics, is that the total number of events N, from which the average number of background events per bin is determined following equation 5.9, is actually a single measurement of an underlying $< N >$. The probability of finding a certain number of events in a bin is dependent on the mean number of events per bin, which will not be exact following this approach. The Bayesian Ψ approach does not have this artifact and provides therefore exact results [24].

It has been shown by Martijn Duvoort [24] in an extensive comparison that the "frequentist" approach using Poisson statistics gives a more conservative $P - value$ than the Bayesian Ψ statistics for various example distributions. A summary of this study is given in appendix C. Due to the exact results of the Ψ statistical approach and the fact that Poisson statistics yield a conservative $P - value$, the choice for using Ψ statistics in this analysis is made.

5.3 Improving the analysis

The method as it has been described above, is sensitive for a neutrino signal that clusters in a single time-bin in two-hour time-windows around each GRB trigger-time. One expects a low number of neutrinos (a few at best) from any individual GRB. The possibility of detecting GRB-associated neutrinos can therefore be enhanced by considering a large number of GRBs, using a stacking procedure already described earlier. Due to the methods clever statistical approach, specific asymmetry features in the background distributions are automatically incorporated (see section 6.1.2), and implementing different improvements to the method is relatively simple. As will be shown below, an improvement in the sensitivity of the method can be obtained by using the angle between the GRB position and the direction of the reconstructed tracks. Moreover, the method that will be described (specifically in section 5.3.2) can be generalized, as other parameters such as the (reconstructed) energy of the event could also be used following the same optimization procedure, provided that they are independent of the time of the event with respect to the GRB trigger-time.

Not only the signal neutrinos are expected to fall in the same time-bin in our two-hour time-window, the direction of the neutrino will also point back to the GRB position in the sky. The direction of the neutrino is not affected throughout its journey towards the Earth, apart from gravitational effects that also affects the photon signal in a similar way. On the other hand, the background events will have a random distribution with respect to the GRB position.

In Figure 5.2(a) the distribution function of the angle (α) between the line-of-sight to a GRB position and the reconstructed track is illustrated, for background (red) and signal (blue) events. The expected number of events within an opening angle around a GRB position (a cone around the line-of-sight of a GRB), scales with the area of the cone, $\sim \pi\alpha^2$, for $\alpha << \pi$. The number of events with a specific angle α in the range $\alpha, \alpha + d\alpha$, will scale with the area of a ring ranging from $\alpha \rightarrow \alpha + d\alpha$, the area from which the tracks are directed. The area of the ring is given by

$$\begin{aligned} A_{ring} &= \pi(\alpha + d\alpha)^2 - \pi\alpha^2 = \pi \cdot \alpha \cdot d\alpha + \pi \cdot d\alpha^2 \\ &\simeq \pi \cdot \alpha \cdot d\alpha \text{ for } \alpha << \pi \text{ and } d\alpha << \pi. \end{aligned} \tag{5.13}$$

Thus, as the background events are uniformly distributed in the area around the GRB position, the number of background events with a specific angle α in the range $\alpha, \alpha + d\alpha$ is

$$\mathrm{d}n = B\pi\alpha\mathrm{d}\alpha, \tag{5.14}$$

where B is a normalization constant. The distribution function of the angle of background events is illustrated by the red line in Figure 5.2(a).

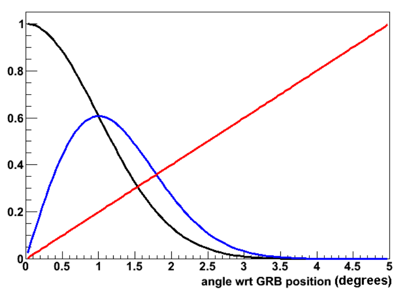

(a)

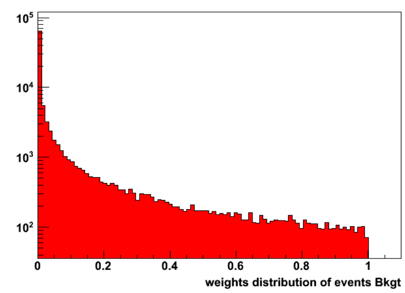

(b)

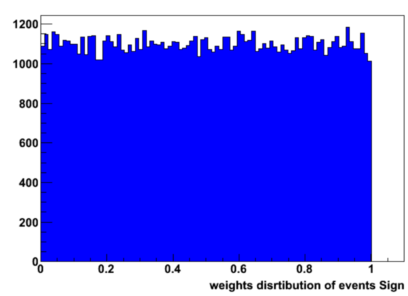

(c)

Figure 5.2: (a) This figure illustrates the distribution function of the angle between the line-of-sight of a GRB and the direction of a reconstructed track for signal events (blue) and background events (red). The weighting function ($G(\sigma, \alpha)$) is drawn in black, and the standard deviation $\sigma = 1$. (b) The weight distribution for background events is illustrated, for a weight between 0 and 1. (c) The weight distribution is plotted for signal events, which have an angular distribution function as drawn in (a). Further details can be found in the text.

The reconstructed track of a signal event will deviate by a small angle from the arrival direction of the neutrino, due to the detector resolution and the $\nu_\mu \to \mu$ interaction. The angular deviation of the reconstructed track with respect to the neutrino direction of flight (which is equal to the GRB position) is given by a Gaussian function $G(\sigma, \alpha)$. The probability of finding a reconstructed track with an angular deviation from the neutrino direction of flight α in the range $\alpha, \alpha + d\alpha$ is

$$\mathrm{d}P_\alpha = \frac{1}{\sqrt{2\pi\sigma^2}} \exp(-\alpha^2/2\sigma^2)\ \mathrm{d}\alpha \equiv G(\sigma, \alpha)\mathrm{d}\alpha. \tag{5.15}$$

The standard deviation of the Gaussian function σ determines the angular resolution in the track reconstruction. Here $\sigma << \pi$ as such that the possible angle α is finite and $\alpha << \pi$.

As for the background events, the number of signal events with an angle α in the range $\alpha, \alpha + d\alpha$ need to be scaled with the factor $\mathrm{d}\Omega \simeq \pi\alpha\mathrm{d}\alpha$ due to the increased area of a ring between $\alpha \to \alpha + \mathrm{d}\alpha$ around the GRB position. This leads to an expected number of signal events with an angle α in the range $\alpha, \alpha + d\alpha$ following

$$\mathrm{d}n = C_\sigma\ \alpha\ \exp(-\alpha^2/2\sigma^2)\ \mathrm{d}\alpha = D\ \alpha\ G(\sigma, \alpha)\ \mathrm{d}\alpha, \tag{5.16}$$

where C_σ and D are normalization constants. The distribution function is illustrated by the blue line in Figure 5.2(a).

The standard deviation of the Gauss $G(\sigma, \alpha)$ is determined by the resolution of the detector ($\sigma_{detector}$) and the GRB position($\sigma_{GRB-position}$), following

$$\sigma = \sqrt{\sigma^2_{detector} + \sigma^2_{GRB-position}}, \tag{5.17}$$

which is specific for each GRB, as the position accuracy is different for each GRB. The toy-model example that is used below has a uniform standard deviation of $\sigma = 1$.

It is noted that the angular distribution for the signal and background is different, see Figure 5.2(a). This indicates a potential improvement of the analysis method. In the following sections, two different procedures are described to combine the angular information of a track and the event-time with respect to the GRB trigger-time. In the first method the events in the time-window acquire a weight which is related to the angle of a track with respect to the GRB position. The second method uses the calculation of a Ψ_{angle} value for the angular distribution of events, in a similar way as a Ψ_{time} value is calculated in section 5.2. An improvement of the sensitivity of the methods are investigated in section 5.3.3.

Determining the sensitivity of a method

To determine the sensitivity of an analysis method, we calculate the minimal number of signal events that are needed to claim a 5σ discovery, for a fixed total number of events N. In case of the Ψ analysis explained above, the presented toy-model example results in one specific $\Psi_{observed}$ value. However, if the 10 background events would have clustered together in only a few time bins, a different $\Psi_{observed}$ value would have been calculated. In such a case, we would still be dealing with 3 signal events and 10 background events, although the $\Psi_{observed}$ value is different than in our original toy-model example. This effect is the principle behind the iterative $P - value$ calculation and equation 5.8, where only background events are used to determine a range of $\Psi_{rndm-bkgt}$ values that result in a background Ψ_{rndm} distribution.

To determine the sensitivity of the method, this effect is incorporated by determining the *minimal number of signal events* (n_{mns}) that will result in a 5σ discovery in 50 % of the cases. Therefore, the median value of the $\Psi_{rndm\ sign+bkgt}$ distribution is determined, by generating distributions with a fixed number of signal and background events. Then, a $\Psi_{5\sigma}$ value is determined, which is the minimum Ψ value that will result in a 5σ discovery. For a certain number of signal events, the median value of the $\Psi_{rndm\ sign+bkgt}$ distribution will be larger than the $\Psi_{5\sigma}$ value. This number of signal events will thus result in a 5σ discovery in 50 % of the cases, yielding the n_{mns}.

The n_{mns} will be compared for the original analysis method as well as for the new improved methods that are described below. A lower n_{mns} is found for a method with a better sensitivity, as a lower number of signal events is needed to claim a 5σ discovery.

The procedure is illustrated by Figure 5.3 where two Ψ distributions are drawn. The black distribution illustrates the Ψ values using only background events and the blue distribution is determined by using 3 signal and 10 background events. Note that the Ψ distribution relates to the improvement method explained in section 5.3.2, which is different than the Ψ distribution of the time histograms of section 5.2 illustrated in Figure 5.5(a).

5.3.1 Time-bin Weighting Procedure

One way to combine the information of the angle and time of a track with respect to the GRB position and trigger-time respectively in an analysis, is by assigning a specific weight to each event. The events can be weighted with a Gaussian function $G(\sigma, \alpha)$, which is illustrated by the black line in Figure 5.2(a). Specific (randomly chosen) angles are generated for signal and background events (see Figure 5.1(c)) according to the angular distribution functions of equations 5.14 and 5.16. Weights are assigned to each event according to the angle between the track and the GRB position. This yields a 'weighted time-window', illustrated by the toy-model example in Figure 5.1(d).

The excess in number of (signal) events in the center bin compared to the average background rate is enhanced by the weighting procedure. Note that the number of events in the center bin is also decreased due to the weighting of the signal events, however the majority of the background events are suppressed more substantially. The distributions of the weights for signal and background events will be discussed below.

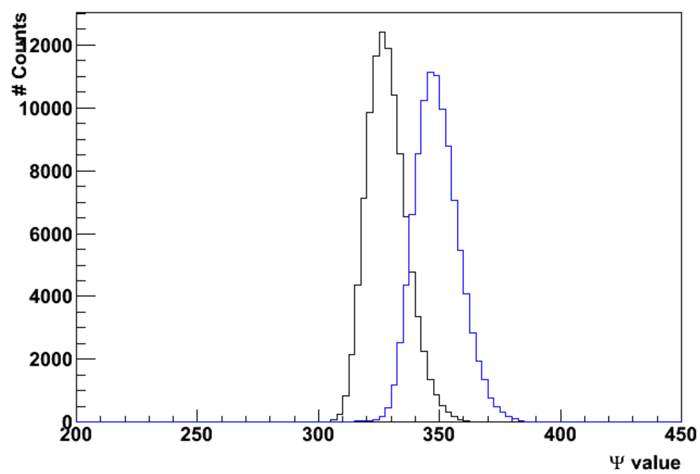

Figure 5.3: The Ψ_{total} distributions are shown for only background randomizations (black) and signal + background randomizations (blue). Note the wide spread in Ψ_{total} distribution for the signal+background. Having 3 signal and 10 background events does not yield one specific $\Psi_{angle-observed}$ value. Further details in the text.

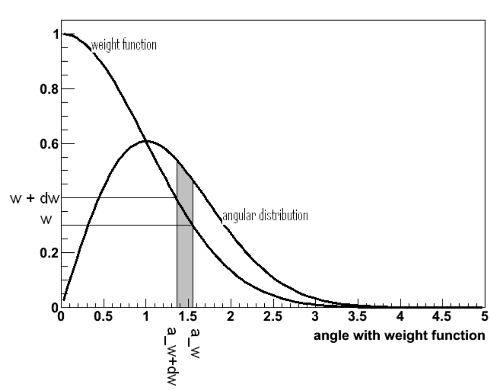

Figure 5.4: The weighting function is illustrated as well as the distribution function of the signal events.

Distributions of the weights

Overall, the weights of the background events will be lower than the weights for the signal events, as they will generally have a larger opening angle with respect to the GRB position. The weights of the background events are predominantly small ($<< 1$), whereas the weight of the signal events are uniformly distributed between 0 and 1, illustrated in Figures 5.2(b) and 5.2(c). The uniform distribution of the weights for signal events might be counter-intuitive, but will explained mathematically below.

When determining the distribution of the weight, one must calculate the number of events with a weight between w and $w + \Delta w$. Figure 5.4 shows the distribution function of the angle between the track and the GRB position of signal events, given by $D \cdot \alpha \cdot G(\sigma, \alpha)$, where D is a normalization factor and α the angle. The weighting function is also drawn and given by the Gaussian function $G(\sigma, \alpha)$.

The standard deviation value σ of the two Gaussian functions are the same and is determined by equation 5.17. The σ will not be constant for all GRBs in our sample because it depends on the non-uniform accuracy of the GRB positions, $\sigma_{GRB-position}$. However, the signal distribution of Figure 5.2(a) will be affected similarly. Consequently, the non-uniform $\sigma_{GRB-position}$ does not affect the essence of the method. However, in the second method described below, this feature has to be considered with more care. We will use a standard deviation of $\sigma = 1$ for our toy-model examples.

A weight $w(\alpha)$ can be attributed to each event with angle α between the track direction and the GRB position. When the distribution function for the angle is given by equation 5.16, the probability $\mathcal{P}(w)$ to find a certain weight w in a range $w, w + \mathrm{d}w$ follows from

$$\mathrm{d}n = \mathcal{P}(w)\mathrm{d}w = C_\sigma \alpha \, \exp(-\alpha^2/2\sigma^2)\mathrm{d}\alpha. \tag{5.18}$$

This results in the probability

$$\mathcal{P}(w) = C_\sigma \alpha \, \exp(-\alpha^2/2\sigma^2) \left| \frac{\mathrm{d}\alpha}{\mathrm{d}w} \right| = C_\sigma \alpha \, \exp(-\alpha^2/2\sigma^2) \left| \frac{\mathrm{d}w}{\mathrm{d}\alpha} \right|^{-1}. \tag{5.19}$$

The absolute signs will ensure that the probabilities are kept positive. The weighting function $w(\alpha)$ needs to be defined for this equation. As mentioned above, a Gaussian function $G(\sigma, \alpha)$ is chosen to weight each event. The fraction including the weighting function of equation 5.19 becomes

$$\left| \frac{\mathrm{d}w}{\mathrm{d}\alpha} \right|^{-1} = \left| \frac{\mathrm{d}G}{\mathrm{d}\alpha} \right|^{-1} = \frac{\sigma^2}{\alpha G(\alpha)}. \tag{5.20}$$

For this choice, the probability distribution function $\mathcal{P}(w)$ for the weights of the signal events is constant, and the weights w will therefore be uniformly distributed between 0 and 1, see Figure 5.2(c).

Since the average angle between the original (MC) track and the reconstructed track is described by the 'central limit theorem' (CLT) [4], the most realistic weighting function for our detector is a Gaussian function ($G(\sigma, \alpha)$). It should be noted that the choice of the weighting function $w(\alpha)$ will affect the distribution of the weights for background and signal events, and that other detectors could be described better with another weighting function than a Gauss.

Note that one needs to make an assumption on the accuracy of the track reconstruction method, to determine a specific standard deviation σ for the weighting function. The performance of the improved method relies on how accurate one can determine the correct and most realistic standard deviation σ. For the toy-model used in this section, a standard deviation σ of 1 is chosen.

Ψ method on the weighted events

To asses the significance of the weighted time distribution, we determine the $\Psi_{observed}$ value of the weighted histogram using equation 5.6. Because the events are weighted, the number of events in a bin (n_i) have a non-integer value, but this forms no issue when using equation 5.6, as it is also suitable for non-integer values of n_i.

However, the total number of events N of the weighted distribution, should not change according to the total weights of all the events. A Ψ value, found with equation 5.6, depends on the total number of events N as well as the distribution of the events over the bins. To determine the $\Psi_{rndm-bkgt}$ distribution, as outlined in section 5.2, multiple random distributions with a constant N events are generated in m time-bins according to a known background distribution function. Hence, the $\Psi_{rndm-bkgt}$ distribution is a reflection of the probability of all the possible configurations of events in the time-window. It is therefore important to use a constant N.

In this method the value N is set to 1, so that the Ψ_{bkgt} distribution has no negative values. [5] The direct connection with the multinomial probability function of equation 5.5 is therefore lost, as the real total number of events is **not** equal to 1. However the method works correctly in a similar way as the original Ψ method, as the distribution of the (weighted) events give a specific $P - value$ according to their Ψ_{bkgt} distribution, which is a direct measure of the significance of the deviation of the observation compared to an expected (weighted) background distribution. The weighted Ψ_{bkgt} distribution is illustrated in Figure 5.5(b).

We determine the $\Psi_{rndm-bkgt}$ distribution (illustrated in Figure 5.5(b)) and the corresponding $\Psi_{observed}$ value for the toy-model that was given above. A $\Psi_{observed}$ value of 67.28 is found, which corresponds to a $P - value$ of $3.26 \cdot 10^{-3}$, illustrated by the blue line in Figure 5.5(b). In this example the $P - value$ is

[4] The central limit theorem states conditions under which the mean of a sufficiently large number of independent random variables, each with finite mean and variance, will be approximately normally distributed.

[5] If the normal value N is used together with the weighted n_i, the Ψ values would be negative, due to the relatively large $\log(N!)$ factor of equation 5.6

not improved compared to the original $P-value$ (1.13×10^{-3}). A more detailed investigation on the sensitivity of this method is provided in section 5.3.3.

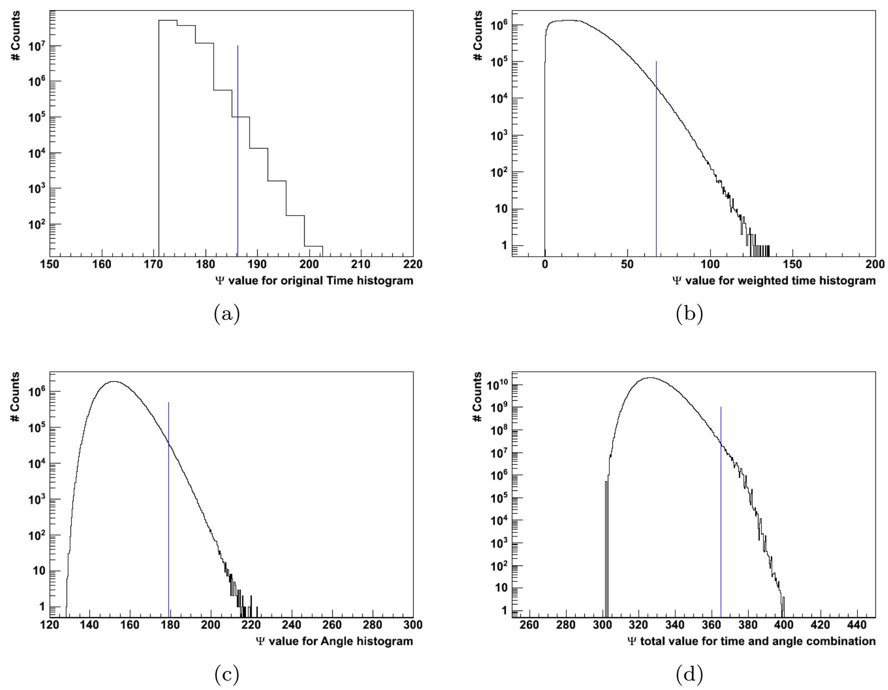

Figure 5.5: Distribution of the randomized background Ψ values are given, with the specific Ψ values of the toy-model example illustrated by the blue lines. (a) The background Ψ distribution of time histogram for the original method. (b) Drawn is the background Ψ distribution for the weighted time histogram. To calculate the Ψ value we set $N = 1$, and use the weights per event to determine $\Psi_{weighted}$. (c) The background Ψ_{angle} distribution is drawn for the angular histogram. Note that the angular distribution is smoother, as far more Ψ_{angle} values are possible due to the non-uniform probability function. (d) The Ψ_{total} value is drawn, by convolution of the Ψ_{time} from (a) and Ψ_{angle} from (c). The P-value is slightly better using the combined Ψ values compared to the Ψ_{time}.

5.3.2 $\Psi_{angle} + \Psi_{time}$ Procedure

A more direct method that combines the angular and timing information of the track is the so-called Ψ_{total} method. For this method the corresponding Ψ_{angle} value is determined for the distribution of all the angles of each track with respect to the GRB position (see Figure 5.1(c)). This Ψ_{angle} value is combined with the (original) Ψ_{time} value of the time-window distribution.

A Ψ_{angle} is determined following equation 5.6. The angular distribution, illustrated in Figure 5.1(c), is split up in 100 bins (n_{bins}) and the (integer) number of events in a single bin is given by n_i, where N is the total number of events. Note that the probability p_i for an event to fall in bin i is **not** constant, as the background distribution function of the angle between the GRB position and the background tracks is not uniform but given by equation 5.14. Thus, the probability function we use to determine the Ψ_{angle} value is

$$p_i = \frac{i}{n_{bins}!} \text{ with } i = 1, 2, ..., n_{bins} \tag{5.21}$$

Tracks with a small opening angle with respect to the GRB position, will induce a high Ψ_{angle} value because the probability p_i is low for those events.

Note that this procedure does not rely on specific assumptions made on the properties of signal events, like the accuracy of the detector. It merely incorporates the (theoretical) background distribution function of the angle between the reconstructed background tracks and the GRB position to determine the Ψ_{angle} value.

However, the 'opening angle' around the GRB position, which indicates the maximum angle between a track and the GRB position, is normally not the same for all the GRBs. The opening angle depends on the accuracy of the track reconstruction, for which we take an average for all GRBs in our sample, as well as the accuracy of the determined position of the GRB, which is different for each GRB. In the procedure described here, we stack all the angular distributions of each GRB. The angular histograms need to have the same size for this stacking procedure, and thus a generic 'opening angle' is needed for all the GRBs in our sample. To use this method for our real experimental data, the spread in accuracy for the GRB position should not be large so that a generic opening angle for all GRBs can be applied. In this section, we use a generic opening angle of 5 degrees for our toy-model example.

The previous toy-model example will yield a Ψ_{angle} value of 179. To investigate the significance of this Ψ_{angle} value, the randomization procedure described in section 5.2 needs to be followed. The direct calculation method of section 5.2 cannot be applied in this case, as the number of different configurations and Ψ values are largely increased due to the non-uniform probability function p_i.

This Ψ_{angle} background distribution is illustrated in Figure 5.5(c). The blue line indicates the Ψ_{angle} value obtained for the specific toy-model example. This Ψ_{angle} on itself yields a $P{-}value$ of $3.95{\cdot}10^{-3}$, which is not significant compared to the $P - value$ of the time histogram ($P_{\Psi time} = 1.13 \times 10^{-3}$).

However, the timing method could be improved by combining the Ψ_{angle} and the Ψ_{time} values. As the Ψ values represent the logarithm of a probability (a degree of support for a background hypothesis), it is provided in a decibel scale. Combining the probabilities of the timing and angular histograms results simply in summation of the corresponding Ψ values. Because the timing histogram is totally independent from the angular histogram, the summation of the different

Ψ values is allowed. The total Ψ value is given by

$$\Psi_{total} = \Psi_{time} + \Psi_{angle} \tag{5.22}$$

To find the final $P - value$ for the combined Ψ values, both the time and angular distributions have to be randomized to determine the Ψ_{total} background distribution. The convolution of the separately generated Ψ_{time} and $\Psi angle$ distributions results in the Ψ_{total} distribution, illustrated in Figure 5.5(d).

The toy-model example given above has a Ψ_{total} value of 365 that yields a $P - value$ of $2.14 \cdot 10^{-4}$. Although this is an improvement compared to the original $P - value$ ($P_\Psi = 1.13 \times 10^{-3}$) obtained by original Ψ_{time} method, an investigation on the improvement of the method will be given below with more statistics, to determine if the method shows a consistent improvement.

5.3.3 Quantifying the sensitivity and discussion

As described in section 5.3, the minimum number of signal events n_{mns} indicates how sensitive a method is. The n_{mns} is equal to the minimal number of signal events that is needed to claim a 5σ discovery in 50% of the cases when we have a constant total number of events N.

To investigate the original method and the two 'improved' methods described above, we determine the n_{mns} for each method using a total number of 30 events ($N = 30$). For a standard deviation of $\sigma = 1$ for the accuracy of the track reconstruction, no difference is seen in the sensitivity for the three methods. However, if we improve the accuracy of the track reconstruction, decreasing the σ, an improvement in the sensitivity is observed. This is summarized in table 5.3.3.

From this table we learn that only the Ψ_{total} method is able to gain some improvement on the sensitivity of the analysis method in case a $\sigma \leq 0.8$ is chosen, compared to the original Ψ_{time} method. The 'weighting method' shows no improvement on the sensitivity at all compared to the original method, as it needs a n_{mns} of more than 10 signal events, compared to 8 n_{mns} for the original method.

The sensitivity of the methods that use the angular information depend on the accuracy of the track reconstruction. However, the determined 'opening angle' around the GRB also depends on the accuracy of the track reconstruction. By improving the σ, the determined 'opening angle' will also decrease. This effect is not taken into account here, although this implies that the sensitivity of the improvement methods compared to the original method is overestimated in table 5.3.3.

The 'opening angle' value is already optimized in section 4.6.2, which indicates that the information of the angle between the track and the GRB position is already used to its full extend. This is demonstrated by the fact that the sensitivity of the original analysis method cannot be improved (substantially) by using one of the new methods presented here.

This section should be viewed as an investigation on possible improvement methods for the Bayesian analysis that is used for the real experimental data

	n_{mns}, $\sigma = 1$	n_{mns}, $\sigma = 0.8$	n_{mns}, $\sigma = 0.5$
Original Method	8	8	8
Ψ_{angle} Method	17	14	11
Ψ_{total} Method	8	7	6
Weighting Method	13	12	10

Table 5.2: Comparison between the sensitivity of three methods, using the original Bayesian statistical analysis method for only the time-distribution (Original Method), a combined method using the angular and time-distribution (Ψ_{total} method) respectively and a weighted time-distribution (Weighted Method).

of chapter 6. Unfortunately the new methods presented here show no real improvement on the sensitivity of the method, however, it has been shown that the Ψ analysis method can incorporate several independent parameters that could help to improve the sensitivity of the analysis. Other parameters such as the energy of an event, which is different for signal events compared to background events, could also be used in a similar way as the Ψ_{total} method described above. This investigation lies beyond the scope of my research and furthermore, such a procedure would make the analysis more model dependent.

Chapter 6

GRB data

The IceCube detector in its 40 string configuration took data between April 5, 2008 and May 20 2009. During this period, 277 Gamma-Ray Bursts were reported by the Gamma-Ray Burst Coordinate Network (GCN), 128 of them were located in the Northern Hemisphere. The GRBs were analyzed and listed by Kevin Meagher for his model dependent GRB analysis, [87]. In short, five GRBs were rejected because the detector was not running in a stable state. In total six bursts were marked faulty by the good run list, [93], but were later on determined usable because the time intervals around the burst showed correct functionality of the detector. The event rate passing the Muon Filter was used as a stability check, illustrated in Figure 6.3. The event rates of the good run list are shown in green, and the GRB data in red. No deviations were found for rejecting a GRB from this plot. All the GRBs without information on the duration of the burst were rejected, and one GRB was rejected because its position was determined with an angular resolution of 116 degrees. In total 117 GRBs were used in Kevin Meaghers analysis, and the same list is used as a starting point for the presented analysis.

6.1 Data-rate stability checks

To test the data-rate stability for each GRB, checks are made on the number of events during the two-hour window. Figure 6.1 gives an overview of the data-rate checks performed. The median number of entries per 60 second bin is plotted per GRB, as well as the spread of the number of entries per bin for each GRB. Dividing the spread by the median gives a good indication of the stability of the data, as well as the total number of events in the two-hour window [24]. Due to these data-rate stability checks, three GRBs were rejected. During the two-hour window of GRB090206A test runs were taken, and therefore cannot be used in this analysis. For the GRB090107A and GRB090126A, large data gaps arose due to problems that occurred during change of data runs, see section 6.1.2. These GRBs ended with very small entries and a large spread/median of

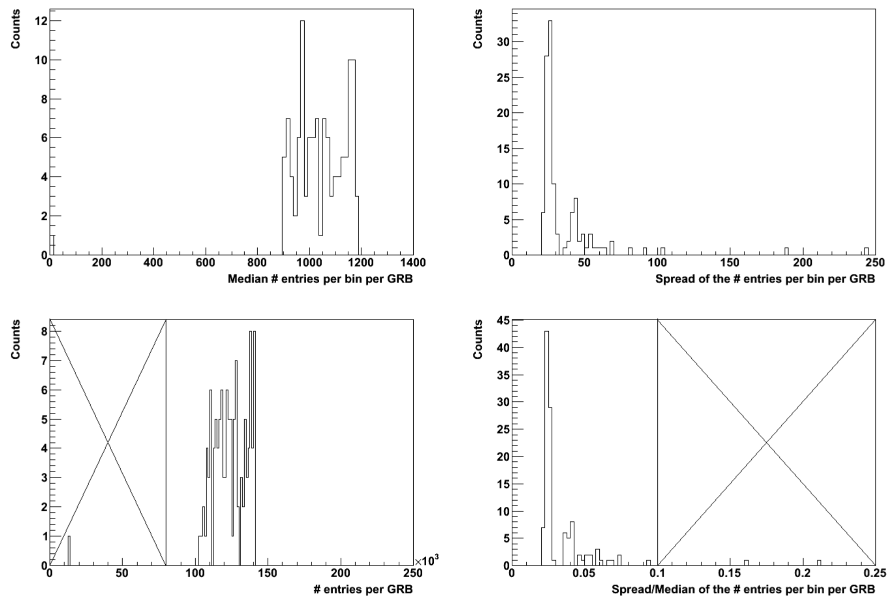

Figure 6.1: Data rate stability checks for all GRBs from [87], three GRBs are rejected due to these checks, which is illustrated by the crossed section in the figures. Further details can be found in the text.

the number of entries per bin, illustrated by the crosses in Figures 6.1 and 6.1.

6.1.1 Angular resolution on the GRB position

The GRBs used in this analysis were originally detected by the satellites from the GCN. These satellites have very different detection methods (see section 2.1), which lead to a substantial difference in the angular resolution of the position of each GRB (see Figure 6.2). In the analysis, the final opening angle that is taken around each GRB is given by

$$\alpha = \sqrt{\alpha^2_{optimal\ opening\ angle} + \sigma^2_{GRB\ position}}, \tag{6.1}$$

depending on the optimal opening angle ($\alpha_{optimal\ opening\ angle} = 6.5°$, see section 4.6.2), and on the resolution of the GRB position($\sigma_{GRB\ position}$). A wider opening angle would enhance the background rate, so all GRBs with a position resolution worse than 6.5 degrees are not taken into account for the analysis. In total 12 GRBs are rejected due to this resolution conditions, namely GRB080818B, GRB081003C, GRB081102B, GRB081105B, GRB081119A, GRB081204B, GRB081229A, GRB090109A, GRB090320B, GRB- 090328B, GRB090409A and GRB090511A.

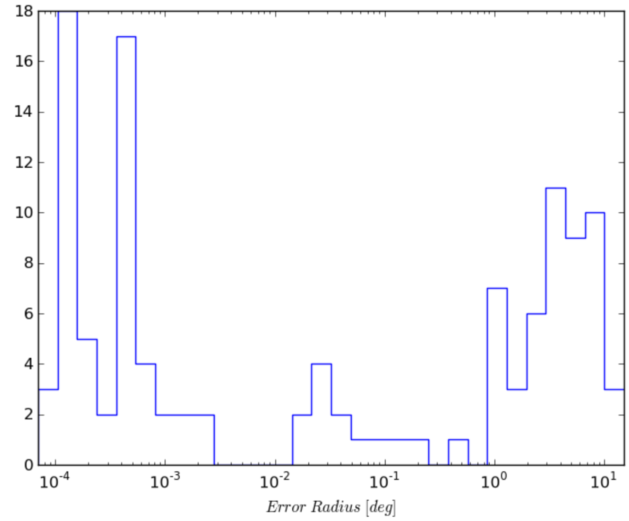

Figure 6.2: Angular resolution of all the GRBs in the GRB list of Kevin Meagher [87]

6.1.2 Nonuniform background rates and Detector Asymmetry

When considering the data of the IceCube IC40 detector, we need to account for two different background fluctuations. First of all, the cosmic ray muon background rate is not uniformly distributed in declination angle over the whole sky. The cosmic rays only travel downwards through the detector. The rate also varies due to seasonal variations. Furthermore, the detector itself has an asymmetric geometry, resulting in variations in the background rates for different azimuth angles. To examine these asymmetries, a large opening angle is used to investigate the specific background rates near the GRB positions. To stay blind in this phase of the analysis, we take a large opening angle of 40° to make sure the signal cannot be seen due to the large amount of background. Only events with a MPE-fit is used, but no further quality checks are performed.

Nonuniform background rates

As Figure 6.3 shows, the amount of total cosmic rays are subjected to seasonal variation. The atmosphere works as a giant calorimeter (see section 1.2). The atmospheric profiles of, for example, temperature, total height and column-density (gram / cm2) vary throughout the year. These variations were investigated for the southern Auger detector based in Argentina to gain understanding of the cosmic ray air showers [94]. It was found that in the summer, the height of the atmosphere and the column-density are increased due to the higher tempera-

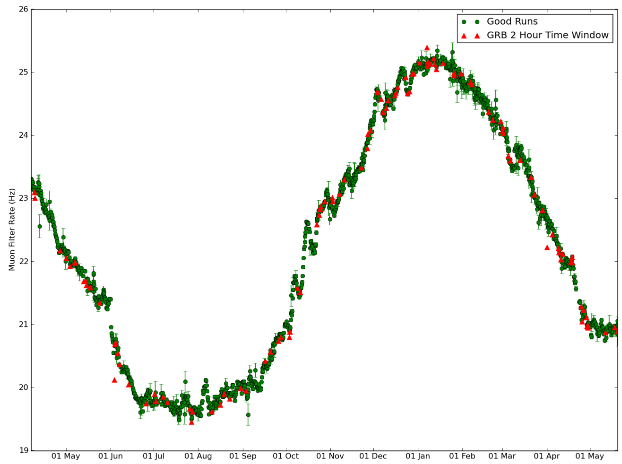

Figure 6.3: Seasonal variation shown using the data rates of the Muon Filter, including the data rates for the two hours surrounding each GRB. (Courtesy of Kevin Meagher [87])

ture. These atmospheric effects are expected to show similar variations at other locations, such as at the South-Pole. Due to an increased column density, the probability that a particle interacts is enlarged, which increases the interaction rate. The cosmic rays will therefore induce more particles in the air showers, resulting in a higher cosmic ray muon rate in the IceCube detector.

Secondly, the cosmic ray muons all have a down-going direction in our detector. To remove most of the background events, only GRBs that lie at least 10° under the horizon, such that they have a position in the Northern Hemisphere sky, are taken into account.

The seasonal variation in background rates is not visible in two-hour time-windows, so the variation will only result in a difference in average background rates between the GRB data-sets. Because the two-hour data-sets are stacked, information on the average background rate for each separate GRB is lost. Thus the seasonal variation will have no influence on the analysis itself.

Detector Asymmetry

The background muon rate also varies in azimuth angle due to the asymmetry of the IC40 detector. Because the IC40 detector is shaped as a boomerang, with a long and short axis, the reconstruction algorithms of the detector perform better for muons passing through the longer axis than through the shorter axis of the detector. Even specific angles show an enhanced reconstruction rate, due to the geometry of the detector. Figure 6.4(a) shows clear preference angles for the

Linefit first guess reconstruction (see section 4.3.1 for a detailed description on the Linefit reconstruction algorithm). For these angles, the DOMs are aligned as is illustrated in Figure 6.4(c). Fortunately the MPE-fit does not have such distinctive preference angles, especially not for tracks with $\theta < 90°$ (upward directed tracks). But the probability that a muon is reconstructed by the MPE algorithm is higher when it travels through the long axis of the detector, than for the shorter axis, see Figure 6.4(b).

To illustrate this effect of detector asymmetry the events per bin for two GRBs is plotted in Figure 6.5. The GRBs were reported on the same day, and have nearly the same declination, 63° and 68° respectively. The different background rate is therefore solely due to the different position of the GRBs with respect to the detector, namely 280° in azimuth for GRB080603A and 175° in azimuth for GRB080603B.

Because of the variation of background rates in azimuth angle, possible differences could show up in the overall event rate in the two hours surrounding a GRB. In addition, the position of the GRB will shift 30° in azimuth with respect to the detector in the two hours of data taking, the background rate could change over time. After investigation of the events per 60 sec bin for each GRB (see Appendix A), no clear deviations are encountered in the two-hour windows. In addition, Figure 6.7 shows that the total stacked bins have no specific deviation in the number of events per bin, where the possible (random) deviations per GRB are eliminated by the stacking procedure.

A second specific feature needs to be addressed, which is illustrated by Figure 6.5. Namely, in the two-hour window of GRB080603A, the data-runs were changed, leaving a gap in the data were no events could be detected and saved on tape, so called detector dead-time. The typical duration of a run is about 8 hours, resulting in about three occurrences of detector dead-time per day. This feature can therefore be seen in numerous two-hour windows (see Appendix A). Fortunately, in most cases these dead-times do not last long, and are always randomly distributed in the two hours. Again, due to the stacked data, these features will not influence this analysis.

Perhaps superfluous, but when one of these asymmetries or other background fluctuation feature would have shown up in the stacked time profile, the analysis method would have been able to cope with it. If the events would not be uniformly distributed over the two hours because of background fluctuations, the effect could have been tackled by incorporating a non-uniform probability p_i (see section 5.2).

An overview of the total events passing the large opening angle filter for each GRB is given in Appendix A, where asymmetry effects for each GRB are visible.

6.1.3 Using the time difference between events as a stability check

A further stability check on the data is performed by looking at the time difference between consecutive events. The background events consist predominantly

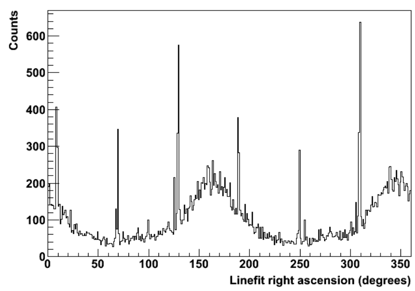

(a)

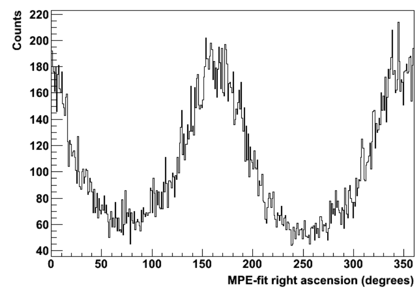

(b)

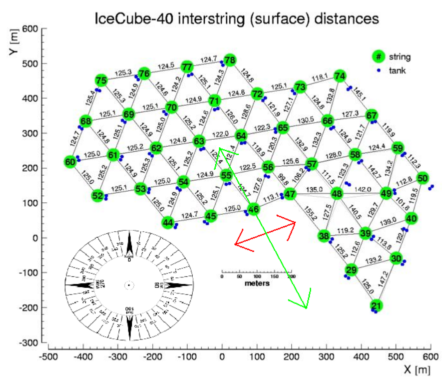

(c)

Figure 6.4: Due to the geometry of the detector, the track reconstructions have specific preference angles. (a) Shows the distribution in azimuth for all reconstructed Linefit first guess tracks. Spikes are visible for the preference angles, where the reconstruction of the muons are better preformed than for other angles. This is due to the line-up of DOMs for those angles. (b) Illustrates the azimuth distribution of MPE-fit reconstructions. The specific preference angles as seen in (a) disappear, but still more MPE-fit tracks are reconstructed along the directions of the arrows, drawn in (c). Figure (c) gives the boomerang geometry of the IC40 detector with specific preference angles for reconstruction algorithms, drawn by the arrows.

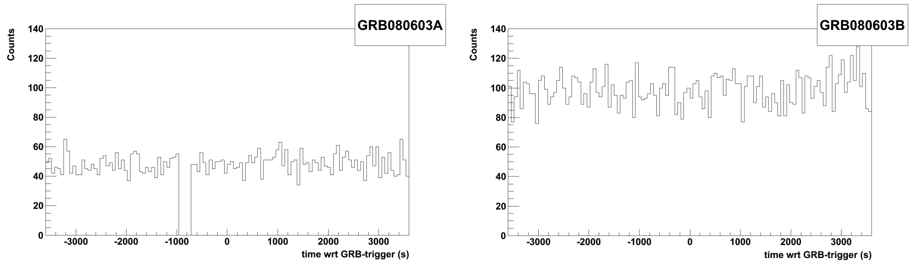

(a) (b)

Figure 6.5: For the two hours surrounding the GRB trigger-time, all events within a 40° opening angle are binned in 60 sec bins for two GRBs. A difference in background rate is visible due to the asymmetric geometry of the IC40 detector. Further details can be found in the text.

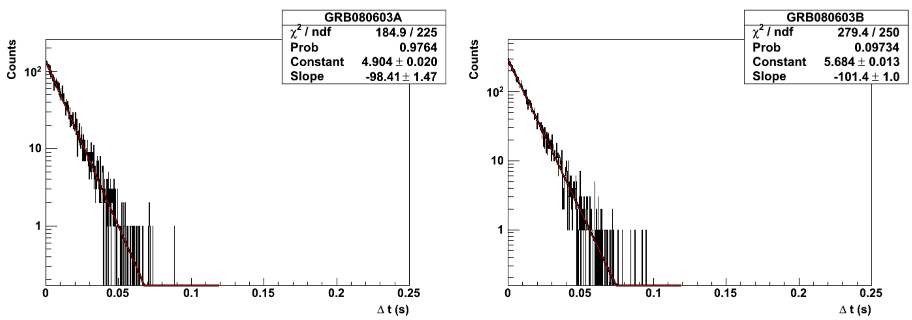

(a) (b)

Figure 6.6: The time difference between consecutive events is plotted. The event rate is a Poission process and exhibits a straight line on log-scale.

of cosmic rays, which have a steady rate. Thus the time difference between consecutive events is given by a Poisson distribution. However, the data passes through several filtering stages, which influences the ratio of cosmic ray background events and other background phenomena, like atmospheric neutrinos. These atmospheric neutrinos have a different rate (and corresponding Poisson distribution). The event rate of the filtered data will therefore not follow one Poisson distribution, but a merger of several Poisson distributions. The Δ t plots are therefore merely a check on the consistency of the data-rate, and will not be used for further analysis. Figure 6.6 shows the time difference between all consecutive events for the two GRBs discussed earlier. The events are primarily background events that can be described by a Poission process and therefore the log-scale exhibits a straight line. An overview on the time difference for all GRBs is given in Appendix B.

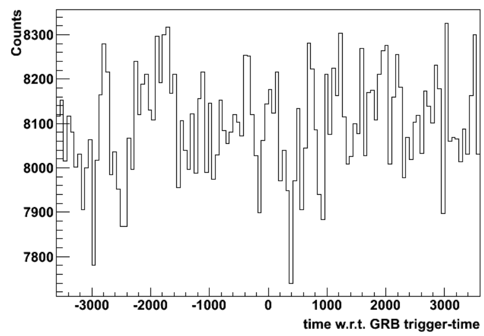

(a)

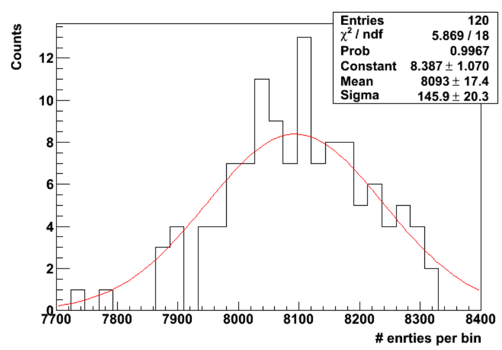

(b)

Figure 6.7: Figure (a) shows the total stacked entries per (60 sec) bins, stacking all GRB time windows of the GRB catalog (see section 6.2). The GRB time windows are stacked such that the GRB trigger-times fall in the center bin (0 seconds). For each GRB, all events with a MPE-fit which point within an opening angle of 40° wrt the GRB position, are taken into account. By using a large opening angle, the analysis stays blind for the low expected neutrino signal from GRBs. The total stacked bins show a uniform distribution, which illustrate the fact that the asymmetry features per GRB are eliminated. Figure (b) gives the distribution of the event rate in the 60 sec bins of Figure (a). A Gaussian is fitted to illustrate that the entries per bin is consistent with a pure background distribution. Further details can be found in the text.

6.1.4 Stacked GRBs window

After stacking all the events passing the large opening angle filter (40°), all the irregularities due to the asymmetry or dead-time of the detector disappear, see Figure 6.7. The stacking procedure ensures that specific features, which are seen per GRB separately, are eliminated. The number of entries is uniformly distributed over the two-hour window, which is compatible with a background distribution. The large number of entries per bin can be fitted by a Gaussian function. It is noted that from this histogram no signal can be seen because of the high background rate.

6.2 GRB Catalog

Finally, 102 GRBs passed the data consistency checks and are used in this analysis. An overview of all GRBs in the catalog is given here.

Table 6.1: IcePack Feature Extractor Parameters

Name	Satellite	Date	T_0	RA [°]	Dec [°]	σ_{pos} [°,′,″]	Fluence [$10^{-6}\frac{erg}{cm^2}$]
GRB080408A	SuperAGILE	08/04/2008	18:12:48	114.665	33.304	0.50”	
GRB080409A	BAT	09/04/2008	01:22:57	84.330	5.085	2.00”	0.61
GRB080426A	BAT	26/04/2008	13:23:22	26.499	69.468	1.80”	0.37
GRB080430A	BAT	30/04/2008	19:53:02	165.311	51.686	0.50”	1.2
GRB080503A	BAT	03/05/2008	12:26:13	286.620	68.794	0.25”	2
GRB080506A	BAT	06/05/2008	17:46:21	329.424	38.985	0.50”	1.3
GRB080507A	SuperAGILE	07/05/2008	07:45:00	233.681	56.436	0.70”	50.9
GRB080513A	IPN	13/05/2008	05:14:32	163.283	28.195	10.98’	20.2
GRB080514B	SuperAGILE	14/05/2008	09:55:56	322.845	0.708	0.60”	32.3
GRB080515A	BAT	15/05/2008	06:01:13	3.163	32.579	3.80”	2
GRB080517A	BAT	17/05/2008	21:22:51	102.242	50.735	1.80”	0.56
GRB080524A	BAT	24/05/2008	04:13:00	268.449	80.143	2.50’	0.29
GRB080603A	INTEGRAL	03/06/2008	11:18:11	279.409	62.744	0.30”	10
GRB080603B	BAT	03/06/2008	19:38:13	176.532	68.061	0.30”	4.5
GRB080604A	BAT	04/06/2008	07:27:01	236.965	20.558	0.50”	0.8
GRB080605A	BAT	05/06/2008	23:47:57	262.125	4.016	0.50”	30.2
GRB080607A	BAT	07/06/2008	06:07:27	194.947	15.920	0.50”	89.3
GRB080613A	INTEGRAL	13/06/2008	09:35:21	213.271	5.173	0.50”	1.3
GRB080625A	SuperAGILE	25/06/2008	12:28:31	298.404	56.278	0.50”	2.3
GRB080701A	BAT	01/07/2008	10:13:37	45.839	75.475	1.70”	0.72
GRB080702A	BAT	02/07/2008	11:50:43	313.051	72.313	1.90”	0.036
GRB080707A	BAT	07/07/2008	08:27:53	32.618	33.110	1.10”	0.52
GRB080710A	BAT	10/07/2008	07:13:10	8.274	19.501	0.50”	1.4
GRB080726A	SuperAGILE	26/07/2008	01:26:10	20.398	13.913	5.00’	

Name	Satellite	Date	T_0	RA [°]	Dec [°]	σ_{pos} [°,′,″]	Fluence $[10^{-6}\,\frac{erg}{cm^2}]$
GRB080727B	BAT	27/07/2008	08:13:24	276.859	1.163	1.90”	9.46
GRB080727C	BAT	27/07/2008	23:07:35	32.635	64.138	1.50”	5.2
GRB080810A	BAT	10/08/2008	13:10:12	356.793	0.320	0.60”	6.9
GRB080816A	GBM	16/08/2008	12:04:18	156.200	42.600	2.00°	18.6
GRB080822B	BAT	22/08/2008	21:02:52	63.560	25.760	3.60’	0.17
GRB080830A	GBM	30/08/2008	08:50:16	160.100	30.800	2.50°	4.6
GRB080903A	BAT	03/09/2008	01:12:23	86.792	51.264	1.60”	1.4
GRB080916B	BAT	16/09/2008	14:44:47	163.665	69.065	5.10”	0.63
GRB080920A	GBM	20/09/2008	06:25:48	121.600	8.900	5.40°	2.4
GRB080925A	GBM	25/09/2008	18:35:55	96.100	18.200	1.20°	9.7
GRB080927A	GBM	27/09/2008	11:30:32	61.300	27.400	4.60°	5.7
GRB081003A	INTEGRAL	03/10/2008	13:46:12	262.391	16.571	3.90”	0.4
GRB081003B	INTEGRAL	03/10/2008	20:48:08	285.026	16.691	1.50’	6
GRB081009A	GBM	09/10/2008	03:20:58	250.500	18.400	1.00°	35
GRB081011A	BAT	11/10/2008	00:28:50	220.344	33.544	0.50”	0.16
GRB081022A	BAT	22/10/2008	14:23:48	226.584	12.409	1.40’	2.5
GRB081024A	BAT	24/10/2008	05:53:08	27.874	61.331	1.90”	0.12
GRB081024B	GBM	24/10/2008	21:22:41	322.900	21.204	9.60’	0.27
GRB081025A	BATSS	25/10/2008	08:22:02	245.366	60.474	6.70”	7.1
GRB081028A	BAT	28/10/2008	00:25:00	121.895	2.308	1.50”	3.7
GRB081102A	BAT	02/11/2008	17:44:39	331.172	52.994	1.50”	2.1
GRB081107A	GBM	07/11/2008	07:42:01	51.000	17.100	3.50°	1.64
GRB081110A	GBM	10/11/2008	14:25:43	111.700	21.400	1.80°	
GRB081122A	GBM	22/11/2008	12:28:12	339.100	40.000	1.00°	9.6
GRB081126A	BAT	26/11/2008	21:34:10	323.515	48.711	0.50”	9.91
GRB081127A	BAT	27/11/2008	07:05:08	332.064	6.851	1.70”	0.49
GRB081128A	BAT	28/11/2008	17:18:44	20.804	38.127	1.80”	2.3
GRB081203A	BAT	03/12/2008	13:57:11	233.032	63.521	0.50”	30.5
GRB081203B	BATSS	03/12/2008	13:52:02	228.799	44.429	0.50”	55.6
GRB081206A	GBM	06/12/2008	06:35:53	120.100	32.800	6.40°	4
GRB081207A	GBM	07/12/2008	16:18:47	112.400	70.500	1.20°	106
GRB081209A	GBM	09/12/2008	23:31:56	45.300	63.500	4.90°	0.59
GRB081211B	BATSS	11/12/2008	06:15:02	168.265	53.830	2.00”	0.61
GRB081215A	GBM	15/12/2008	18:48:37	125.600	54.000	1.00°	3.54
GRB081216A	IPN	16/12/2008	12:44:00	129.200	7.600	4.40°	3.6
GRB081217A	GBM	17/12/2008	23:34:49	116.800	26.800	2.00°	10

Name	Satellite	Date	T_0	RA [°]	Dec [°]	σ_{pos} [°, ′, ″]	Fluence [$10^{-6}\frac{erg}{cm^2}$]
GRB081223A	GBM	23/12/2008	10:03:57	112.500	33.200	3.80°	1.2
GRB081224A	GBM	24/12/2008	21:17:55	201.700	75.100	1.00°	2.87
GRB081226C	GBM	26/12/2008	03:44:52	193.000	26.800	2.40°	2.32
GRB081228A	BAT	28/12/2008	01:17:40	39.462	30.853	2.90”	0.089
GRB090102A	BAT	02/01/2009	02:55:45	128.244	33.114	1.10”	30.9
GRB090107B	INTEGRAL	07/01/2009	16:20:36	284.818	59.595	1.80”	1.75
GRB090108A	GBM	08/01/2009	00:29:02	260.800	46.000	3.80°	1.28
GRB090111A	BAT	11/01/2009	23:58:21	251.676	0.077	1.70”	0.62
GRB090112B	GBM	12/01/2009	17:30:15	192.300	25.400	1.70°	5.4
GRB090113A	BAT	13/01/2009	18:40:39	32.057	33.429	1.70”	0.76
GRB090118A	BATSS	18/01/2009	13:54:02	49.828	18.415	7.10”	0.4
GRB090126B	GBM	26/01/2009	05:26:22	189.200	34.100	3.60°	1.25
GRB090131A	GBM	31/01/2009	02:09:21	352.300	21.200	1.00°	22.3
GRB090207A	GBM	07/02/2009	18:39:10	252.700	34.900	3.80°	4.01
GRB090219A	GBM	19/02/2009	01:46:18	26.500	59.200	5.20°	0.8
GRB090222A	GBM	22/02/2009	04:17:09	118.600	45.000	4.30°	2.19
GRB090227B	GBM	27/02/2009	18:31:01	11.800	32.200	1.80°	8.7
GRB090228B	GBM	28/02/2009	23:25:01	357.600	36.700	3.30°	0.996
GRB090301A	BAT	01/03/2009	06:55:55	338.142	26.639	1.00’	113
GRB090301B	GBM	01/03/2009	07:33:37	352.800	9.500	5.00°	2.69
GRB090305B	GBM	05/03/2009	01:14:35	135.000	74.300	5.40°	2.7
GRB090306C	GBM	06/03/2009	05:52:05	137.000	57.000	4.10°	0.9
GRB090313A	BAT	13/03/2009	09:06:27	198.401	8.097	0.50”	1.4
GRB090323A	LAT	23/03/2009	00:02:42	190.710	17.053	0.50”	100
GRB090401A	BAT	01/04/2009	00:00:59	350.920	29.762	1.00’	21.4
GRB090404A	BAT	04/04/2009	15:56:30	239.240	35.516	1.80”	3
GRB090408B	IPN	08/04/2009	19:46:38	43.980	26.610	29.39’	284
GRB090410A	BAT	10/04/2009	16:57:52	334.956	15.419	1.80’	5.6
GRB090411B	GBM	11/04/2009	23:47:44	38.500	5.100	2.40°	8
GRB090417B	BAT	17/04/2009	15:20:03	209.693	47.017	5.00”	2.3
GRB090418A	BAT	18/04/2009	11:07:40	269.313	33.406	0.50”	17.9
GRB090418B	BATSS	18/04/2009	08:59:02	225.910	17.224	1.91’	23.1
GRB090424A	BAT	24/04/2009	14:12:09	189.521	16.838	0.74”	52
GRB090425A	GBM	25/04/2009	09:03:30	118.600	68.100	2.10°	13
GRB090426A	BAT	26/04/2009	12:48:47	189.075	32.986	0.75”	0.18
GRB090428A	GBM	28/04/2009	10:34:38	210.100	39.500	4.20°	0.99
GRB090428B	GBM	28/04/2009	13:15:11	0.800	11.500	3.90°	5.2
GRB090429B	BAT	29/04/2009	05:30:03	210.667	32.171	0.50”	0.31
GRB090429C	GBM	29/04/2009	12:43:25	260.000	54.300	4.80°	3.7
GRB090429D	GBM	29/04/2009	18:03:57	124.400	7.900	5.00°	1.6
GRB090518A	BAT	18/05/2009	01:54:44	119.954	0.759	1.60”	1.6
GRB090519A	BAT	19/05/2009	21:08:56	142.279	0.180	0.50”	1.2

Chapter 7

Results and Discussion

This report provides a full description on the GRB analysis for the IC 40 detector. Low level feature extraction algorithms, high level parameter cuts, statistical analyses and data performance checks are described. A total number of 102 GRBs were selected, for which two-hour time-windows are investigated for possible neutrino signal. Various filters have been applied to the data, to eliminate as much background events as possible, ensuring not too much signal is filtered out along this process. Finally, "only" 32 events out of the ~ 200 hours of data were selected for the analysis, which lies in perfect agreement with the expected 30 events based on an extrapolation of the study by M.Duvoort [24].

To be able to present the final distribution of these 32 events, and state a concluding $\Psi_{observed}$ or $P - value$ for the observation, a so-called "unblinding" permission has to be granted from the IceCube collaboration. In view of the time in which this Masters degree research had to be performed, such a request for "unblinding" the data could not be achieved.

However, the distribution of the $\Psi_{background}$ can be determined, because this only relies on the number of events. This $\Psi_{background}$ distribution is illustrated by Figure 7.1. For this distribution, the variable time binning was applied, as described in 5.1.1. The 5 σ limit corresponds to a minimum $\Psi_{observed}$ of 123. This $\Psi_{observed}$ value is obtained when at least 8 signal events are detected in the center bin, assuming the remaining 24 background events are distributed uniformly in the two hour time window. This corresponds to an average detection of one neutrino for $\backsim 8$ % of the GRBs, which is in agreement with the expected detection sensitivity of the analysis [89], and can be compared to the largest expected neutrino detection fraction of $\backsim 10$ % predicted [95] [96]. From a theory point of view, an "unblinding" of the analysis could result in a discovery.

In the case the observation would not provide a discovery, an upper-limit can be set to the neutrino flux. This upper-limit constraints the amount of neutrinos emitted by a GRB. To set the limit, a clear understanding is needed of the expected number of neutrinos that can be detected by the detector, including the amount of signal events that are lost due to the parameter cuts

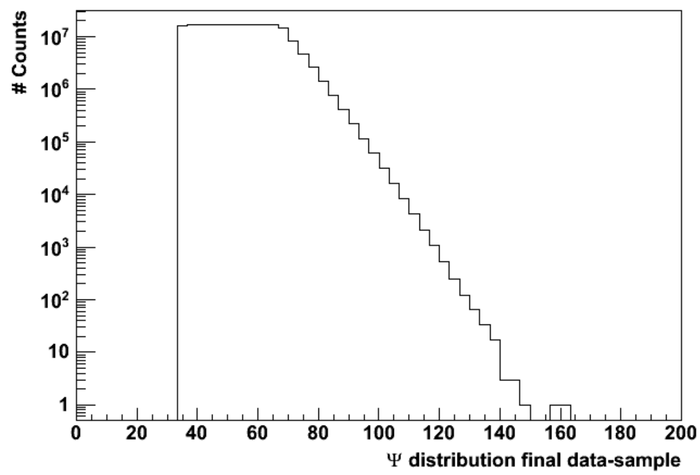

Figure 7.1: Ψ distribution for the final 32 events is illustrated here. The variable bins are used, as described in section 5.1.1.

and filter levels. Also this did not lie in the scope of the research presented. It is noted that the analysis as it is set up, is aimed to make a discovery and not to set an upper-limit.

The IceCube detector will be completed in the construction period of 2010-2011, doubling in size compared to the IC40 detector. The effective area, for which the detector is able to detect the neutrinos will enlarge, which will increase the fraction of observed signal events per GRB. Although the background events will also increase due to the size, the study to improve the track reconstruction algorithms is still ongoing, which would lower the amount of mis-reconstructed tracks in the detector. Eliminating the background events is therefore still an important task. Improvements on the feature extractors and improved hit-cleaning procedures that are described in chapter 4 could help improve the track reconstructions even further.

Concerning the analysis presented here, a general parameter cut procedure has been investigated and used to eliminate as much background events without loosing too much of our signal. The procedure as described here could be improved by the use of more parameters to distinguish the background from the signal events. For example the number of hits per event or the distribution of events in the detector can be used, because they have a different *pdf* for signal compared to background events. Including these different parameters could improve the background elimination procedure, leaving more signal in the final data.

As the detector is coming to its completion, and the data-sets over the years are getting similar, an analysis which spans over multiple years will be more feasible. This would increase the discovery potential of the analysis, as the fraction of observed neutrinos per GRB that is needed to claim a 5σ discovery, decreases when adding more GRBs to the final data-sample [89]. As M.Duvoort showed in his research with multiple years of AMANDA data, our analysis method can easily incorporate different years of data. Provided that the total time-windows per GRB are kept the same, one can stack GRBs data from multiple years onto each other. Even having different parameter cuts for different GRBs will not influence the statistical method, as the background is determined only by randomizing the total number of events. However, these parameter cuts have to be taken carefully into account when providing an upper-limit in case of no discovery.

Also the construction of the DeepCore component in the IceCube detector will open up opportunities, as this will allow the detection of lower energy neutrinos, and also a search for neutrinos from the Southern Hemisphere using veto-algorithms. Including the GRBs from the Southern Hemisphere can double our GRBs in the stacking method.

Appendix A

Histograms of entries per bin for all GRBs

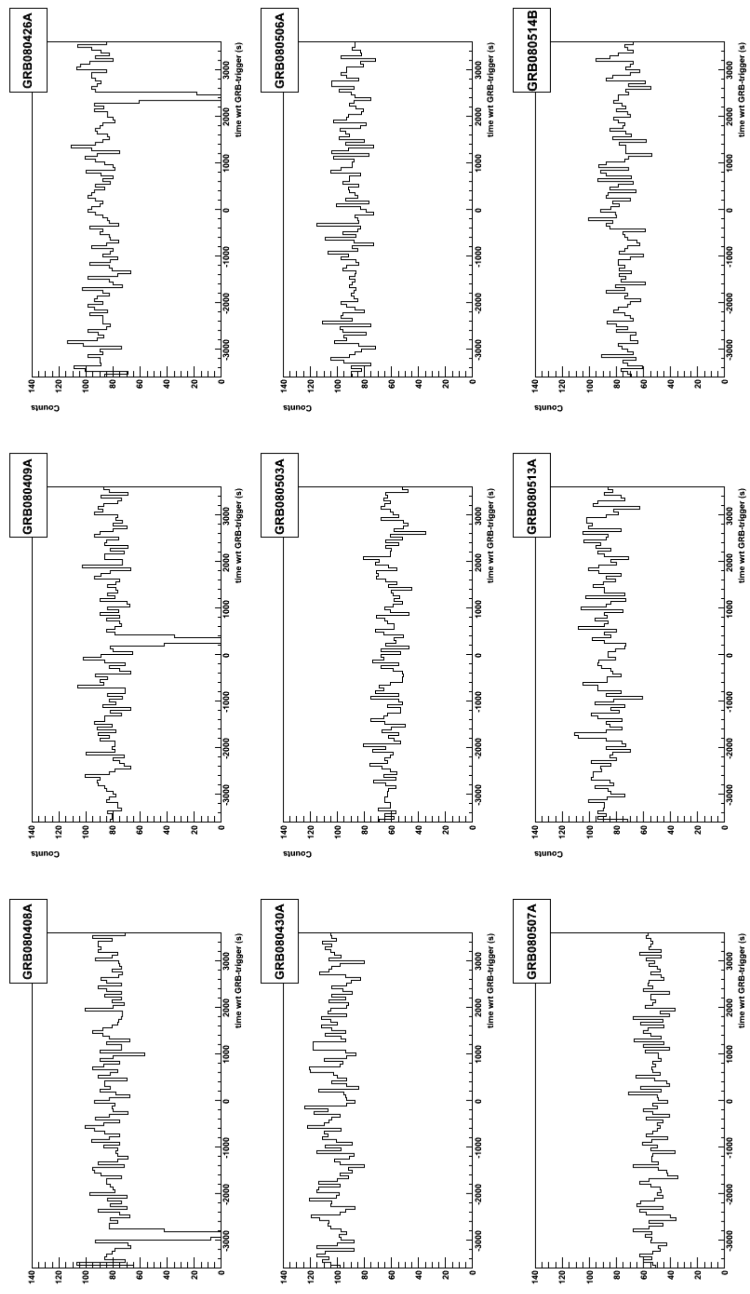

Figure A.1: Number of entries per 60 sec bin during two hours surrounding each GRB trigger. The events are filtered up to level 2 (see section 4.4) and need to lie within a 40° degree opening angle around the GRB position.

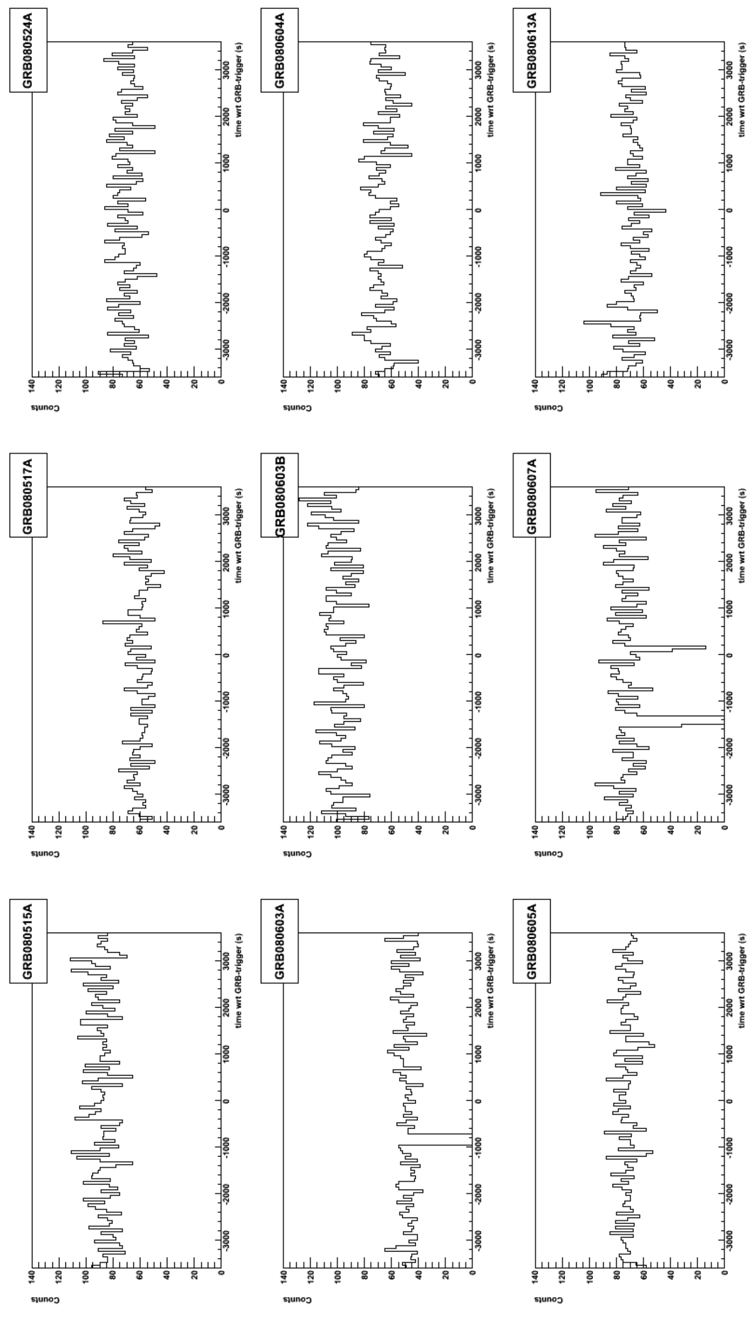

Figure A.2: Number of entries per 60 sec bin during two hours surrounding each GRB trigger. The events are filtered up to level 2 (see section 4.4) and need to lie within a 40° degree opening angle around the GRB position.

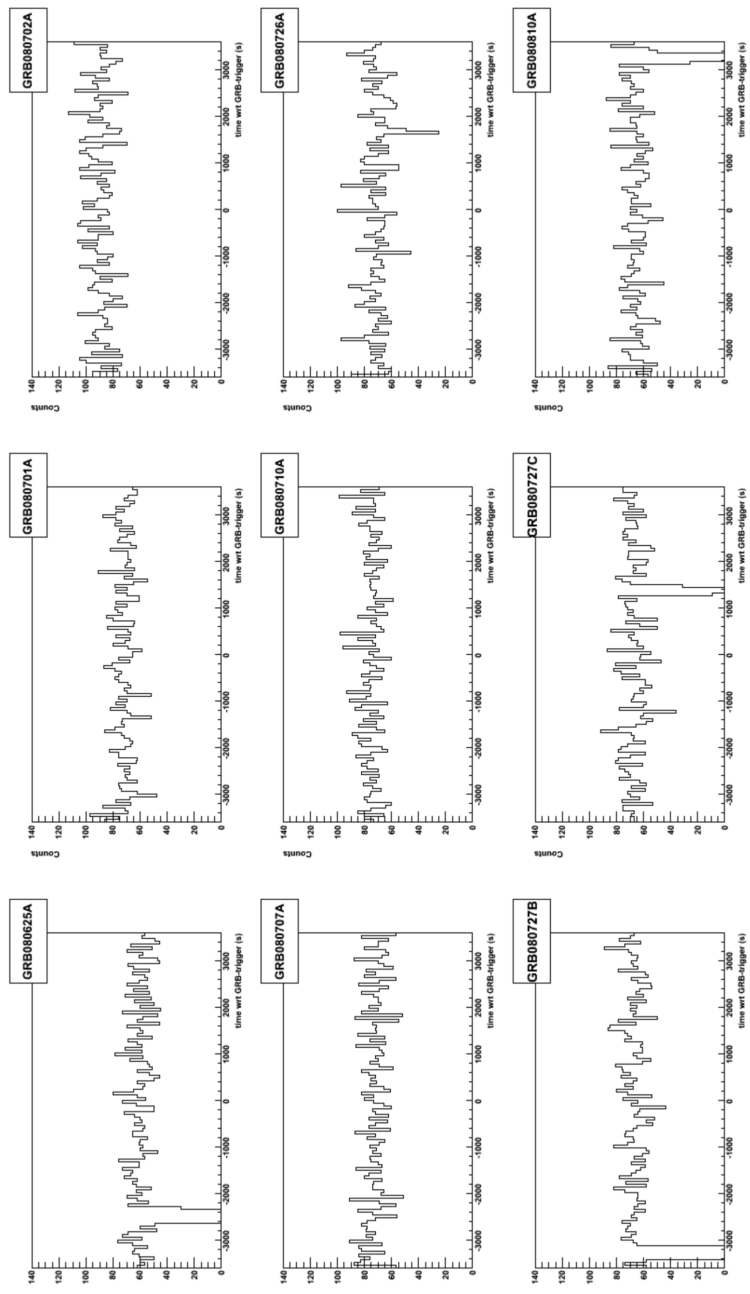

Figure A.3: Number of entries per 60 sec bin during two hours surrounding each GRB trigger. The events are filtered up to level 2 (see section 4.4) and need to lie within a 40° degree opening angle around the GRB position.

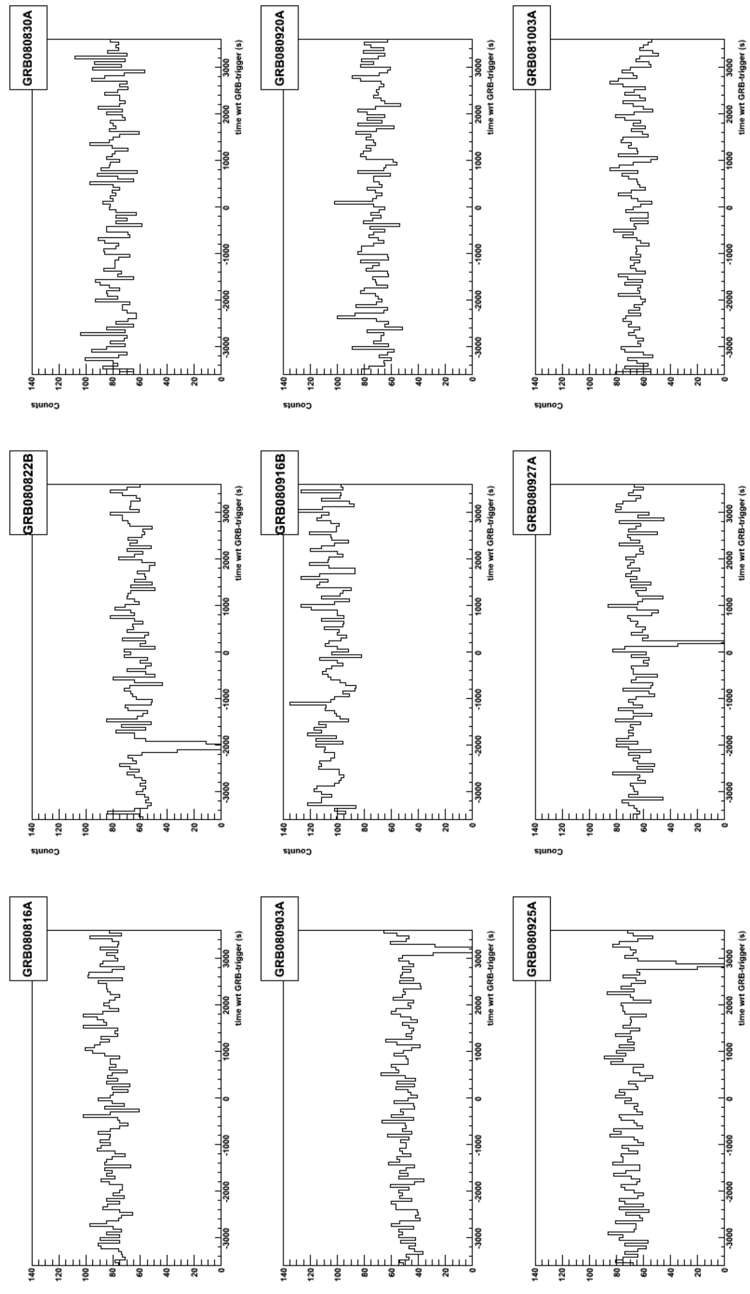

Figure A.4: Number of entries per 60 sec bin during two hours surrounding each GRB trigger. The events are filtered up to level 2 (see section 4.4) and need to lie within a 40° degree opening angle around the GRB position.

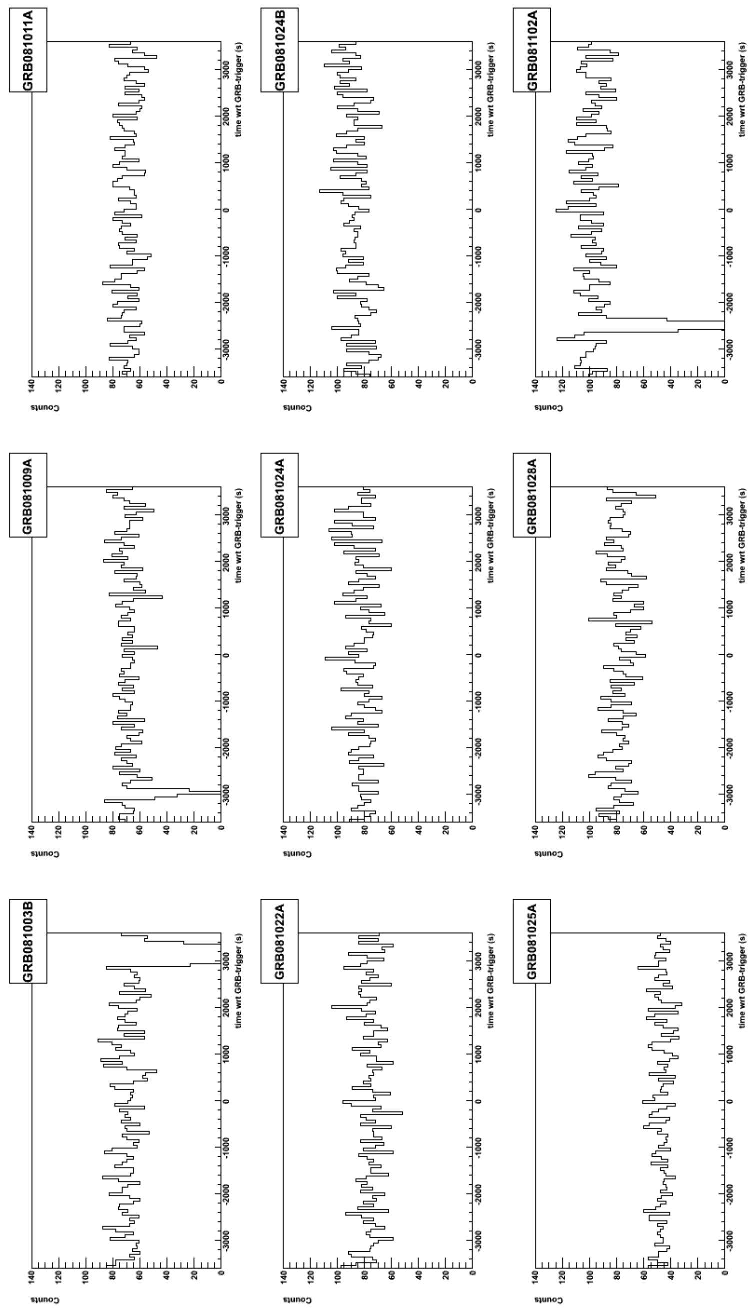

Figure A.5: Number of entries per 60 sec bin during two hours surrounding each GRB trigger. The events are filtered up to level 2 (see section 4.4) and need to lie within a 40° degree opening angle around the GRB position.

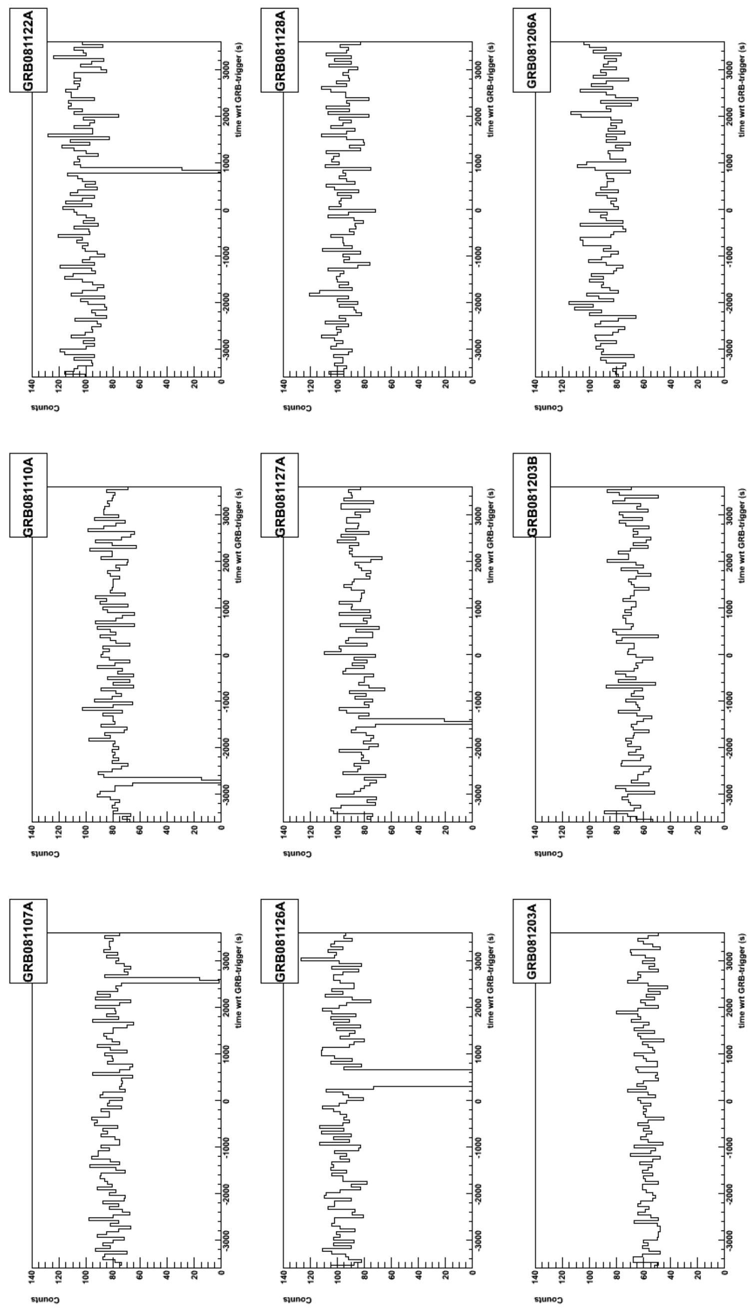

Figure A.6: Number of entries per 60 sec bin during two hours surrounding each GRB trigger. The events are filtered up to level 2 (see section 4.4) and need to lie within a 40° degree opening angle around the GRB position.

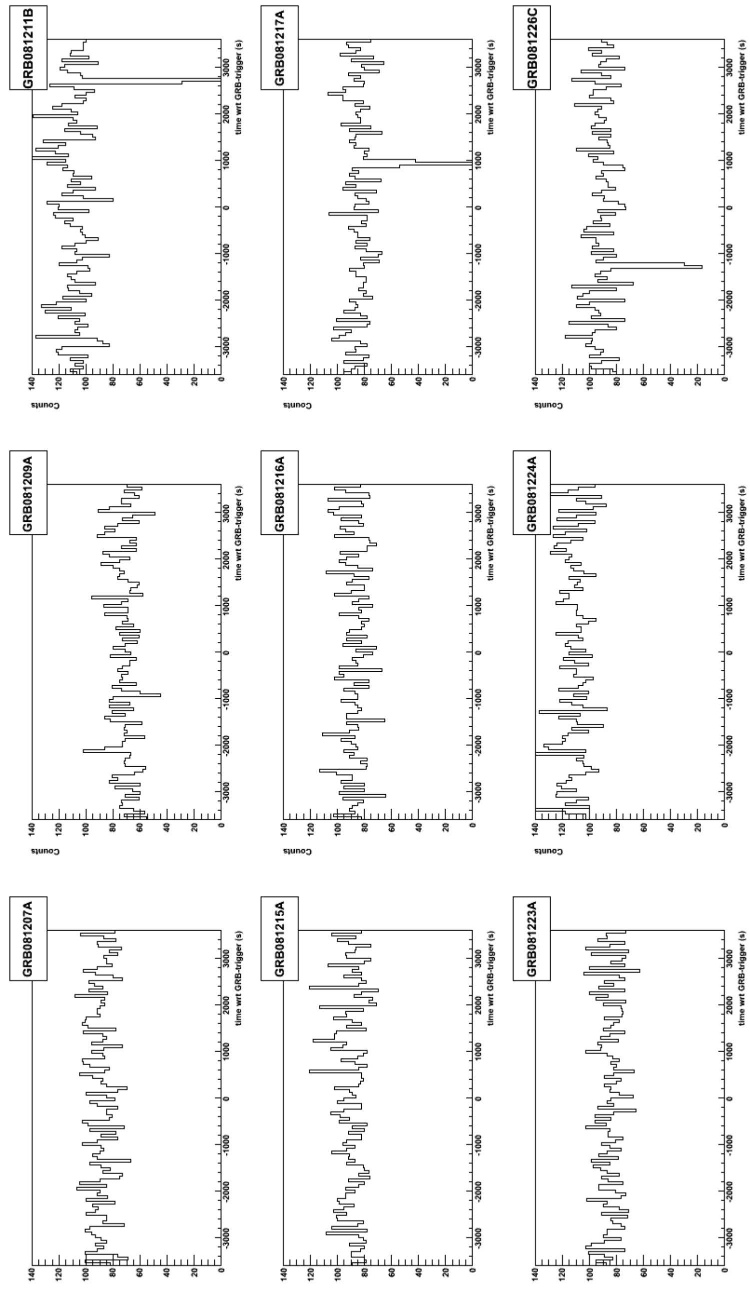

Figure A.7: Number of entries per 60 sec bin during two hours surrounding each GRB trigger. The events are filtered up to level 2 (see section 4.4) and need to lie within a 40° degree opening angle around the GRB position.

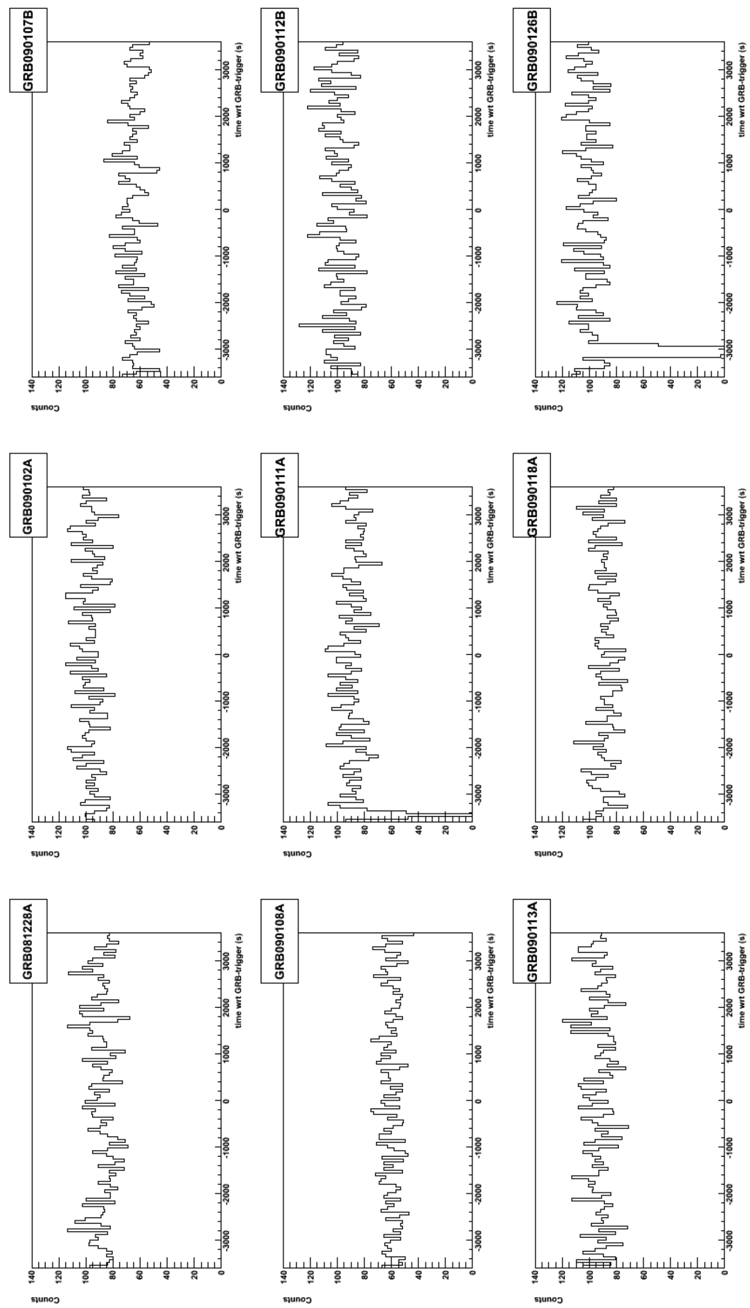

Figure A.8: Number of entries per 60 sec bin during two hours surrounding each GRB trigger. The events are filtered up to level 2 (see section 4.4) and need to lie within a 40° degree opening angle around the GRB position.

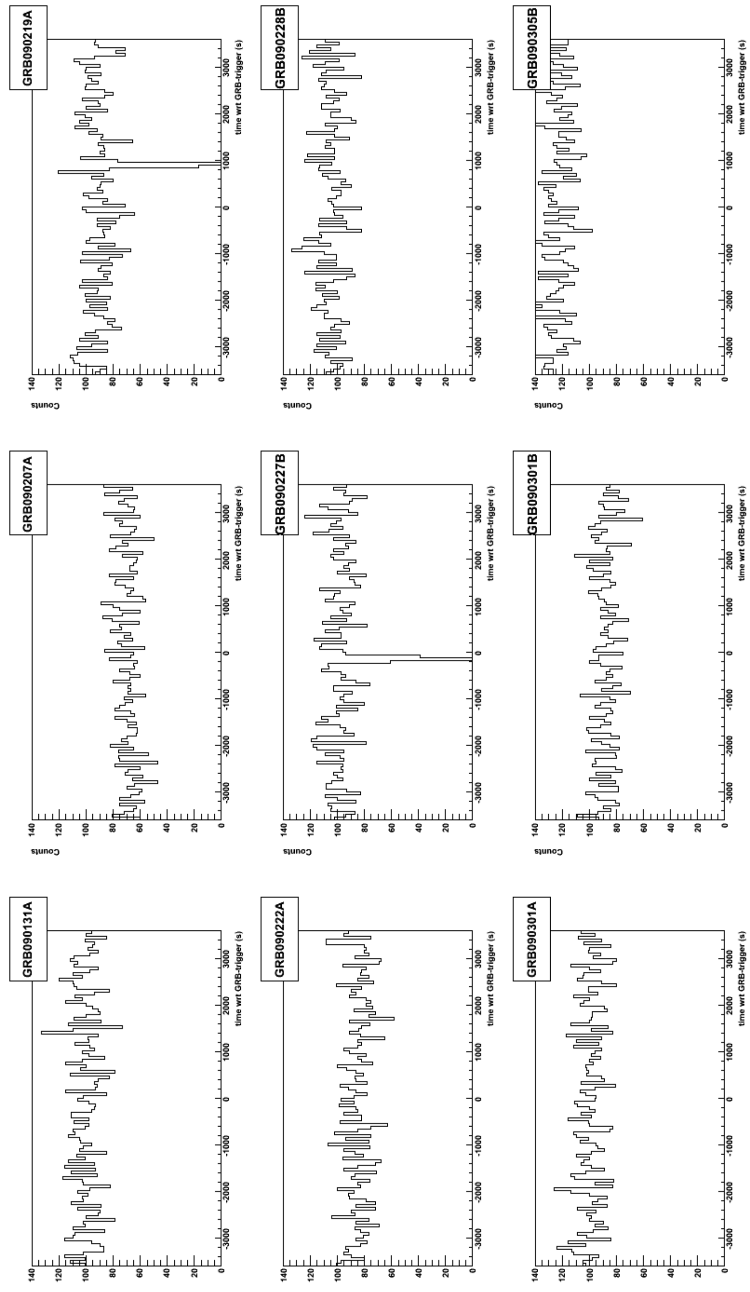

Figure A.9: Number of entries per 60 sec bin during two hours surrounding each GRB trigger. The events are filtered up to level 2 (see section 4.4) and need to lie within a 40° degree opening angle around the GRB position.

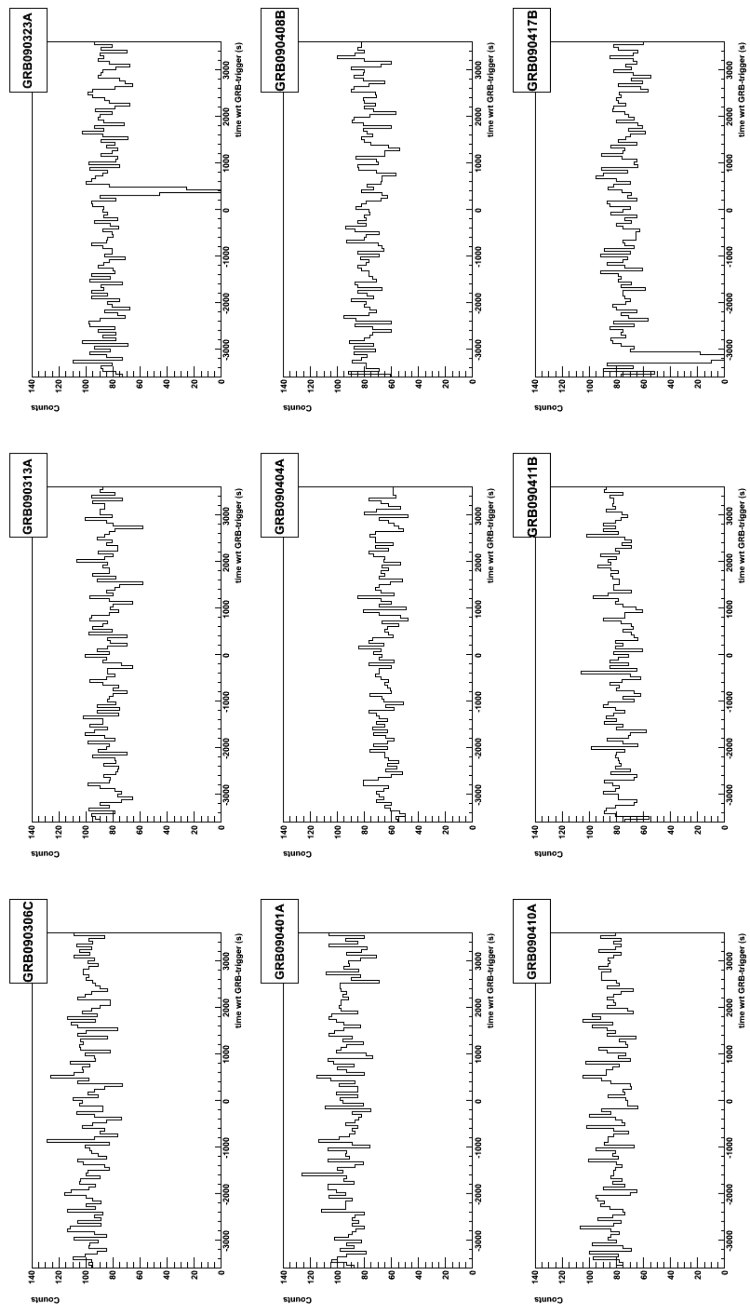

Figure A.10: Number of entries per 60 sec bin during two hours surrounding each GRB trigger. The events are filtered up to level 2 (see section 4.4) and need to lie within a 40° degree opening angle around the GRB position.

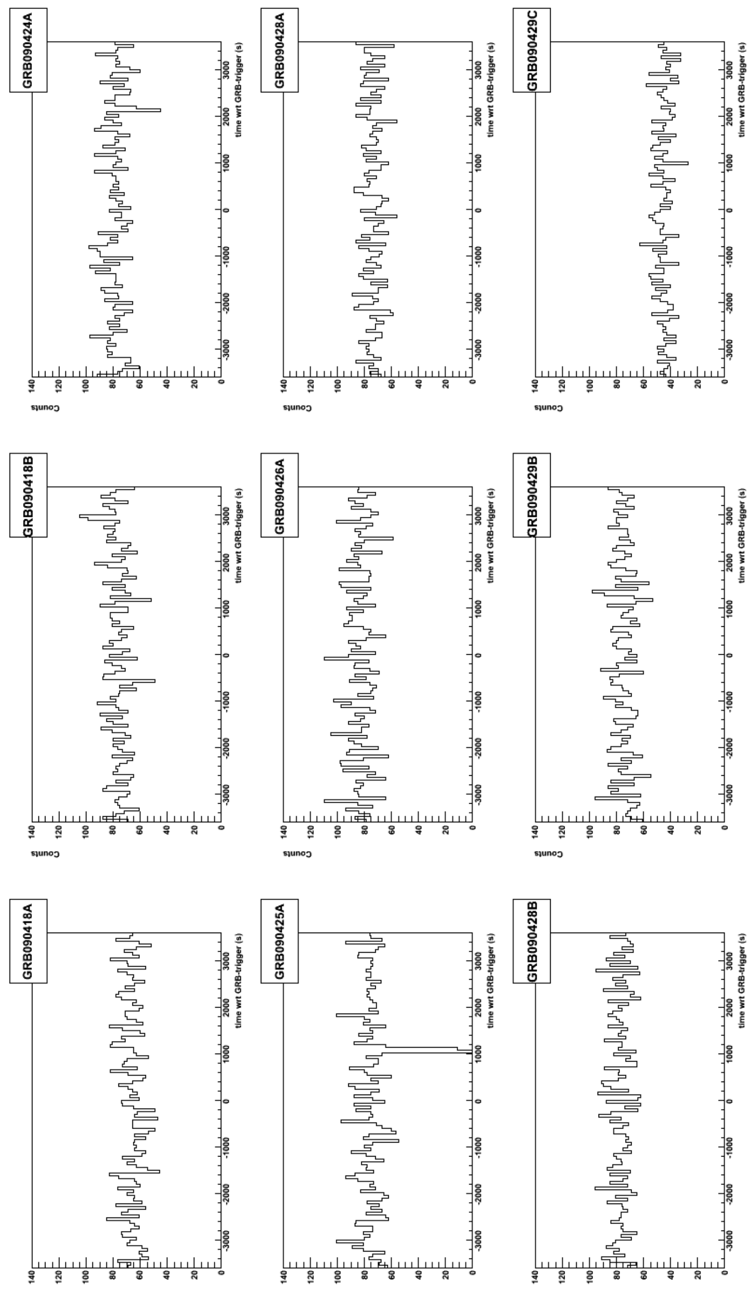

Figure A.11: Number of entries per 60 sec bin during two hours surrounding each GRB trigger. The events are filtered up to level 2 (see section 4.4) and need to lie within a 40° degree opening angle around the GRB position.

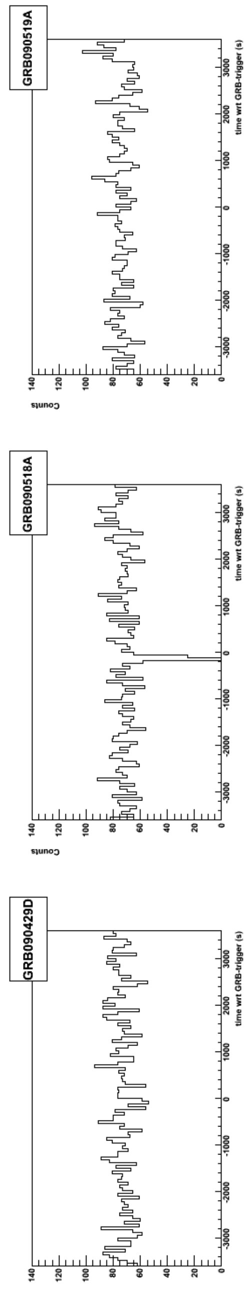

Figure A.12: Number of entries per 60 sec bin during two hours surrounding each GRB trigger. The events are filtered up to level 2 (see section 4.4) and need to lie within a 40° degree opening angle around the GRB position.

Appendix B

Δt of consecutive events plots for all GRBs

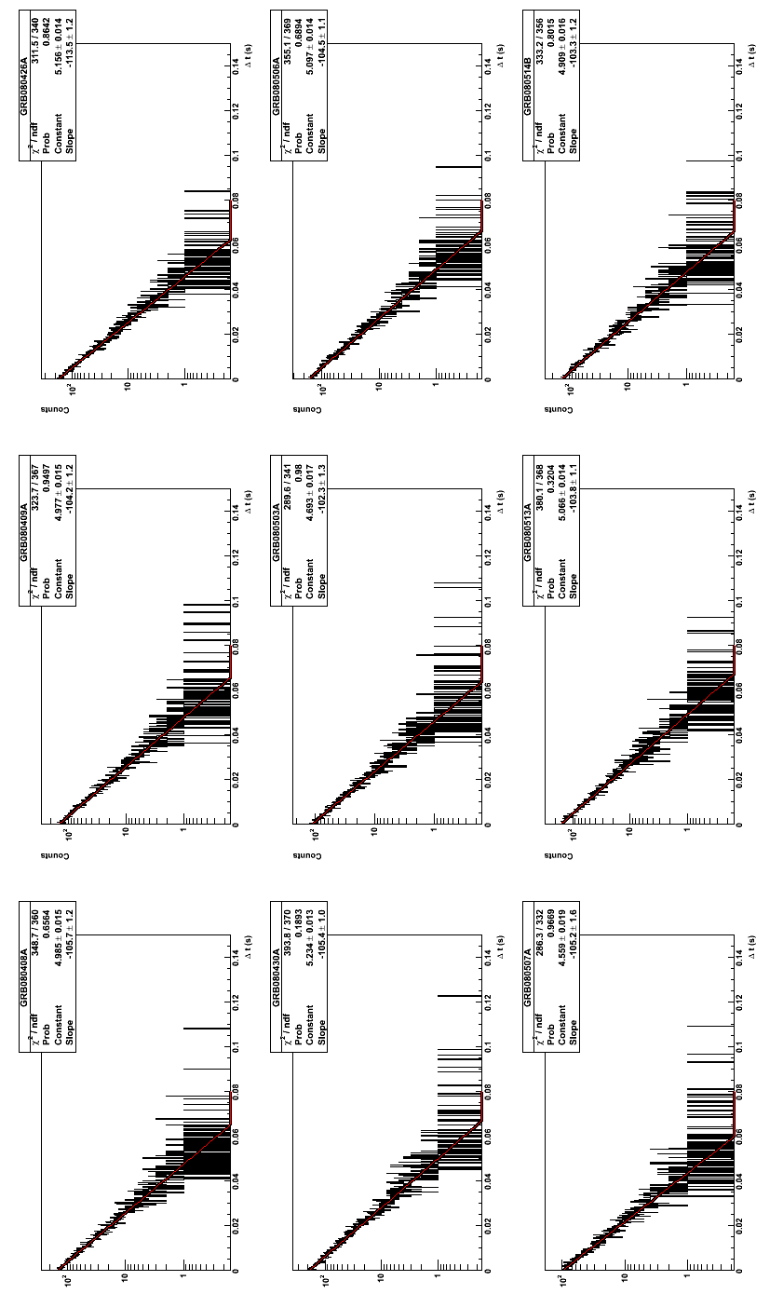

Figure B.1: The difference in time between consecutive events is plotted. The events are filtered up to level 2 (see sectionsec:Filter) and need to lie within a 40° degree opening angle around the GRB position.

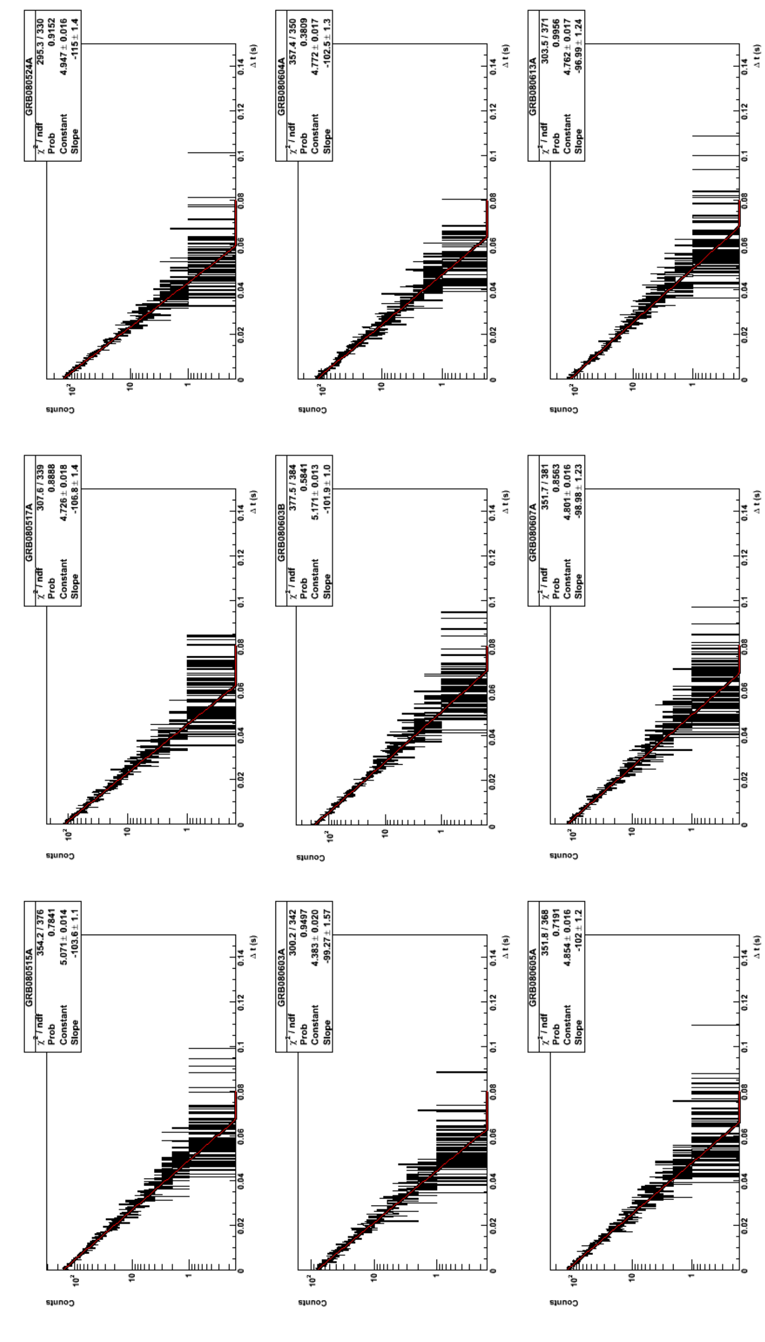

Figure B.2: The difference in time between consecutive events is plotted. The events are filtered up to level 2 (see sectionsec:Filter) and need to lie within a 40° degree opening angle around the GRB position.

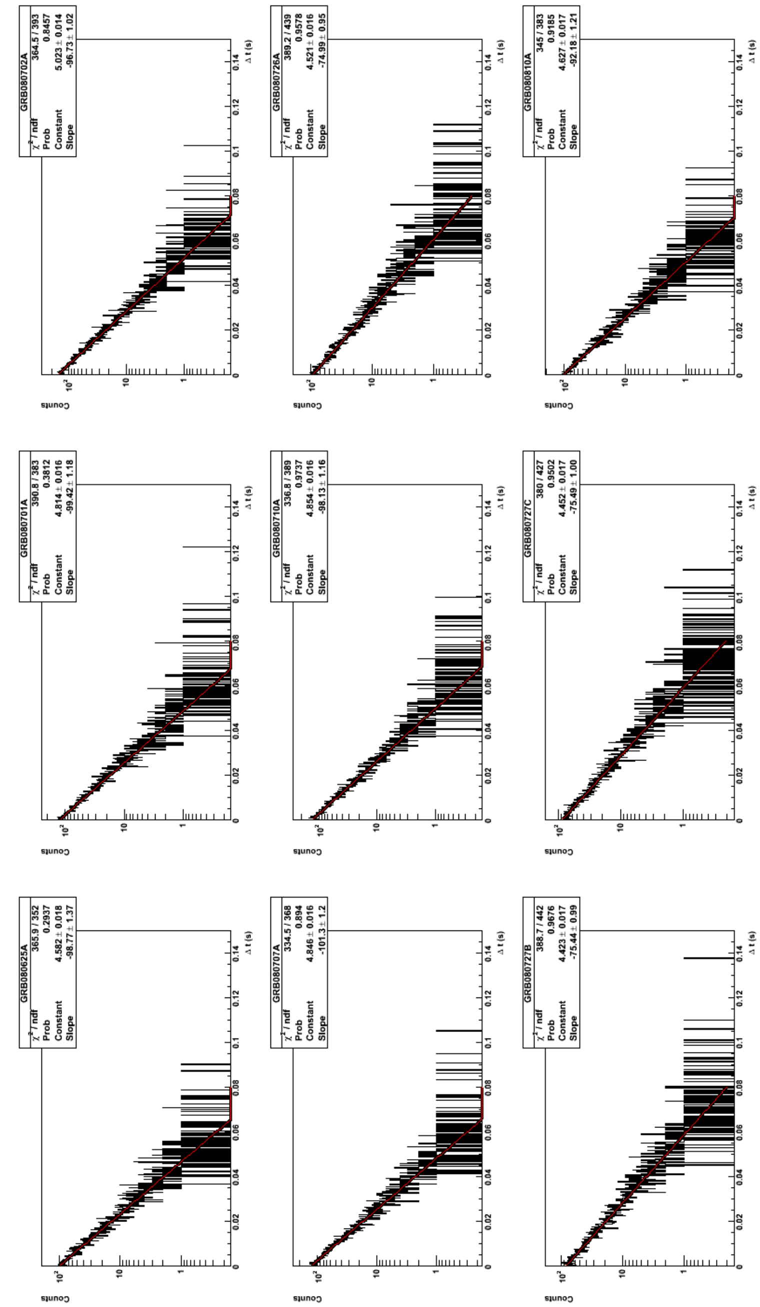

Figure B.3: The difference in time between consecutive events is plotted. The events are filtered up to level 2 (see sectionsec:Filter) and need to lie within a 40° degree opening angle around the GRB position.

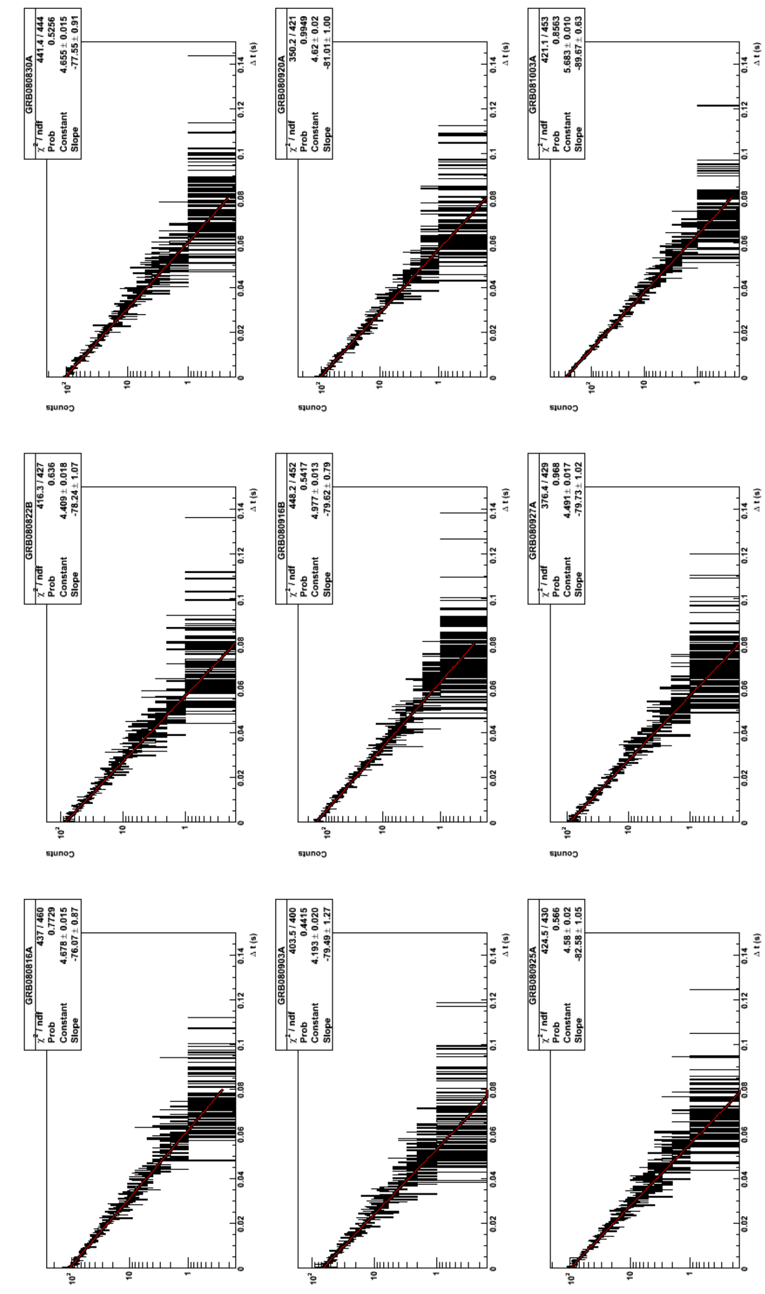

Figure B.4: The difference in time between consecutive events is plotted. The events are filtered up to level 2 (see sectionsec:Filter) and need to lie within a 40° degree opening angle around the GRB position.

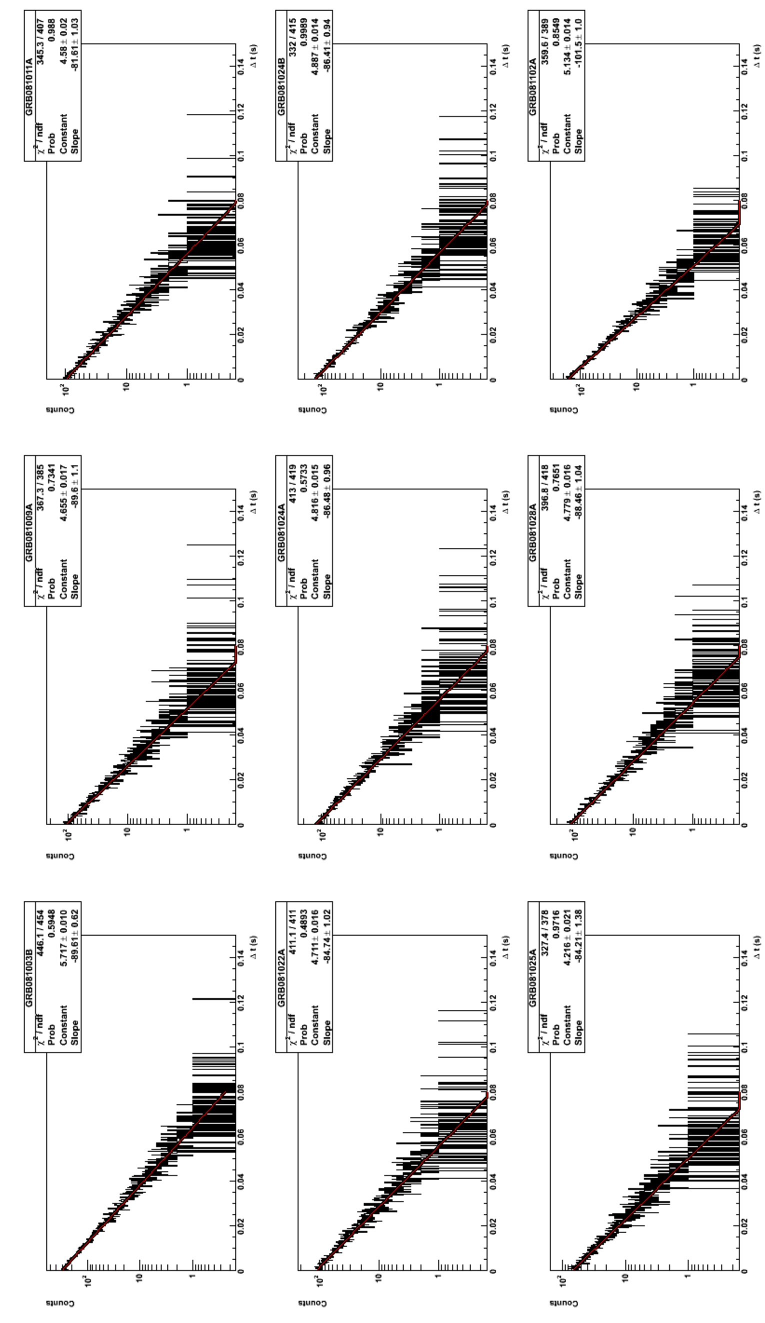

Figure B.5: The difference in time between consecutive events is plotted. The events are filtered up to level 2 (see sectionsec:Filter) and need to lie within a 40° degree opening angle around the GRB position.

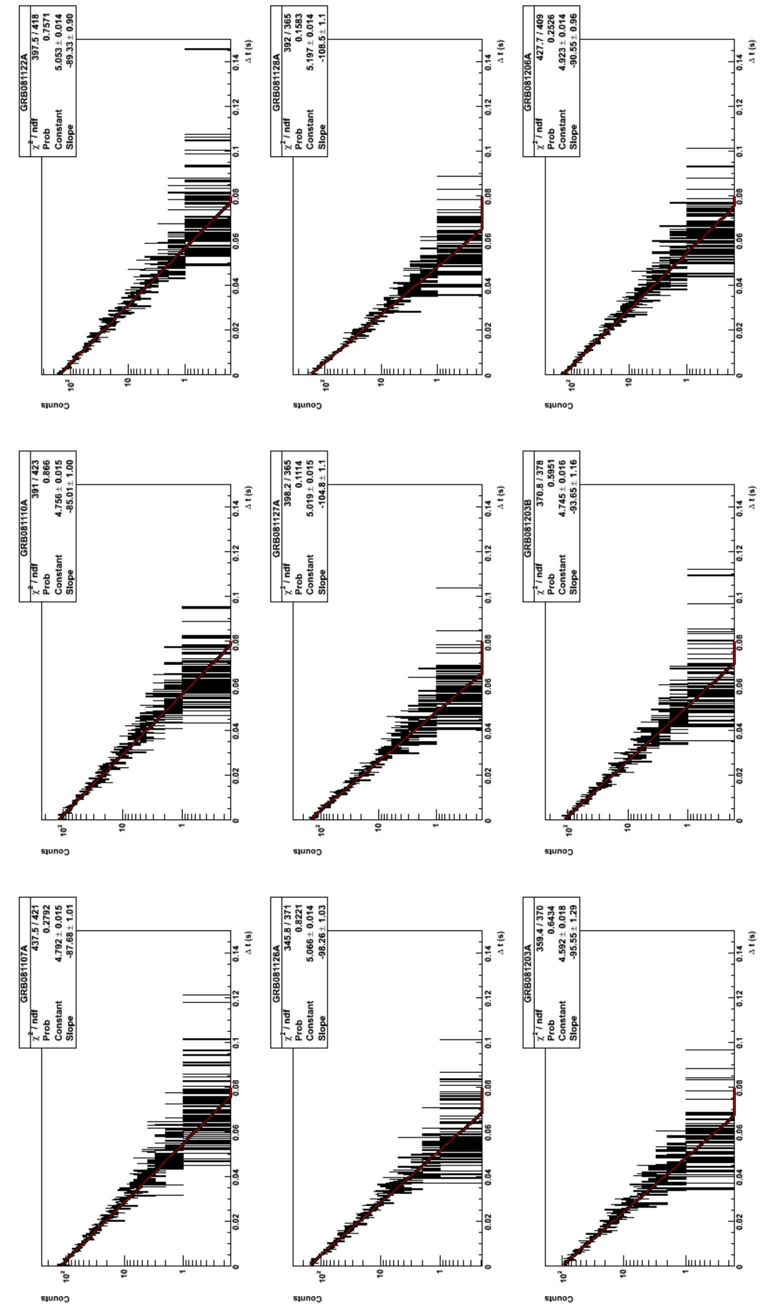

Figure B.6: The difference in time between consecutive events is plotted. The events are filtered up to level 2 (see sectionsec:Filter) and need to lie within a 40° degree opening angle around the GRB position.

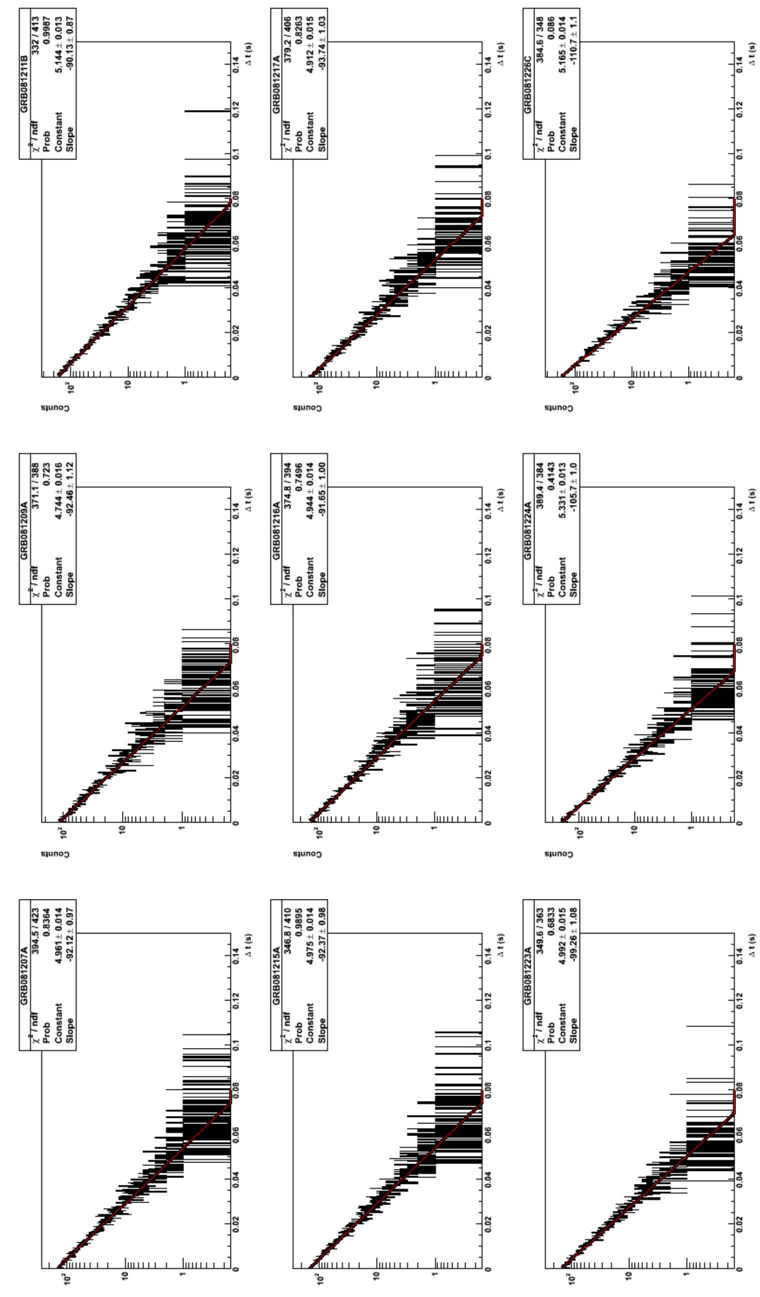

Figure B.7: The difference in time between consecutive events is plotted. The events are filtered up to level 2 (see sectionsec:Filter) and need to lie within a 40° degree opening angle around the GRB position.

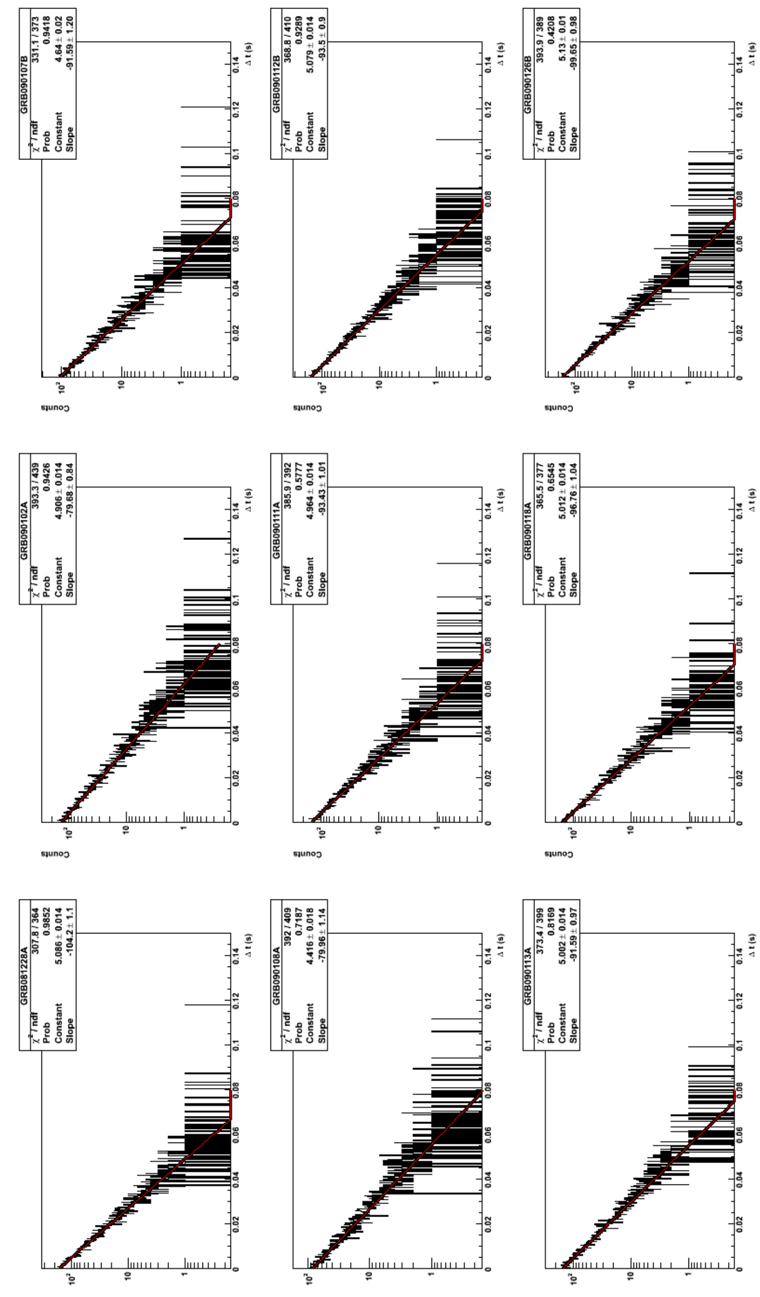

Figure B.8: The difference in time between consecutive events is plotted. The events are filtered up to level 2 (see sectionsec:Filter) and need to lie within a 40° degree opening angle around the GRB position.

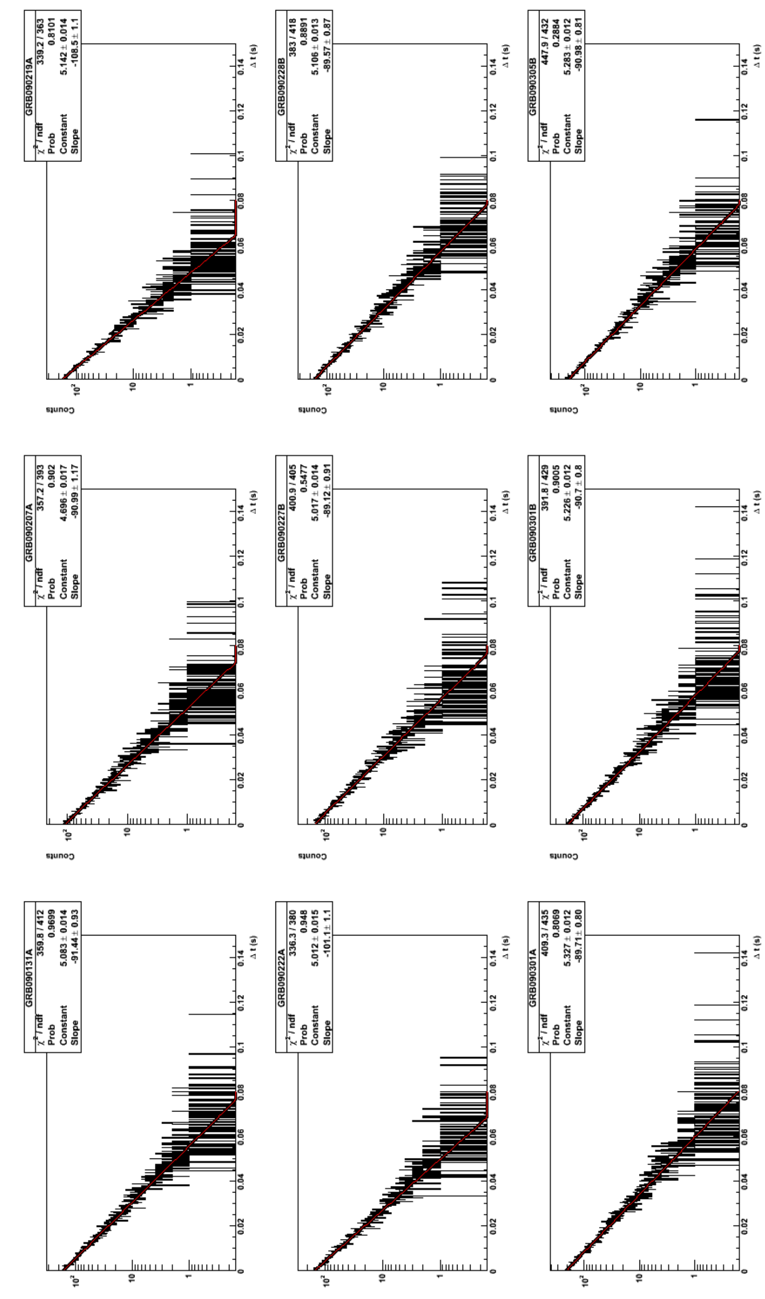

Figure B.9: The difference in time between consecutive events is plotted. The events are filtered up to level 2 (see sectionsec:Filter) and need to lie within a 40° degree opening angle around the GRB position.

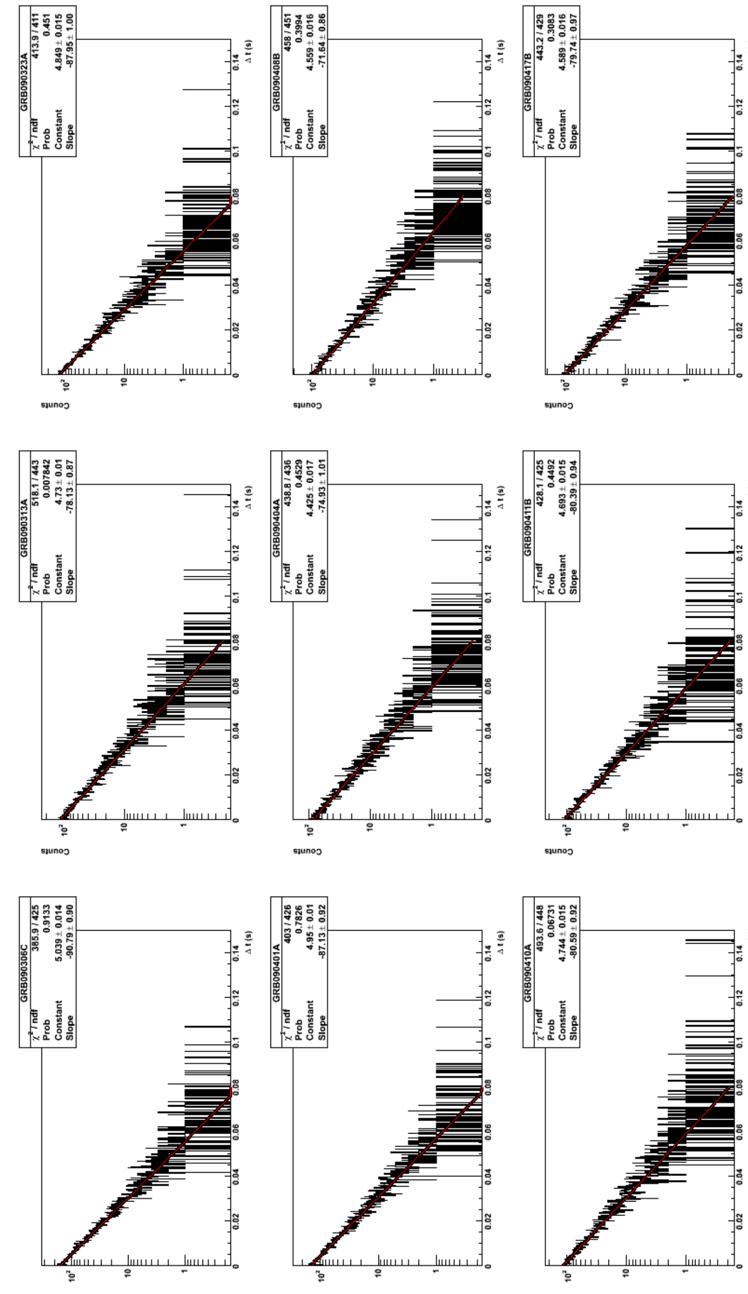

Figure B.10: The difference in time between consecutive events is plotted. The events are filtered up to level 2 (see sectionsec:Filter) and need to lie within a 40° degree opening angle around the GRB position.

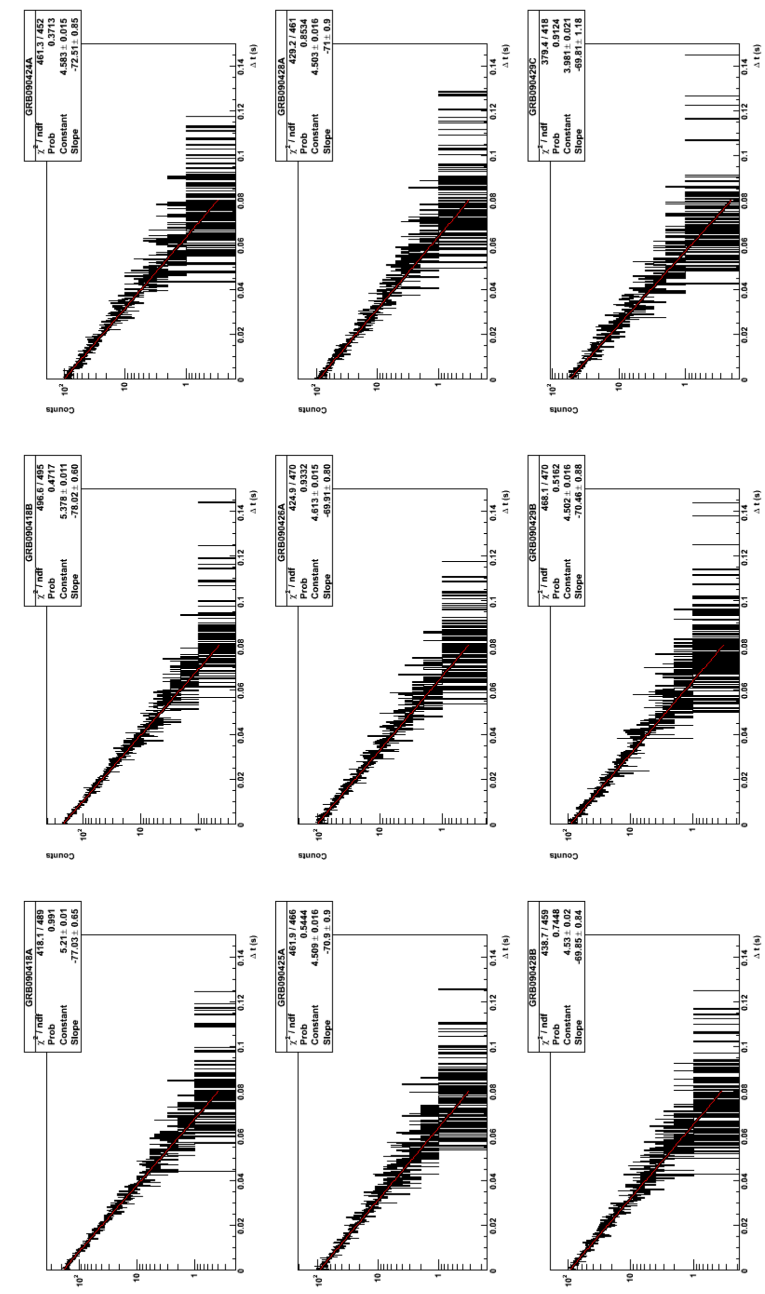

Figure B.11: The difference in time between consecutive events is plotted. The events are filtered up to level 2 (see sectionsec:Filter) and need to lie within a 40° degree opening angle around the GRB position.

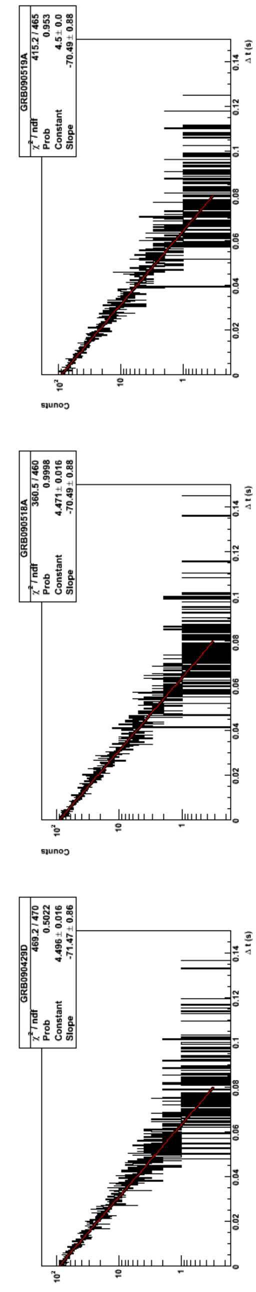

Figure B.12: The difference in time between consecutive events is plotted. The events are filtered up to level 2 (see sectionsec:Filter) and need to lie within a 40° degree opening angle around the GRB position.

Appendix C

A comparison of Ψ and Poisson statistics

An extensive comparison between the Ψ statistics and Poisson statistics (see section 5.2 and 5.2.2) has been performed by Martijn Duvoort [24]. The table below gives an illustration of the comparison where it is shown that the Poisson statistics give a more conservative $P-values$ than the exact Bayesian Ψ approach.

The $P-values$ for several observed distributions are calculated with the Ψ statistical approach as well as with the "frequentest" approach. The different distributions are characterized by the total number of events N, and the number of signal events $n_{signal} = N - n_{background}$. In these example distributions, the background events are randomly distributed over all the (static 60 sec) time-bins in the two-hour time window, such that at maximum one background event falls in one time-bin. The total number of signal events, n_{signal} cluster in the center time-bin. The Ψ_0 value is calculated for these distributions as well as the $P-value$ with the Ψ statistics following the procedure in section 5.2. The $P-value$ following the Poisson statistics of section 5.2.2 yields a $P-value$ before and after it has been corrected with the trial factor. The corrected $P-value$ of the Poisson approach should be compared to the $P-value$ of the Bayesian Ψ statistical approach. Note that correcting the higher probabilities with the trial factor yields a probability larger than unity. This is an anomaly of the correction method, but will not effect the comparison as we want to compare the low probability values.

		Ψ-statistics		Poisson statistics		
N	n_{signal}	Ψ_0	P-value	μ	P-value	P-value $\times(N_t = 120)$
1	1	20.79	1	1/120	8.30×10^{-3}	0.99
2	1	38.57	1	2/120	1.65×10^{-2}	1.98
	2	41.58	8.33×10^{-3}		1.37×10^{-4}	1.65×10^{-2}
3	1	54.59	1	3/120	2.47×10^{-2}	2.96
	2	57.60	2.49×10^{-2}		3.07×10^{-4}	3.69×10^{-2}
	3	62.38	7.01×10^{-5}		2.56×10^{-6}	3.07×10^{-4}
4	1	69.37	1	4/120	3.28×10^{-2}	3.93
	2	72.38	4.92×10^{-2}		5.43×10^{-4}	6.52×10^{-2}
	3	77.15	2.77×10^{-4}		6.02×10^{-6}	7.22×10^{-4}
	4	83.17	5.63×10^{-7}		5.01×10^{-8}	6.01×10^{-6}
5	1	83.17	1	5/120	4.08×10^{-2}	4.90
	2	86.18	6.11×10^{-2}		8.44×10^{-4}	1.01×10^{-1}
	3	90.95	4.61×10^{-4}		1.17×10^{-5}	1.40×10^{-3}
	4	96.97	1.40×10^{-6}		1.21×10^{-7}	1.46×10^{-5}
	5	103.96	9.00×10^{-9}		1.01×10^{-9}	1.21×10^{-7}
6	1	96.18	1	6/120	4.88×10^{-2}	5.85
	2	99.19	7.33×10^{-2}		1.21×10^{-3}	1.45×10^{-1}
	3	103.96	7.13×10^{-4}		2.01×10^{-5}	2.41×10^{-3}
	4	109.98	2.87×10^{-6}		2.50×10^{-7}	3.00×10^{-5}
	5	116.97	2.70×10^{-8}		2.50×10^{-9}	3.00×10^{-7}
	6	124.75	$< 1.0 \times 10^{-9}$		2.08×10^{-11}	2.49×10^{-9}

Figure C.1: Comparison between the significance of specific configurations of entries using Ψ statistics and using Poisson statistics. The correction on the probabilities for the trial factor produces unphysical results for the very high probabilities. Overall, the Poisson statistical approach results in more conservative $P - values$ than the Ψ statistical approach.

List of Abbreviations

ADC	Analog to Digital Converter, the amplitude of a pulse from a DOM
AMANDA	Antarctic Muon and Neutrino Detector Array, the predecessor of the IceCube detector
ATWD	Analog Transient Waveform Digitizer, specific waveform of a DOM
BAT	Burst Alert Telsecope
BATSE	Burst and Transient Source Experiment
BeppoSAX	Beppo Satellite per Astronomia a raggi X, an Italian-Dutch satellite for X-ray astronomy, also used for GRB research
CGRO	Compton Gamma Ray Observatory
CMB	Cosmic Microwave Background
Corsika	Simulation package used to simulate atmospheric muons and neutrinos
DAQ	Data Acquisition System
DirectWalk	A first-guess reconstruction algorithm
DOM	Digital Optical Modules, the basic detector element of the IceCube detector
DOMSimulater	Simulation package used to simulate the DOM respons of simulated photons
EAS	Extensive Air Showers, produced by cosmic rays
EGRET	Energetic Gamma Ray Experiment Telsecope
FADC	Fast Analog to Digital Converter
FE	Feature Extractor, an algorithm to determine the hits in a waveform
GBM	Gamma-Ray Burst Monitor
GRB	Gamma-Ray Burst
GROND	Gamma-Ray Burst Optical/Near-Infrared Detector
GZK	Greisen-Zatsepin-Kuzmin
HLC	Hard Local Coincidence Hit
LAT	Large Area Telescope
LE	Leading Edge, start time of a pulse
MC	Monte Carlo, indicating a simulation procedure
MDF	Model Discovery Factor
MDP	Model Discovery Potential
MMC	Muon Monte Carlo, simulation package used to propagat muons through matter

MPE	Multiple Photo-Electron
PE	Photo-electron, a unit used for the amplitude of an DOM signal
Paraboloiderror	Name of the algorithm determining the uncertainty of the log-likelihood reconstructtion
PMT	Photo Multiplier Tube, the main photon detector devise of the IceCube detector
rlogl	Reduced log-likelihood, quality parameter of a track
SLC	Soft Local Coincidence Hit
SWIFT	A multi-wavelength space-based observatory dedicated to the study of GRBs
T_{90}	Duration in which 90% of the detected photons of a Gamma-Ray Burst are detected
TE	Trailing Edge, end time of a pulse
TOT	Time Over Threshold, the duration of a pulse
TREL	Track Element, a construction used by some first-guess algorithms
UVOT	UV/Optical Telescope
Waveform	Representation of the signal a DOM detects
XTC	X-ray Telescope

Bibliography

[1] V. F. Hess, Reviews of Modern Physics **11**, 153 (1939).

[2] C. Amsler, et al. for the Particle Physics Data Group, Physics Letters **B667** (2008).

[3] L. Anchordoqui, T. Paul, S. Reucroft, and J. Swain, hep-ph/0206072 (2002), Int.J.Mod.Phys.A18:2229-2366,2003.

[4] P. Auger, P. Ehrenfest, R. Maze, J. Daudin, and R. A. Fron, Reviews of Modern Physics **11**, 288 (1939).

[5] J. Linsley, Physical Review Letters **10**, 146 (1963).

[6] K. Suga, H. Sakuyama, S. Kawaguchi, and T. Hara, Physical Review Letters **27**, 1604 (1971).

[7] S. Gabriel and G. Patrick, *Solar Energetic Particle Events: Phenomenology and Prediction*, Astronautics Research Group, 2006.

[8] E. Waxman, Physical Review Letters **75** (1995).

[9] T. P. A. Collaboration et al., Physical Review Letters **101**, 061101 (2008).

[10] H. R. F. E. Collaboration et al., Physical Review Letters **100**, 101101 (2008).

[11] K. Greisen, Physical Review Letters **16** (1966).

[12] P. Gorham, 1st International Workshop an the Saltdome Shower Array (SalSA) (2005).

[13] J. Abraham et al., Astroparticle Physics **31**, 399 (2009).

[14] E. Fermi, Physical Review **75**, 1169 (1949).

[15] R. Blandford and D. Eichler, Physics Reports **154**, 1 (1987).

[16] L. Davis, Physical Review **101**, 351 (1956).

[17] R. J. Protheroe, Astrophysical sources of high energy neutrinos, 1998.

[18] M. A. Lieberman and A. J. Lichtenberg, Physical Review A **5**, 1852 (1972).

[19] A. R. Bell, MNRAS **182**, 147 (1978).

[20] R. D. Blandford and J. P. Ostriker, J.P. **221**, L29 (1978).

[21] G. F. Krymskii, Akademiia Nauk SSSR Doklady **234**, 1306 (1977).

[22] W. I. Axford, E. Leer, and J. F. McKenzie, AAP **111**, 317 (1982).

[23] L. Anchordoqui, T. Paul, S. Reucroft, and J. Swain, (2002).

[24] M. Duvoort, *A search for Gamma Ray Burst Neutrinos in AMANDA*, University of Utrecht, PhD thesis, 2009.

[25] J. Ahrens et al., Astroparticle Physics **20**, 507 (2004).

[26] R. Klebesadel, I. Strong, and R. Olson, (1973).

[27] W. S. Paciesas et al., astro-ph/9903205 (1999), Astrophys.J.Suppl. 122 (1999) 465-495.

[28] L. Piro et al., IAU **6467**, 1 (1996).

[29] T. Piran, A. Shemi, and R. Narayan, Monthly Notices of the Royal Astronomical Society **263**, 861 (1993).

[30] P. Meszaros and M. J. Rees, The Astrophysical Journal **405**, 278 (1993).

[31] A.Achterberg, University of Utrecht: Lecture Notes .

[32] W. Zhang, S. E. Woosley, and A. I. MacFadyen, Astrophysical Journal **586** (2003).

[33] S. E. Woosley, The Astrophysical Journal **405**, 273 (1993).

[34] J. S. Bloom, D. A. Frail, and S. R. Kulkarni, The Astrophysical Journal **594**, 674 (2003).

[35] J. B. Hartle and T. Dray, American Journal of Physics **71**, 1086 (2003).

[36] S.E.Woosley and J.S.Bloom, Annual Rev.Astron. Astorphys. **44** (2006).

[37] S. Kobayashi, T. Piran, and R. Sari, The Astrophysical Journal **490**, 92 (1997).

[38] Daigne and Mochkovitch, Monthly Notices of the Royal Astronomical Society **296**, 275 (1998).

[39] J. G. Learned and S. Pakvasa, Astroparticle Physics **3**, 267 (1995).

[40] E. Waxman and J. N. Bahcall, The Astrophysical Journal **541**, 707 (2000).

[41] E. Waxman and J. Bahcall, astro-ph/9701231 (1997), Phys.Rev.Lett. 78 (1997) 2292-2295.

[42] D. Band et al., The Astrophysical Journal **413**, 281 (1993).

[43] E. Waxman and J. Bahcall, Physical Review D **59**, 023002 (1998).

[44] S. Razzaque, P. Mészáros, and E. Waxman, Phys. Rev. D **68**, 083001 (2003).

[45] P. Lipari and T. Stanev, Physical Review D **44**, 3543 (1991).

[46] J. Arhens and et al, *IceCube Preliminary Design Document*, IceCube Collarboration IceCube Internal Wiki, 2001.

[47] R. Blair et al., Phys. Rev. Lett. **51**, 343 (1983).

[48] G. V. Domogatsky, Nuclear Physics B - Proceedings Supplements **70**, 439 (1999).

[49] M. Ageron et al., Astroparticle Physics **31**, 277 (2009).

[50] F. Halzen, The European Physical Journal C - Particles and Fields **46**, 669 (2006).

[51] R. Abbasi and et al for the IceCube Collarboration, NIM in Physics Research A (2009).

[52] IceCube-Collaboration, IceTray software package (2010).

[53] http://aliceinfo.cern.ch/Collaboration/General/ALICE ACDB.html.

[54] D. Chirkin et al., IceCube SVN Source Code Repository (2010).

[55] M. Wallraff, Internal IceCube reports **icecube/201003002** (2010).

[56] N. van Eijndhoven, IcePack software package .

[57] G. D'Agostini, Nuclear Instruments and Methods in Physics Research Section A: Accelerators, Spectrometers, Detectors and Associated Equipment **362**, 487 (1995).

[58] N. van Eijndhoven and G. de Vries, Feature Extractor, IcePack software package .

[59] T.Spectrum, ROOT package, http://root.cern.ch/root/html/TSpectrum.html .

[60] R. Brun et al., ROOT package (CERN), http://root.cern.ch/drupal/ .

[61] Z. Silagadze, NIM in Physics Research Section A **376**, 451 (1996).

[62] R. Gold, Argonne National Laboratories **Argonne Ill** (1964).

[63] C. Wendt, *DOM SPE Waveform Shape*, IceCube Internal Wiki, 2009.

[64] T. A. Collaboration and J. Ahrens, astro-ph/0407044 (2004), Nucl.Instrum.Meth.A524:169-194,2004.

[65] J. Bazo, *Towards a better muon track reconstruction in IceCube*, presentation for IceTray seminar, DESY-Zeuthen, 2008.

[66] N. van Eijndhoven, IcePack Dwalk module .

[67] N. van Eijndhoven, O. Fadiran, and G. Japaridze, Astroparticle Physics **28**, 456 (2007).

[68] N. van Eijndhoven, *Performance of the extended Direct Walk reconstruction*, presentation at the pre-meeting IceCube collaboration, 2009.

[69] V. J. Stenger, External Report HDC-1-90 **University of Hawaii at Manoa, USA** (1990).

[70] D.E.Groom, et al. (Particle Data Group), The European Physical Journal C (EPJ C) .

[71] D. Pandel, *Pandel reconstruction*, Humboldt-Universitt zu Berlin, Diploma Thesis, 1996.

[72] T. Neunhaffer, Astropart.Phys. (2004), 0403367.

[73] J. Dumm, et al. for the IceCube Collaboration, The internal IceCube Wikipages (2008).

[74] D. Heck and J. Knapp, Forschungszentrum Karlsruhem, Institut für Kernphysik (2000).

[75] http://internal.icecube.wisc.edu/simulation/dataset/2326, Nugen E^{-2} signal neutrino dataset .

[76] J. McCartin, *Cascade Reconstruction Analysis with the IceCube Neutrino Detector*, University of Canterbury, 2009.

[77] D. Chirkin and W. Rhode, hep-ph/0407075 (2004).

[78] J. Lundberg et al., NIMPR A **581**, 619 (2007).

[79] K. Nakamura, et al. (Particle Data Group), J. Phys **G 37** (2010), 075021.

[80] A. Karle, *Proc. Workshop on Simulation and Analysis Methods for Large Neutrino Telescopes*, DESY-PROC, 1999.

[81] http://internal.icecube.wisc.edu/simulation/dataset/2712, Corsika single muon dataset .

[82] http://internal.icecube.wisc.edu/simulation/dataset/2483, Corsika double muon dataset .

[83] J. Dum, IceCube Wiki page, explaination on the energy corrected sigma (2009).

[84] M. Baker, *Looking into scaling angular resolution parameters for muons for IC22/IC40*, presentation at the pre-meeting IceCube collaboration, 2009.

[85] G.Hill, J.Hodges, B.Hughey, A.Karle, and M.Stamatikos, (2006).

[86] E. Strahler, *Searches for Neutrinos from Gamma Ray Bursts with the AMANDA-II and IceCube Detectors*, PhD thesis, 2009.

[87] K. Meagher, IC40 GRB analysis (2010).

[88] N. Whitehorn, IC40 Model-Independent GRB Analysis, University of Wisconsin-Madison (2009).

[89] N. van Eijndhoven, Astroparticle Physics **28**, 540 (2008).

[90] T. Piran, astro-ph/9810256 (1998), Phys.Rept. 314 (1999) 575-667.

[91] N. R. Tanvir et al., Nature **461**, 1254 (2009).

[92] E. T. Jaynes, *Probability Theory: The Logic of Science*, Cambridge University Press, 2003.

[93] http://wiki.icecube.wisc.edu/index.php/Goodrunlist, Good Run List IceCube .

[94] B. Keilhauer, J. Blumer, R. Engel, H. Klages, and M. Risse, Astroparticle Physics **22** (2004), 249-261.

[95] F. Halzen and D. W. Hooper, ApJ **527** (2000), L93.

[96] C. Dermer and A. Atoyan, Phys. Rev. Lett. **91** (2003), 071102.